Joining of Metal and Fiber Reinforced Polymers Using Ultrasonic Additive Manufacturing

Dissertation

Presented in Partial Fulfillment of the Requirements for the Degree
Doctor of Philosophy in the Graduate School of The Ohio State
University

By

Hongqi Guo,

Graduate Program in Mechanical Engineering

The Ohio State University

2021

Dissertation Committee:

Professor Marcelo J. Dapino, Advisor

Professor Anthony Frank Luscher

Professor Noriko Katsube

© Copyright by

Hongqi Guo

2021

Abstract

Various methods have been reported to join carbon fiber reinforced polymer (CFRP) composites with aluminum alloy (AA), with strengths ranging from 13 MPa to 112 MPa. This research project presents a new method for joining carbon fiber reinforced composites and metals using ultrasonic additive manufacturing (UAM), a solid-state manufacturing technology. Dry fibers are embedded in a metal matrix to create mechanical interlocking between the fiber and metal. After the UAM process, the dry fiber-metal joint can be interleaved with additional fiber fabrics to create FRP components with metal tabs that enable the FRP to be joined with metal structures using conventional metal-metal joining techniques.

A manufacturing approach for producing continuous CFRP and aluminum alloy (AA) joints is developed. Mechanical testing demonstrates that the joints achieve a 129.5 MPa tensile strength. The failure mode can be designed to be fiber failure or metal failure based on the fiber-to-metal bearing area ratio. Failure in metal leads to high peak load, and failure in fiber is associated with high energy absorption due to fiber pull-out after initial fracture.

The utilization of resistance spot welding (RSW) to join the UAM CFRP-AA joints to bulk AA is investigated by mechanical testing and hardness mapping. In addition to the coupon-level mechanical tests, structure-level tests are performed to evaluate the benefits of UAM CFRP-AA joints. CFRP-AA hybrid beam structures are manufactured using RSW through CFRP-AA joints with the settings developed previously. Benchmarked against pop rivets, experimental results show that the beam structures with UAM joints introduce benefits in energy absorption and force efficiency in four-point bend, axial crush, and torsion.

An analytical model is developed based on the thick-wall cylindrical pressure vessel theory. The model is able to predict the tensile peak load and failure mode of the joints based on the material properties and joint design. An FEA model is created based on parameters calculated from the analytical model. The FEA model accurately predicts the tensile behavior of the CFRP-AA joints.

A countermeasure to galvanic corrosion is developed by applying a Kevlar fiber reinforced polymer (KFRP) buffer to insulate the CFRP-AA couple. A 12-year equivalent corrosion cyclic test (CCT) is performed. The result demonstrates that the CFRP-KFRP-AA joint can maintain 95% tensile strength and achieve zero mass loss.

The technique of UAM FRP-metal joining has been applied to 1010 steel. A UAM manufacturing process is developed to create 1010 bonding with high shear strength at room temperature. Tensile tests are performed on KFRP-1010 steel joints and KFRP tow failure mode is achieved with high strength. RSW and corrosion studies are also carried out on the steel-based joints.

Acknowledgments

Firstly, I would like to thank my advisor, Prof. Marcelo Dapino, for providing me with the opportunity to work on this exciting research project. His continuously insightful guidance with immense knowledge and professionalism is extremely appreciated. I would also like to thank my committee members, Prof. Anthony Luscher and Prof. Noriko Katsube, for their support and advice on this study. I'm very grateful for Dr. Ryan Hahnlen's consistent technical guidance in this project.

Thanks to my colleagues in the SMSL lab. Working with them has been a pleasure. Thanks to Dr. Leon Headings for his help and advice. Thanks to Bryant Gingerich for mentoring me and maintaining the UAM lab. Special thanks to the MAE and MSE departments staff that have provided substantial technical support that enables the experimental studies in this project.

Thanks to Dr. Shichao Cui for being the most supportive friend these years. Thanks to my cat Bon-Bon for being the warmest companion.

Finally, I would like to thank my grandmother and parents for their love, support, and encouragement.

Vita

July, 2016	B.S. Composite Materials and Engineering, Harbin Institute of Technology, Harbin, Heilongjiang, China
2016-2021	Graduate Research Associate, The Ohio State University, Columbus, Ohio, United States

Publications

Guo, H., Gingerich, M. B., Headings, L. M., Hahnlen, R., & Dapino, M. J. (2019). Joining of carbon fiber and aluminum using ultrasonic additive manufacturing (UAM). *Composite Structures, 208, 180-188.*

Guo, H., Gingerich, M. B., Headings, L. M., Hahnlen, R., & Dapino, M. J. (2021). Experimental investigation of CFRP-AA structures joined by ultrasonic additive manufacturing (UAM) and resistance spot welding (RSW). *Composites Part B: Engineering, in preparation*

Fields of Study

Major Field: Mechanical Engineering

Studies in:

Ultrasonic Additive Manufacturing

Metal/FRP Joining

Table of Contents

Page

Abstract ii

Acknowledgments iv

Vita v

List of Tables x

List of Figures xiii

1. Introduction 1

   1.1 Literature Survey 1
      1.1.1 Background 1
      1.1.2 Conventional CFRP-to-metal joining methods 2
      1.1.3 Innovative CFRP-to-metal joining methods 4
      1.1.4 Ultrasonic additive manufacturing (UAM) 6
   1.2 Objectives 8
   1.3 List of acronyms 10

2. CFRP-AA Joint Using UAM 11

   2.1 Material and methods 12
      2.1.1 Materials and components 12
      2.1.2 Sample preparation 13
   2.2 Optical imaging 19
   2.3 Tensile test 21
      2.3.1 CF tow failure 23
      2.3.2 AA matrix failure 26
   2.4 Cross-tensile test 29
   2.5 Summary 33

3. Effect of RSW on CFRP-AA UAM Joints 35

3.1 Investigation of the effect of RSW on UAM aluminum 35
  3.1.1 Tensile testing 36
  3.1.2 Cross-tension testing 40
3.2 Investigate the heat affected zone from RSW 43
  3.2.1 Literature review 43
  3.2.2 Hardness testing 45
3.3 Experimentally investigate the safe location of RSW on CFRP-AA joints 47
  3.3.1 Tensile tests 49
  3.3.2 Optical images 52
3.4 Summary 53

4. CFRP-AA Beams Joined by UAM and RSW 55

4.1 Literature survey 55
4.2 Sample preparation 56
  4.2.1 CFRP-AA hybrid structures 56
  4.2.2 Riveted structures 63
  4.2.3 Notation of sample configuration and load cases 64
4.3 Four-point-bend tests 65
  4.3.1 Experimental method 65
  4.3.2 Results and discussion 66
  4.3.3 Conclusion 73
4.4 Axial crush tests 73
  4.4.1 Experimental method 73
  4.4.2 Results and discussion 77
  4.4.3 Conclusion 82
4.5 Torsion tests 82
  4.5.1 Experimental method 82
  4.5.2 Results and discussion 83
  4.5.3 Conclusion 90
4.6 Summary 90

5. Analytical and Finite Element Models of FRP-metal UAM Joints 93

5.1 Analytical model 93
  5.1.1 Stress in embedded FRP loops 97
  5.1.2 FRP-metal joint tensile strength 101

5.1.3 Comparing CFRP-AA joint strength from experiments and the analytical model 107
5.2 Finite element model 109
5.3 Summary 116

6. Corrosion Mitigation of CFRP-AA UAM Joints 118

6.1 Investigate the effect of galvanic corrosion on CFRP-AA joints . . . 118
6.1.1 Construct corrosion samples 118
6.1.2 Perform corrosion cycling 120
6.1.3 Perform post corrosion testing and sample evaluation 121
6.2 Mechanical performance of CFRP-KFRP-AA Joint 124
6.3 Galvanic corrosion mitigation of CFRP-KFRP-AA joints 134
6.3.1 Construct corrosion samples 134
6.3.2 Resistance measurements 138
6.3.3 Perform post corrosion testing and sample evaluation 140
6.4 Summary 154

7. CFRP-1010 Steel Joints by UAM 156

7.1 UAM process for 1010 steel 156
7.1.1 UAM parameter for annealed 1010 steel 156
7.1.2 Shear tests of 1010 steel UAM welds 160
7.2 Kevlar-1010 steel joint 167
7.2.1 Sample preparation 167
7.2.2 Tensile test of KFRP-1010 steel UAM joint 167
7.3 Effect of RSW on Kevlar-1010 steel joints 169
7.3.1 Lap shear test of RSW between UAM 1010 and JAC 270 . . 170
7.3.2 Heat affected zone of RSW between UAM 1010 and JAC 270 173
7.4 Corrosion mitigation investigation of Kevlar-1010 steel joints 174
7.5 Summary 177

8. Conclusions and Future Work 179

8.1 Summary 179
8.2 Contributions 182
8.3 Future work 184

Appendices 186

A. Corrosion study data 186

B. CFRP mechanical tests 190

B.1 Longitudinal tensile test 190
B.2 Longitudinal compressive test 192

C. Additional tensile test of CFRP-AA joints 195

Bibliography 200

List of Tables

Table **Page**

1.1 List of acronyms 10

2.1 Experimentally measured ultimate tensile strengths of CFRP-AA joint materials. 13

2.2 Welding parameters for AA 6061-H18. 19

2.3 Peak loads of cross-tension tests 32

3.1 UAM weld parameters 36

3.2 RSW parameters for UAM 6061-H18 and bulk 6061-T6 36

3.3 Tensile test results of RSW samples of UAM AA 6061-H18 and bulk AA 6061-T6 39

3.4 Cross-tensile test results of RSW samples 42

4.1 Welding parameters for AA 6061-H18 foils 59

4.2 RSW parameters 61

4.3 Summary of sample configurations. CFRP: CFRP hat, AA: AA plate. 64

4.4 Four point bend results for top-hat structures. 67

4.5 Dynamic axial crush performance of riveted and UAM samples. . . . 80

4.6 Torsion test results for UAM and rivet samples 86

5.1 Analytical model parameters of CFRP-AA joints 97

5.2 Analytical and experimental results of tensile tests on CFRP-AA joints 108

5.3 CONSTRAINED_GENERALIZED_WELD parameters 112

5.4 Model and experimental results of tensile tests on CFRP-AA joints . 116

6.1 Grouping for corrosion samples 120

6.2 Corrosion cycle process 121

6.3 Channel geometries of the final KFRP-AA joint design (unit:mm) . . 124

6.4 Stacking sequence of the final KFRP-AA joint design. 125

6.5 Welding parameters of the final KFRP-AA joint design. 125

6.6 Peak loads and energy absorptions of tensile samples 128

6.7 Peak loads of cross-tensile samples 132

6.8 Resistances of CF-outside and CF-inside samples (unit:Ω) 139

6.9 Average masses and mass losses of samples before and after the CCT process (unit:g) 149

6.10 Average and standard deviation of peak loads of samples after CCT process (unit:N) 151

7.1 UAM parameters for welding 1010 steel at room temperature. 159

7.2 Transverse shear strengths of 1010 steel samples 163

7.3 Interface shear strengths of 1010 steel samples 166

7.4 RSW parameters for UAM 1010 and bulk JAC 270 170

7.5 Lap shear peak load of RSW between UAM 1010 and JAC 270 172

A.1 Tensile peak loads of samples after CCT process (unit:N) 187

A.2 Masses of samples before and after CCT process (unit:g). Samples 1 to 3. 188

A.3 Masses of samples before and after CCT process (unit:g). Samples 4 to 6. 189

B.1 CFRP longitudinal ultimate tensile strength 192

B.2 CFRP longitudinal ultimate compressive strength 194

List of Figures

Figure **Page**

1.1 Utility of each adhesive and surface treatment; P is polyurethane and E is epoxy [1]. 3

1.2 Schematic of a AA/CFRP clinched joint cross section [24]. 4

1.3 Schematic diagram of an ultrasonic torsion welding system [45]. . . . 6

1.4 Ultrasonic additive manufacturing process (schematic not to scale). The normal force and lateral vibrations collapse asperities and disperse oxides to produce intimate metal-to-metal contact, resulting in solid-state welding. 7

2.1 Example hybrid CFRP-metal hat structure with UAM transition joints and RSW welds to connect the AA transition to a flat metal sheet (at the bottom of the hat). 12

2.2 CFRP-AA joint manufacturing process schematics 14

2.3 CFRP-AA transition joint manufacturing progression 16

2.4 Schematic of looped channels to house the dry CF tows. 17

2.5 (a) Schematic cross section of 3-CF-layer transition joints; and (b) schematic cross section of 4-CF-layer transition joints. The CFRP component shown represents the CF after layup and cure in epoxy. (Schematics not drawn to scale.) 18

2.6 CFRP-AA interface at the channel side walls. 20

2.7 CFRP-AA interface at the lower and upper edges. 21

2.8 CFRP-AA tensile samples: (a) picture and (b) schematic. 22

2.9 Load vs. displacement curves for tensile tests on 3-CF-layer and 4-CF-layer samples. The straight lines are caused by undersampling of the DIC system's cameras. 23

2.10 DIC strain maps at different displacements for 3-CF-layer sample 2: (a) 0.036 mm; (b) 0.057 mm; (c) 0.086 mm; and (d) 1.44 mm of displacement. Failure takes place in the CF tows. 24

2.11 3-CF-layer sample after tensile testing (speckled for DIC measurements). 25

2.12 Loading diagram of one layer of CF loops in a 25.4 mm wide sample. 26

2.13 4-CF-layer sample after testing (speckled for DIC measurements). . . 27

2.14 DIC strain maps at different displacements for a 4-CF-layer sample failing in the AA matrix: (a) 0.011 mm; (b) 0.045 mm; (c) 0.076 mm; and (d) 2.13 mm. 28

2.15 Schematic of the projection of an AA failure interface. 29

2.16 Shape and dimensions of CTS test pieces from JIS 3137. 30

2.17 (a) Fixture for cross-tension tests; (b) cross tensile testing setup consisting of an MTS load frame and the fixture. 30

2.18 CTS samples before testing. 31

2.19 Load vs. displacement plot for the CTS samples. 32

2.20 CTS samples after testing. 33

3.1 Tensile samples before testing: (a) UAM-bulk samples; (b) bulk-bulk samples 37

3.2 Tensile samples after testing with close-up images of representative failed joints: (a) UAM-bulk samples; (b) bulk-bulk samples 38

3.3 Load vs crosshead displacement plot of tensile tests on 2nd round RSW samples. 39

3.4 Cross-tensile samples before testing: (a) UAM-bulk samples; (b) bulk-bulk samples 40

3.5 Cross-tensile samples after testing with close-up images of representative failed joints: (a) UAM-bulk samples; (b) bulk-bulk samples . . . 41

3.6 Load vs crosshead displacement plot of cross-tensile tests on RSW samples. 42

3.7 Schematic cross-section of a resistance spot weld [20]. 43

3.8 (a) Temperature ratio vs. non-dimensional radius; (b) weld nugget geometry and isothermal distribution [35]. 44

3.9 Cross-section micrograph of resistance spot welded dual-phase steel with two sets of microhardness indentations [20]. 44

3.10 Optical image of the cross-section of a UAM-bulk RSW sample with indents for hardness testing. 45

3.11 Hardness distribution along two lines close to the interface. 46

3.12 Hardness map of a UAM AA/bulk AA RSW. 47

3.13 UAM transition coupons for RSW. 48

3.14 UAM transition coupons welded to bulk AA tab by RSW and prepared for tensile tests: (a) schematic of the samples; (b) front; (c) back. . . 49

3.15 UAM transition coupons welded to bulk AA tabs by RSW after tensile tests. 50

3.16 Scatter diagram of peak tensile load vs RSW location. 51

3.17 DIC strain map indicates nonuniform loading of samples with RSW at 5R: (a) sample from flange A; (b) samples from flange C. 52

3.18 Images of CFRP-AA coupons after RSW at different locations. Red lines and arrows in the schematic to the left of the image indicates the corresponding imaging location. 53

4.1 Procedures to construct CF-AA transition joints. 58

4.2 Side view of a 3-CF-layer transition joint (schematic not drawn to scale). 59

4.3 Mold for CFRP laying up of the hybrid hat structure. 60

4.4 Layup configuration for a CFRP hat with AA flanges. Black layers are dry CF fabrics joined with the AA flanges. Red and blue layers are additional CF pre-preg fabrics. Layup is not shown to scale. 60

4.5 Dimensions of a hybrid hat structure. 61

4.6 Using RSWs to join a UAM hat with an AA plate to construct a top-hat section. 62

4.7 Using RSWs to join two UAM hats to construct a double-hat section. 62

4.8 (a) A UAM top-hat structure; (b) a UAM double-hat structure. . . . 63

4.9 (a) A riveted top-hat structure; (b) a riveted double-hat structure. . . 64

4.10 Load vs. displacement curves for four-point bend tests on (a) UAM samples and (b) riveted samples. 66

4.11 Strain maps of sample Rivet-b-1 during testing: (a) strain distribution at the beginning of the test; (b) cracks initiate under two upper loading noses; (c) cracks propagate, a rivet fails, and the AA plate separates from the CFRP; (d) test ends when the left side of the sample slips off the left support. 69

4.12 Riveted top-hat structures after four-point-bend tests: samples (a) Rivet-b-1; (b) Rivet-b-2; (c) Rivet-b-3; (d) Rivet-b-4. 70

4.13 Strain maps of sample UAM-b-1 during testing: (a) strain distribution before any cracks initiate; (b) cracks initiate under two upper loading noses; (c) cracks propagate and the flange deforms with the AA plate; (d) test ends when CFRP hat fails. 71

4.14 UAM top-hat structures after four-point-bend tests: samples (a) UAM-b-1; (b) UAM-b-2; (c) UAM-b-3. 72

4.15 Detailed pictures of joint failures for hat-plate structures: (a) rivet failure; (b) UAM flange cracking; (c) UAM flange delamination. . . . 72

4.16 Drop tower for axial crush testing. 74

4.17 Schematics of fixtures for axial crush testing. 74

4.18 Axial crush testing setup: (a) cameras set up for data collection; (b) riveted sample in the fixture before testing; (c) riveted sample in the fixture after crushing. 76

4.19 Sample Rivet-c-3 during axial crush testing. Units: time - ms; displacement - mm. 77

4.20 Load vs. displacement plots of axial crush samples: (a) riveted samples; (b) UAM samples. 78

4.21 Energy absorption vs. displacement plot of axial crush samples. . . . 79

4.22 CFRP double-hat structures after axial crush testing: (a) to (d) riveted samples; (e) to (g) UAM samples. 81

4.23 Failed flanges after axial crush testing: (a) riveted samples; (b) UAM samples. 82

4.24 Setup for torsion tests. 83

4.25 Torque vs. twist angle curves for rivet samples: (a) 0 to 1.75 rad (100 degrees); (b) 0 to 0.5 rad (29 degrees). 84

4.26 Torque vs. twist angle curves for UAM samples: (a) 0 to 1.75 rad (100 degrees); (b) 0 to 0.5 rad (29 degrees). 85

4.27 Pictures of the UAM samples after torsion tests: (a) UAM-t-1; (b) UAM-t-2; (c) UAM-t-3; (d) UAM-t-4. 87

4.28 Failure modes in UAM samples: (a) CFRP hat breaking; (b) CFRP tow shearing; (c) AA matrix breaking; (d) AA flange breaking (RSW plug fracture). 88

4.29 Pictures of each side of the rivet samples after torsion tests: (a) Rivet-t-1; (b) Rivet-t-2; (c) Rivet-t-3; (d) Rivet-t-4. 89

4.30 Rivet shearing in rivet samples: (a) all the rivets sheared off along one side of the flange; (b) a sheared rivet. 90

5.1 Schematic of the FRP loop for analytical modeling. Loop spacing is defined as the center-to-center distance between the two corners of the FRP tow in the loop. 96

5.2 Stress distribution in the embedded FRP tow. 100

5.3 FEA result of a FRP strap wrapping around a rod[17]: (a) FEA mesh; (b) circumferential stress distribution; (c) inter-laminate shear stress distribution[17]. 100

5.4 Peak load per tow. 102

5.5 Projection of the cross-section along the fracture line. 104

5.6 Peak load vs sample thickness. 105

5.7 Peak load vs loop spacing. 106

5.8 Peak load vs loop spacing with experimental results. 109

5.9 Shell mesh of a tensile joint with a 2.5 mm mesh size. 111

5.10 Tensile failure modes of CFRP-AA joints in FEA simulation. 113

5.11 Stress distribution of CFRP-AA joints in FEA simulation. 113

5.12 Load vs displacement curves of FEA and experiment results. 115

6.1 25.4 mm wide samples for corrosion tests. 119

6.2 Corrosion samples pulled out after 25 cycles. 122

6.3 Corrosion samples pulled out after 40 cycles. 123

6.4 E-coated CFRP-AA samples after 120 cycle. 123

6.5 Pictures of tensile samples before testing. (a) front, (b) back. 126

6.6 Load vs. displacement curves of joint samples during tensile tests. . . 127

6.7 DIC strain maps of tensile sample 1 during testing. 129

6.8 Pictures of TSS samples after testing. 129

6.9 Pictures of cross-tensile samples before testing. 130

6.10 Picture of a cross-tensile sample mounted in the fixture that is gripped by two MTS wedge grips in the load frame. 131

6.11 Load vs. displacement curves for cross-tensile samples. 132

6.12 Pictures of cross-tensile samples after testing. 133

6.13 Picture and schematic of a buffer sample. (Schematic not drawn to scale) 135

6.14 Pictures and schematics of a CF-outside sample and a CF-inside sample. (Schematics not drawn to scale) 135

6.15 Picture of all CCT samples. 137

6.16 Grouping of CCT samples. I-XII are groups for buffer samples. CI and CO indicates CF-inside and CF-outside samples, respectively. (a) 60 buffer samples from flanges A-E are assigned to 12 colors, 6 CF-inside and 6 CF-outside samples are made from flange F; (b) 12 colors for buffer samples are randomly assigned to 12 groups; (c) group numbers with the corresponding color, number of corrosion cycles and sample labels. 138

6.17 Circuit diagram of a buffer sample. 140

6.18 Group 1: uncoated buffer samples after 0 cycles. Sample sequence: A11, B1, C3, D5, E7. 141

6.19 Group 2: uncoated buffer samples after 25 cycles. Sample sequence: A4, B6, C8, D10, E12. 141

6.20 Group 3: uncoated buffer samples after 50 cycles. Sample sequence: A9, B11, C1, D3, E5. 142

6.21 Group 4: uncoated buffer samples after 60 cycles. Sample sequence: A8, B10, C12, D2, E4. 142

6.22 Group 5: uncoated buffer samples after 70 cycles. Sample sequence: A2, B4, C6, D8, E10. 143

6.23 Group 6: uncoated buffer samples after 80 cycles. Sample sequence: A1, B3, C5, D7, E9. 143

6.24 Group 7: uncoated buffer samples after 90 cycles. Sample sequence: A6, B8, C10, D12, E2. 144

6.25 Group 8: uncoated buffer samples after 100 cycles. Sample sequence: A12, B2, C4, D6, E8. 144

6.26 Group 9: uncoated buffer samples after 110 cycles. Sample sequence: A5, B7, C9, D11, E1. 145

6.27 Group 10: uncoated buffer samples after 120 cycles. Sample sequence: A7, B9, C11, D1, E3. 145

6.28 Group 11: e-coated buffer samples after 0 cycles. Sample sequence: A3, B5, C7, D9, E11. 146

6.29 Group 12: e-coated buffer samples after 120 cycles. Sample sequence: A10, B12, C2, D4, E6. 146

6.30 Group 13: uncoated CF-outside samples after 120 cycles. 147

6.31 Group 14: uncoated CF-inside samples after 120 cycles. 148

6.32 Masses of CCT samples before and after corrosion cycles. 150

6.33 Tensile peak loads vs. number of corrosion cycles. 152

6.34 CCT samples after tensile tests. 154

7.1 Stress vs strain curves of as-received and annealed 1010 steel foil tapes. 157

7.2 Head-on view of the horn in contact with the baseplate, creating a 20.3 mm wide weld. 158

7.3 A 2 mm thick 16-layer 1010 steel build. 159

7.4 Cross-section image of the UAM 1010 build. 160

7.5 (a) Schematic of a transverse shear sample in the fixture; (b) schematic of a interface shear sample in the fixture. 161

7.6 Shear fixture between two compression platens in the load frame. . . 161

7.7 Stress vs. strain curves of transverse 1010 steel shear tests. 162

7.8 Location of interface shear samples on the 1010 steel build. 163

7.9 Stress vs. strain curves of interface 1010 steel shear tests. 165

7.10 Ultimate interface shear strength. 166

7.11 Side-view schematic of the KFRP-1010 tensile sample. 167

7.12 (a) KFRP-1010 samples before tensile testing; (b) KFRP-1010 samples after tensile testing. 168

7.13 Load vs displacement curves of KFRP-1010 tensile tests. 169

7.14 (a) UAM 1010-JAC 270 RSW samples before lap shear testing; (b) UAM 1010-JAC 270 RSW samples after lap shear testing. 171

7.15 Load vs displacement curves of UAM 1010-JAC 270 RSW lap shear tests. 172

7.16 Cross-section of an RSW between UAM 1010 and JAC 270: (a) optical image; (b) microhardness map. 174

7.17 KFRP-1010 joint with RSW to JAC 270 and E-coat prior to CCT. . 175

7.18 Galvanic series in ambient seawater [54]. 176

B.1 CFRP samples before and after tensile testing 191

B.2 Stress vs. strain curves of CFRP longitudinal tensile tests 192

B.3 CFRP samples before and after compressive testing 193

B.4 Stress vs. strain curves of CFRP longitudinal compressive tests . . . 194

C.1 Techniques to promote evenly distributed load on the CFRP loops . . 196

C.2 25 mm wide tensile sample after testing. 197

C.3 Load vs. displacement curve of 25 mm wide tensile samples. 197

C.4 Front and back of a 40 mm wide tensile sample: (a) before testing; (b) after testing. 198

C.5 Load vs. displacement curve of 40 mm wide tensile sample. 199

Chapter 1: Introduction

1.1 Literature Survey

1.1.1 Background

Structural lightweighting is critical for achieving improved vehicle fuel economy. A national energy study conducted by the US Department of Energy [42, 21] estimates that a 10% reduction in vehicle mass can lead to 6% reduction in fuel consumption. Due to their high specific strength and high specific stiffness, composites are commonly used in aerospace structures; their use in automotive applications is expected to increase. High-strength organic fibers such as CF or Zylon reach specific strengths that are an order of magnitude greater than typical automotive structural metals [2]. However, low specific toughness, high cost of materials, and complex process requirements make carbon fiber reinforced polymer (CFRP) ill-suited for high-volume automotive manufacturing. Hybrid, multi-material structures that combine the beneficial characteristics of CFRP composites and typical automotive metals are therefore attractive. Methods to reliably join CFRP components to metallic structural components are thus required. The approach proposed in this work consists of using the ultrasonic additive manufacturing (UAM) process to add metal tabs to a CFRP structure, and thus enable joining of the CFRP structure and a metal body via conventional resistance spot welding (RSW). Being able to incorporate CFRP structures into mass-production vehicles without requiring changes to existing metal welding infrastructure would save the automotive industry from making large investments in equipment and training.

1.1.2 Conventional CFRP-to-metal joining methods

CFRP has been joined with metal using adhesives, which presents limitations including long curing time, weak peel strength, and degradation due to aging [4]. Arenas et al. [1] investigated different structural adhesives with various surface pretreatments for CFRP-aluminum alloy (AA) joints. Considering both the mechanical performance and the industrial feasibility, it was found that for polyurethane adhesive, a peel ply CFRP surface and a sandpapering AA surface is the best option, which can generate a joint with a lap shear strength of 12.42 MPa. A peel ply surface for CFRP and a sand blasting surface for aluminum is the most useful surface finish combination for epoxy adhesive, as plotted in Figure 1.1. Ribeiro et al. [36] used adhesive XNR6852 to join CFRP with AA and obtained strength of 21 MPa.

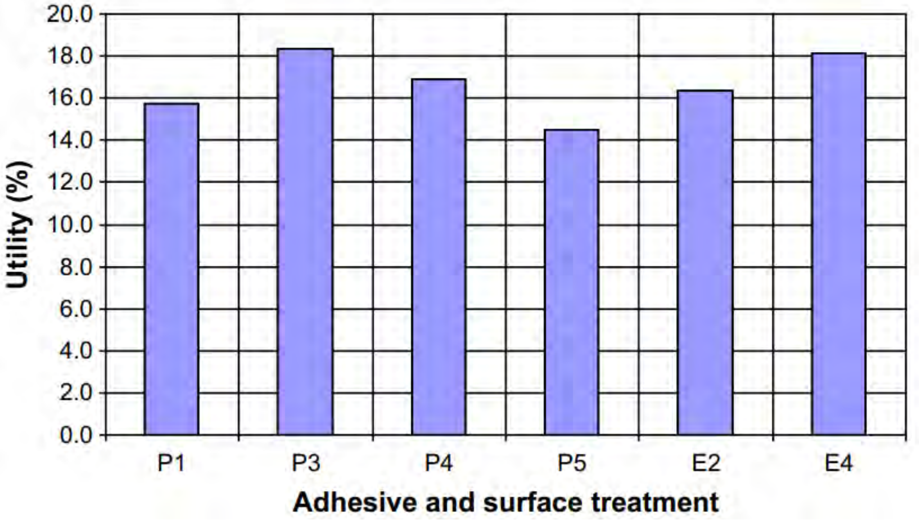

Figure 1.1: Utility of each adhesive and surface treatment; P is polyurethane and E is epoxy [1].

Alternatively, mechanical fasteners can be used for dissimilar material joining. However, fasteners can compromise fatigue life and disrupt the continuity of the joint. Additionally, they are often expensive and require time-consuming drilling processes. The strengths and weaknesses of mechanical joints have been studied by Marannano et al. [32] via double-lap CFRP-AA joints. It was shown that a higher mechanical strength can be obtained by adding steel rivets to CFRP and AA 6082-T6 adhesive joints. However, the riveting process induces delamination in the CFRP around the rivets. Lambiase et al. [24] applied a two-step clinching process and generated a CFRP-AA joint with a 6.6 mm diameter clinching area, as illustrated by Figure 1.2. Tensile tests showed that the lap shear joint carries a peak load of 2.3 kN. A study by Salamati et al. [37] improved the clinching process between aluminum alloy (AA) and CFRP by using electromagnetic discharge energy to accelerate the punch and achieve high-speed clinching. Zhai et al. [56] investigated the strength of countersunk CFRP-AA bolted joints and obtained a lap shear strength of 500 MPa (based on the bearing area).

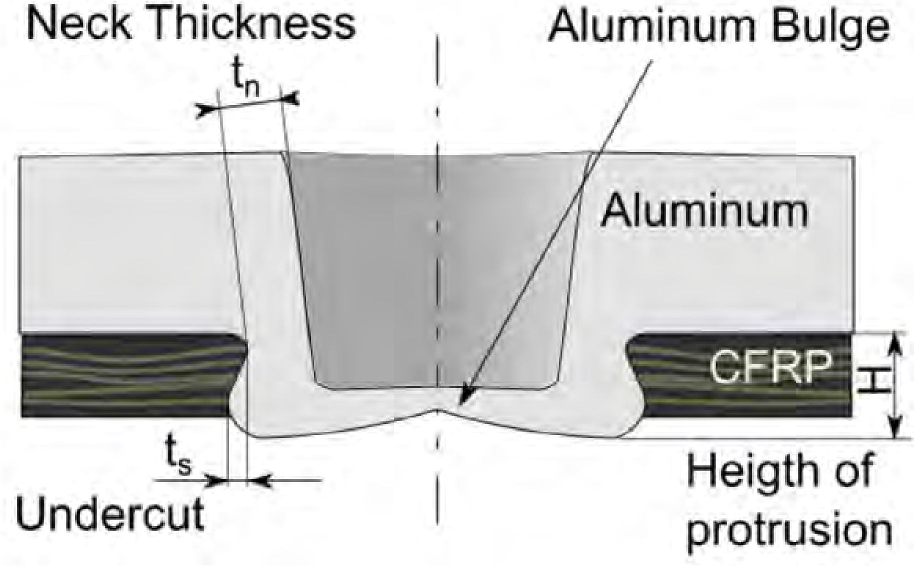

Figure 1.2: Schematic of a AA/CFRP clinched joint cross section [24].

1.1.3 Innovative CFRP-to-metal joining methods

Several innovative welding techniques have been presented for joining CFRP to metals. Balle et al. [3] applied the ultrasonic metal spot welding process to join CFRP to metal sheets. The lap shear strength of a joint between AA 5754 and carbon fiber reinforced Polyamide 66 (PA66) was shown to reach 31.5 MPa. Lionetto et al. [27] modified this joining method by adding a Polyamide 6 (PA6) film on top of the CFRP part before welding. With this modification, the lap shear strength increased to 34.8 MPa. Friction lap joining was proposed by Nagatsuka et al. [34] to directly join CFRP with AA 5052. This method generates joints with a magnesium oxide layer at the interface and produces a joint strength of 2.9 kN for a 225 mm^2 weld area. André et al. [31] applied friction spot joining (FSpJ) to join AA7075-T6 with CFRP and created joints with 4068 N lap shear force. The average lap shear strength of this modified FSpJ joint reaches 52 MPa. Goushegir et al. [10] used the FSpJ method to join a 2 mm thick AA 2024-T3 sheet with a 2 mm thick CF-PPS composite. With phosphoric acid anodizing and primer applied on the aluminum surface before welding, a lap shear peak load of 8788 N was obtained with a nugget diameter of approximately 10 mm. Mitschang et al. [33] reported that a lap shear strength of 14.5 MPa can be obtained by using induction spot welding to join AA 5754 to CF-PA66. Zajkani et al. [55] applied an electromagnetic forming process for CFRP-AA joining and obtained a lap shear force of over 1700 N for a 7.7 mm diameter circular joint region. Research on joining CFRP and AA using ultrasonic torsion welding has been performed by Staab et al. [45], and the joints achieved a tensile shear strength of 83 MPa. A key limitation of these joining methods is the reliance on the strength of the epoxy adhesive to transfer all of the applied load from the fiber to the metal.

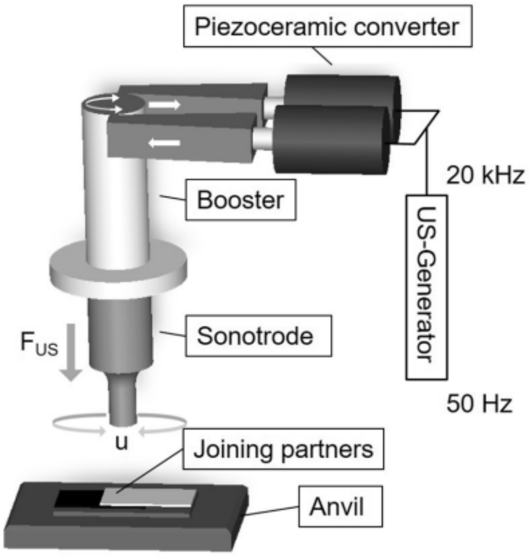
Piezoceramic converter
20 kHz
Booster
US-Generator
F_{US}
Sonotrode
50 Hz
u
Joining partners
Anvil

Figure 1.3: Schematic diagram of an ultrasonic torsion welding system [45].

1.1.4 Ultrasonic additive manufacturing (UAM)

The joining approach presented in this paper employs ultrasonic additive manufacturing (UAM), a solid-state welding technology that incorporates ultrasonic metal welding in a continuous process to build 3D parts from foil stock [51]. The UAM process is illustrated in Figure 1.4. Two piezoelectric transducers vibrate the sonotrode parallel to the welding surface at 20 kHz and an operator-specified amplitude. A metal foil is fed under the textured sonotrode, which applies a normal force and vibrates the foil relative to the base material. The normal and shear forces at the weld interface collapse asperities and disperse oxides. This creates intimate metal-to-metal contact which results in solid-state welding between the foil and substrate.

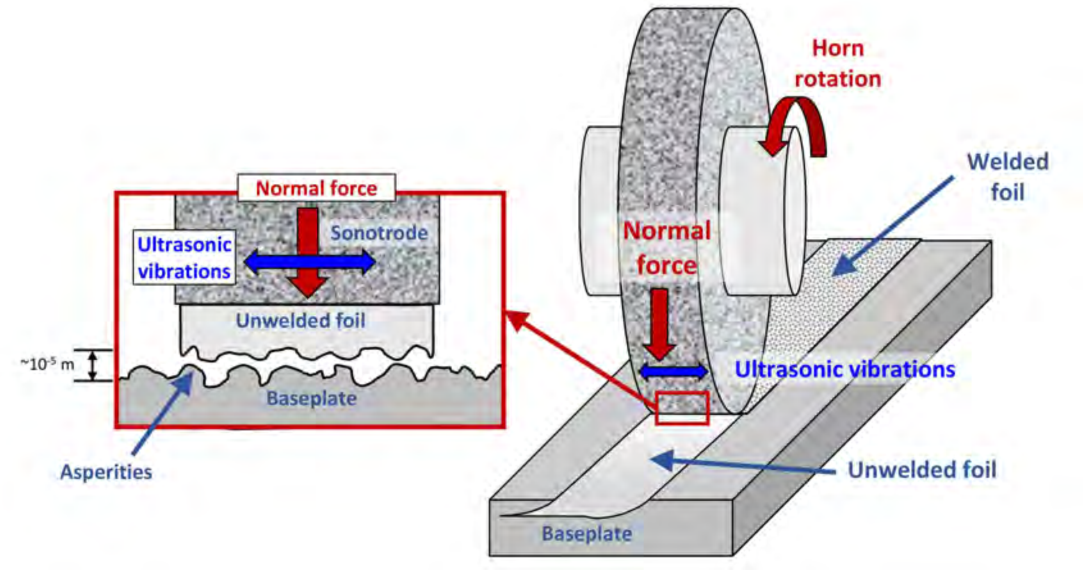
Horn
rotation
Welded
foil
Normal force
Sonotrode
Ultrasonic
vibrations
Unwelded foil
~10^{-5} m
Baseplate
Asperities
Normal
force
Ultrasonic vibrations
Unwelded foil
Baseplate

Figure 1.4: Ultrasonic additive manufacturing process (schematic not to scale). The normal force and lateral vibrations collapse asperities and disperse oxides to produce intimate metal-to-metal contact, resulting in solid-state welding.

UAM is capable of creating high-strength bonds in metals such as AA 6061 [52], stainless steel 410 [16], and many other metals. UAM can also generate bonding between dissimilar materials including AA-steel [44], AA-NiTi [14], and AA-ceramic [9]. The UAM machine includes a built-in computer numerical control (CNC) milling station that enables subtractive milling. Interior features can be created in the metal matrix using the CNC stage during the process. Channels with complex geometries can be machined to house non-metallic materials that can then be encapsulated by welding more foils over the channels. With the solid-state UAM technique, thermally sensitive materials, including reinforcement fibers and sensors, can be embedded into metal structures with full encapsulation [40].

In the UAM process, local temperatures at the weld interface stay below 30% to 50% of the melting temperature of the foil stock [23]. This characteristic makes UAM a suitable method to embed a variety of materials including temperature-sensitive materials and sensors. Hahnlen et al. [12, 13] used UAM to embed thermally-sensitive shape memory NiTi fibers into aluminum, which has the effect of reducing the coefficient of thermal expansion of the composite relative to aluminum. Although no metallurgical bonding was shown between the NiTi and AA matrix, interfacial strength arising from friction coupling was demonstrated using pullout tests and finite element analysis [18]. Delicate sensors such as fiber Bragg grating (FBG) can also be embedded into an aluminum matrix via UAM [41]. The UAM technology is not only able to weld thin foils, but can also weld thick aluminum sheets as demonstrated by Wolcott et al. [53] in a study on seam welding between 1.93 mm thick aluminum sheets.

1.2 Objectives

The goal of this research is to develop a method for joining carbon fiber composites to metal structures using UAM that causes minimal disruption to the existing factory infrastructure. The key feature is a hybrid metal-carbon fiber transition structure that is integrated with the carbon fiber components and serves as a weld tab for joining carbon fiber panels to traditional body in white (BIW) metals using resistance spot welding (RSW). The first objective is to develop a manufacturing process to produce the CF-AA joints by UAM. A sheet welding method is employed to enable CF encapsulation while avoiding foil tearing. To characterize the mechanical property of the UAM CFRP-AA joints, tensile and cross-tensile tests were performed on the coupons. Structural tests were also conducted in four-point bend, axial crush, and torsion. Analytical and finite element models of the mechanical tests were created to provide joint design and application insight.

To enable the application of the transition structure as weld tabs, another objective is to investigate the impact of RSW on the joint. RSWs were performed between a UAM 6061 sheet and a bulk AA sheet to investigate the heat affected zone (HAZ) via microhardness mapping. Mechanical degradation due to fiber damage caused by the heat during RSW was also experimentally studied. Galvanic corrosion mitigation is another objective of this study. The difference in electrical potential makes CFRP and metal a perfect galvanic couple. The metal would corrode severely if no protection is applied to the joint. A countermeasure of using non-conductive Kevlar fiber as insulation is developed and evaluated.

The last objective is to expand the matrix material from AA to steel, which is more commonly used as the structural material in automotive industry. A study has been carried out to develop a UAM process to create voidless high-strength bonding between 1010 steel foils. With the developed method, KFRP-steel joints are created using UAM.

1.3 List of acronyms

Table 1.1: List of acronyms

AA	Aluminum alloy
BIW	Body-in-white
CCT	Cyclic corrosion test
CF	Carbon fiber
CFRP	Carbon fiber reinforced polymer
CNC	Computer numerical control
CTS	Cross-tensile strength
DIC	Digital image correlation
DOE	Design of experiments
FEA	Finite element analysis
FRP	Fiber reinforced polymer
HAZ	Heat-affected zone
KF	Kevlar fiber
KFRP	Kevlar fiber reinforced polymer
RSW	Resistance spot weld
SEM	Scanning electron microscope
UAM	Ultrasonic additive manufacturing
UTS	Ultimate tensile strength

Chapter 2: CFRP-AA Joint Using UAM

In this study, UAM is used to embed dry CF fabric within AA; a key characteristic of our approach is that the CF-AA UAM joints are created before layup and curing of the CF within a CFRP composite structure. In contrast, most other CFRP-AA joining methods connect a cured CFRP laminate to a metal structure. Our joint design avoids the damage to the CFRP associated with drilling holes for fasteners and is able to create a strong mechanical connection between the dissimilar materials. Mechanical interlocking of CF loops in the AA matrix, facilitated by the UAM process, provides direct load transfer. This is in contrast to conventional joining methods where epoxy is a primary load-carrying component of the joint. Rather than creating a traditional joint with overlapping CFRP and metal regions, UAM makes it possible to create joints with a uniform thickness across the CFRP and AA constituents. To illustrate, a CFRP-AA demonstration part has been made (Figure 2.1). Aluminum flanges were joined to the dry CF via UAM, followed by the creation of the CFRP beam (using standard CFRP processes), and subsequent welding to an aluminum plate via conventional resistive spot welding. This chapter describes the manufacturing process that enables the creation of UAM CF-AA transition joints. Optical imaging and mechanical testing of cured CFRP-AA transition joints are presented which illustrate the mechanical properties of the joints. Tensile tests elucidate that two different failure modes are possible, paving the way for joints that can be designed for maximum mechanical strength or maximum energy dissipation.

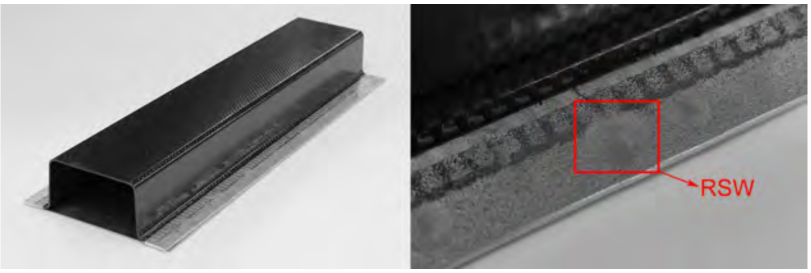

Figure 2.1: Example hybrid CFRP-metal hat structure with UAM transition joints and RSW welds to connect the AA transition to a flat metal sheet (at the bottom of the hat).

2.1 Material and methods

2.1.1 Materials and components

The CFRP component includes bidirectionally woven 3K carbon fiber fabric tape supplied by Fibre Glast Developments Corp. In this carbon fiber product, a single CF tow is woven from side-to-side, forming the weft and producing loops along the sides. The CFRP laminate is prepared with System 2000 epoxy paired with System 2120 hardener. Both the epoxy and the hardener are supplied by Fibre Glast Developments Corp. The resin and hardener are mixed at a ratio of 1:0.27 by weight. After applying the mixture to CF fabrics, the laminate is vacuum bagged and cured at room temperature. The experimental ultimate tensile strength (UTS) of each constituent material of the CFRP-AA joint sample is listed in Table 2.1. The UTS of the CFRP tow was measured by testing a single carbon fiber tow cured with epoxy; the area used for the CFRP tow strength calculation is based on a 7 μm fiber diameter (from

SEM measurements) and the voids or epoxy among the fibers are not accounted for in the strength calculation. AA 6061-H18 foil is used as the feedstock for the UAM process. This is an annealed ASM standard AA 6061 material that has been fully work hardened [51]. The foil has a thickness of 0.152 mm and width of 25.4 mm. Foils are welded as-received, with no cleaning or pre-treatment applied. The UTS for UAM welded AA 6061 was measured by tensile tests of dogbone samples.

Table 2.1: Experimentally measured ultimate tensile strengths of CFRP-AA joint materials.

	UTS
CFRP component	587 MPa
CFRP tow	1.73 GPa
UAM welded AA 6061	195 MPa

2.1.2 Sample preparation

Key to manufacturing CFRP-AA joints by UAM is to embed carbon fiber tows in the AA matrix, creating internal mechanical interlocking between the dissimilar materials. Figure 2.2 shows a schematic of the manufacturing progression.

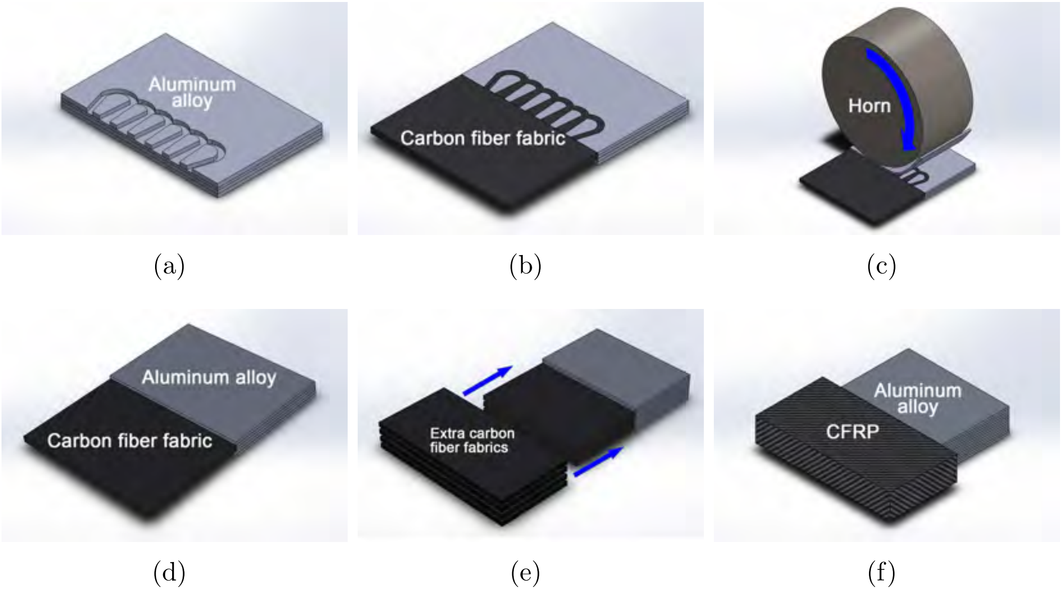

(a) (b) (c)

(d) (e) (f)

Figure 2.2: CFRP-AA joint manufacturing process schematics: (a) AA matrix is built with UAM and channels are machined; (b) dry CF tow loops are placed in the channels; (c) one layer of AA foil is welded by the UAM horn; (d) one layer of CF tow loops is embedded; (e) three layers of CF tows are embedded by repeating steps (a) to (d), extra CF fabrics are inserted to match the thickness of CFRP to AA; (f) CFRP is cured with epoxy to complete the CFRP-AA joint.

The manufacturing process is illustrated in Figure 2.3. A section of the CF foil is cut out and some of the longitudinal tows that make up the warp of the fabric are removed to expose CF weft loops. To ensure that the tows are well situated in the channels and to avoid any drifting during the welding process, a light coating of spray adhesive is applied to the tows before placing them in the channels. An AA 6061 sheet is welded over the channels containing the tows [48]. Rather than using an automatically-fed AA 6061 tape foil, a layer of AA 6061-H18 sheet foil is secured over the sample with vacuum. The thickness of the AA sheet is the same as the typical AA tape foil used in UAM, though the sheet material is wider and can be trimmed to size as required to cover the sample. After a weld pass, the extra sheet material is removed from the sample. Following the sheet layer, several layers of AA 6061 tape foil are added to build up sufficient height for cutting additional channels and embedding more layers of CF fabric. After the welding process, a vent hole is drilled at the top of each loop to allow air to escape during vacuum bagging and ensure that the epoxy can fully wet the embedded CF loops. After the baseplate is removed using subtractive milling operations on the UAM system, the transition joint is laid up with additional CF fabric plies in between and on the outside of the embedded layers using epoxy. Samples 25.4 mm wide are cut from the final build for tensile testing.

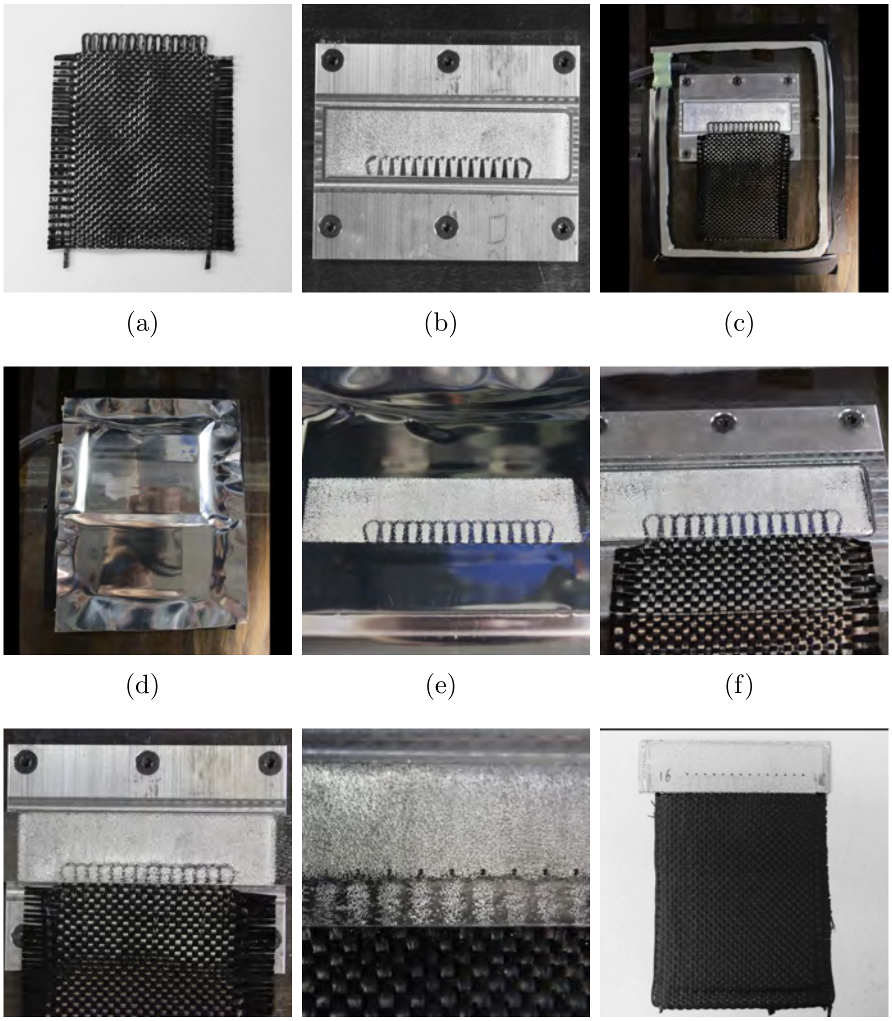

(a) (b) (c)

(d) (e) (f)

(g) (h) (i)

Figure 2.3: CFRP-AA transition joint manufacturing progression: (a) CF fabric is prepared by removing multiple warp tows; (b) four layers of AA 6061 tape foil are welded on the baseplate and the channels are cut into the AA matrix; (c) CF loops are placed into the channels with the aid of spray adhesive. Vacuum putty is set up around the sample with a vacuum hose passing through; (d) a layer of cleaned AA 6061 sheet foil is placed on the sample and secured by vacuum; (e) the AA 6061 sheet foil is welded over the CF tows using UAM; (f) extra sheet material is removed; (g) additional AA 6061 foils are welded over the base aluminum; (h) vent holes are drilled at the top of each loop; (i) additional CF fabrics are inserted into the CF part, and the joint is cured with epoxy in a vacuum bag at room temperature.

The CF tows are encapsulated in n-shaped channels, as shown in Figure 2.4, with dimensions that correspond to the weft loops at the edge of the CF tape. The channel depth determines how compacted the fibers become during embedding. If the channels are over-filled, the fibers may not stay in the channel during welding or tearing of the foil being welded may occur. Considering these factors, the design shown in Figure 2.4 has deeper channels where neighboring CF tows overlap to accommodate the increased volume of carbon fibers. In the schematic, the darkness of the grey shading indicates the depth of the channel. The depth increases linearly from 0.18 mm to 0.36 mm to accommodate the transition from one to two CF tows.

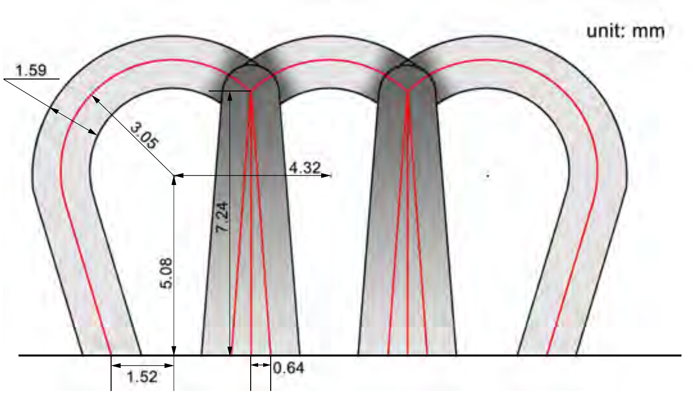

Figure 2.4: Schematic of looped channels to house the dry CF tows.

In this study, UAM transition joint coupons are fabricated with several layers of carbon fiber fabric embedded into an AA 6061 matrix. Side view schematics of two sample constructions for tensile testing are illustrated in Figure 2.5 (a) and (b). For the 3-CF-layer sample, there are 12 layers of AA 6061 foils, 3 embedded plies of CF fabric, and 4 layers of non-embedded CF fabric to preserve sample thickness. The

4-CF-layer sample has 4 layers of CF loops embedded into the AA matrix, which is made from 15 foil layers and 5 layers of non-embedded CF fabric. The thickness of the AA is 1.8 mm and 2.2 mm for the 3 and 4-CF layer builds, respectively.

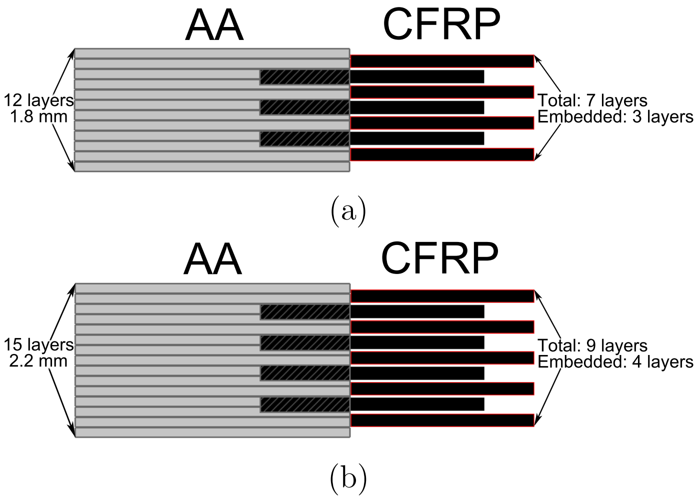
AA
CFRP
12 layers
1.8 mm
Total: 7 layers
Embedded: 3 layers
(a)
AA
CFRP
15 layers
2.2 mm
Total: 9 layers
Embedded: 4 layers
(b)

Figure 2.5: (a) Schematic cross section of 3-CF-layer transition joints; and (b) schematic cross section of 4-CF-layer transition joints. The CFRP component shown represents the CF after layup and cure in epoxy. (Schematics not drawn to scale.)

The parameters used to weld AA 6061-H18 are listed in Table 2.2. The welding parameters for tape foils follow the optimization result from a DOE study carried out by Wolcott et al. [52]. A lower amplitude is used for sheet welding to avoid foil tearing or nuggeting of the sonotrode. To compensate for the decrease in energy input, a lower welding speed is employed. This parameter set is typical for aluminum-to-aluminum UAM sheet welding.

Table 2.2: Welding parameters for AA 6061-H18.

	Force (N)	Amplitude (μm)	Speed (cm/s)	Dwell time (ms)
AA 6061-H18 sheet foil	4000	30	3.4	150
AA 6061-H18 tape foil	4000	32	8.5	300

2.2 Optical imaging

Optical images of the hybrid joint were taken from a 3-CF layer sample to investigate the interface between an embedded CF tow and the AA matrix. Figure 2.6 shows two typical CFRP-AA interface characteristics at the channel side walls. The channels that accommodate the CF tows are slightly oversized in order to preserve tow integrity. In some regions, the CF tow is compactly encapsulated by the AA matrix, as shown in Figure 2.6 (b). It is also possible for the CF tow not to completely fill the channel, which leaves a space between the CF tow and the channel wall. However, when the sample is cured with epoxy, the vent holes ensure that the epoxy flows into the channel and completely fills the spaces, as pictured in Figure 2.6 (c). Oversizing the AA channels does not appear to harm the performance of the joint. On the contrary, the oversized channel design not only protects the CF tows from any damage due to welding, but also gives the epoxy the space needed to flow and consolidate the CF tows. It is emphasized that the primary role of epoxy in the channels is not to provide adhesion between the CF and AA since strength is provided by mechanical interlocking of the fiber loops in the matrix. Rather, consolidation of the tow provides load sharing between fibers to promote concurrent failure, thus improving strength.

The epoxy present in the joint also helps to promote failure at two locations for each loop rather than just one failure point at the top of each loop during tensile testing, which is the typical failure mode when dry fibers are pulled around a pillar or rod.

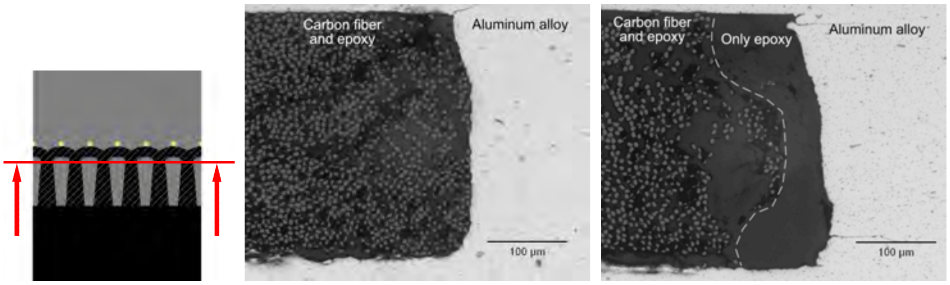
Carbon fiber and epoxy
Aluminum alloy
100 μm
Carbon fiber and epoxy
Only epoxy
Aluminum alloy
100 μm

(a) (b) (c)

Figure 2.6: CFRP-AA interface at the channel side walls: (a) cross-section imaging location; (b) channel tightly packed with CF; and (c) channel that is not completely filled by CF where epoxy has flowed to fill the space between the CF and AA during layup.

Images of the CFRP-AA interface in Figure 2.7 show the difference between the upper and lower edges of the CF tow. Because the normal force applied during the welding process squeezes the CFs in the channel, some CF fibers are pushed into the AA matrix.

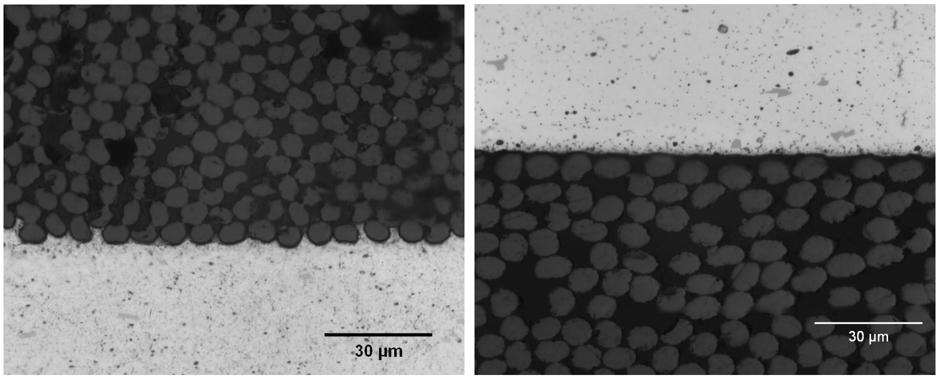

(a) (b)

Figure 2.7: CFRP-AA interface at the (a) lower edge and (b) upper edge of the embedded tow.

2.3 Tensile test

Tensile tests were conducted on 25.4 mm wide UAM CFRP-AA transition joint samples (3-CF-layer and 4-CF-layer) on an MTS C43-504 load frame at a crosshead speed of 5 mm/min. The schematic of the samples is shown in Figure 2.8. During the tests, a Correlated Solutions VIC-3D DIC system was used to evaluate the strain distribution and measure the local displacement in the joint area. A 20-mm virtual gauge length across the joint region was used for measuring displacement. A force vs. displacement curve was plotted based on force data from the frame's load cell and the local displacement data measured by the DIC system.

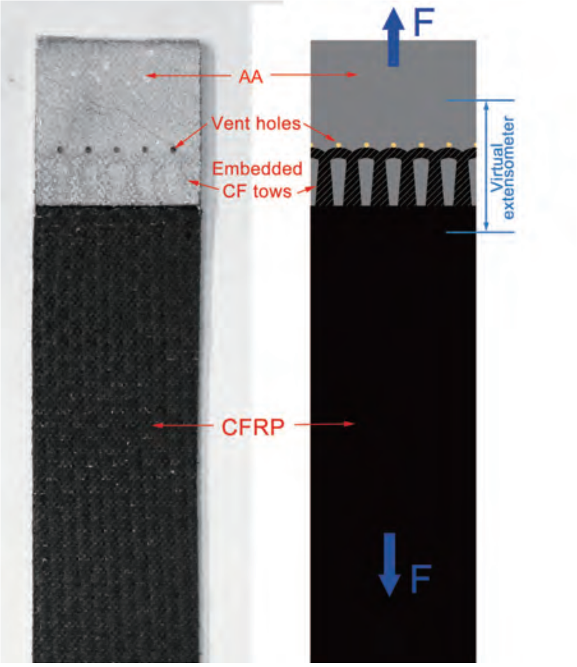

(a) (b)

Figure 2.8: CFRP-AA tensile samples: (a) picture and (b) schematic.

The load vs. displacement curves are plotted in Figure 2.9. Because the sampling frequency of the DIC cameras is only 4 Hz, undersampling occurs as evidenced by the straight lines in the 3-CF-layer curves. The average peak load of the 3-CF-layer samples is 4677 N while the average peak load of the 4-CF-layer samples reach 7238 N. Two failure modes are observed. The 3-CF-layer samples fail in the CF tows and the 4-CF-layer samples fail in AA matrix. The average energy absorbed by the 3-CF-layer samples is 3.96 J, which is 4 times greater than the 0.9 J absorbed by the 4-CF-layer samples. The strain distributions and images of tested specimens will be illustrated and discussed for each failure mode.

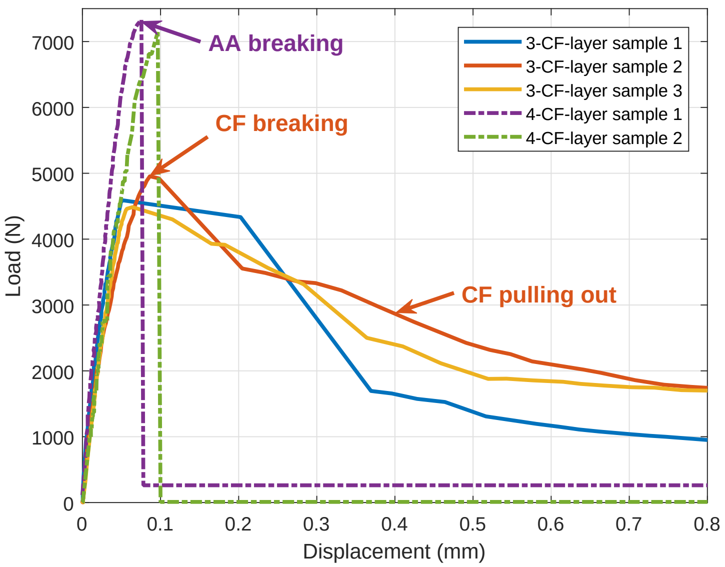

Figure 2.9: Load vs. displacement curves for tensile tests on 3-CF-layer and 4-CF-layer samples. The straight lines are caused by undersampling of the DIC system's cameras.

2.3.1 CF tow failure

CF tow failure is the failure mode observed in the tensile testing of all 3-CF-layer UAM joints. Embedded carbon fiber loops break within the straight region of the channel loop, leaving the curved parts in the AA matrix. This failure mode is characterized by the CF tow loops breaking at two locations. The average peak tensile load for this sample design is 4677 N. Considering the joint's cross sectional area, the tensile strength is 102.3 MPa. As shown in Figure 2.9, the highest peaks in the 3-CF-layer load vs. displacement curves correspond to the CF breaking point, and the tail after the peak load is from friction during fiber pullout. The energy absorption of this failure mode is high due to the friction pullout. From the DIC strain map shown in Figure 2.10, the strain is evenly distributed at the beginning; as the load builds, the strain concentrates at the CFRP-AA interface as shown in Figure 2.10 (c). The CF tows carry load by pulling on the AA columns around which they are looped. The aluminum to CFRP tab interface breaks when the local true strain reaches 2%. As the load reaches a maximum value, the carbon fiber loops break and are pulled out after failure, shown in Figure 2.10 (d). This CF pullout process contributes to the high energy absorption (3.96 J at 0.8 mm displacement). From the pictures of a failed sample shown in Figure 2.11, there is no delamination or AA shearing, which indicates that the UAM weld quality is high enough to avoid failure of the UAM weld in tensile testing.

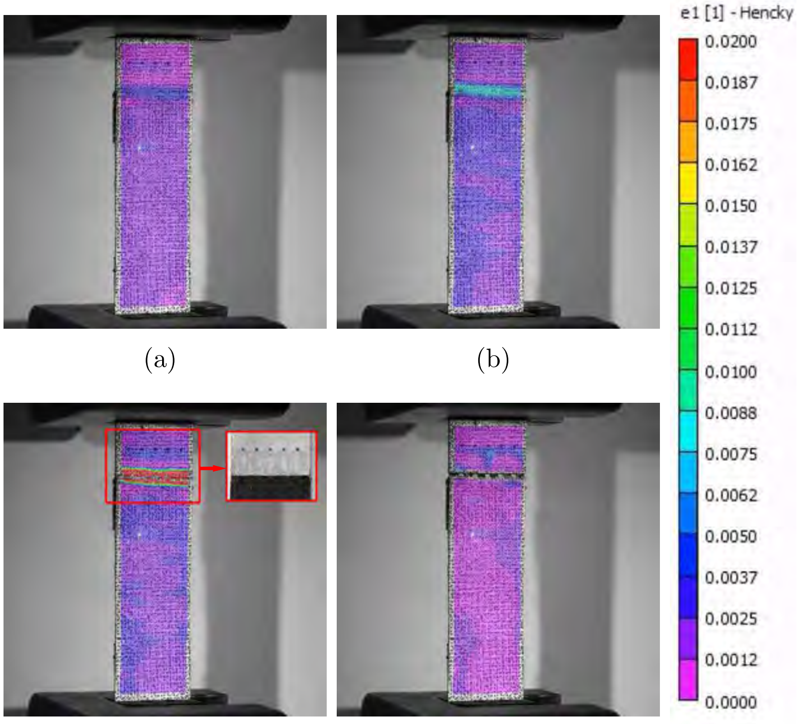
e1 [1] - Hencky
0.0200
0.0187
0.0175
0.0162
0.0150
0.0137
0.0125
0.0112
0.0100
0.0088
0.0075
0.0062
0.0050
0.0037
0.0025
0.0012
0.0000

(a) (b)

(c) (d)

Figure 2.10: DIC strain maps at different displacements for 3-CF-layer sample 2: (a) 0.036 mm; (b) 0.057 mm; (c) 0.086 mm; and (d) 1.44 mm of displacement. Failure takes place in the CF tows.

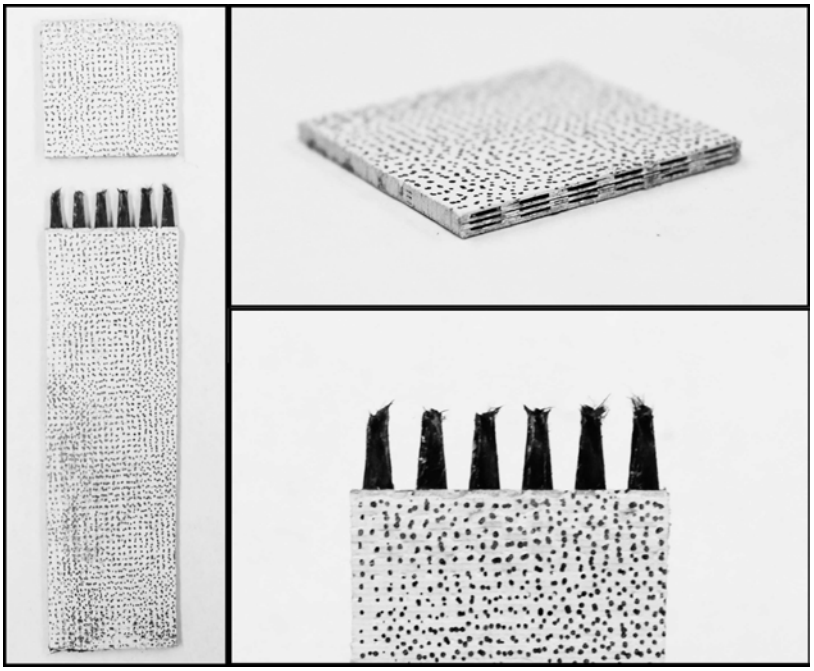

Figure 2.11: 3-CF-layer sample after tensile testing (speckled for DIC measurements).

In these samples, the CF tows are the weaker component when compared to the AA matrix. As illustrated in Figure 2.12, there are 10 CF tows per CF layer that carry load in a 25.4 mm wide sample. According to the single CFRP tow tensile test mentioned earlier, the peak load of each 3K CF tow is 200 N on average. Assuming the load is distributed uniformly among the CF tows, a 25.4 mm wide, 3-CF-layer CFRP-AA joint with 30 CF tows should be able to carry 6000 N. Referring to Figure 2.9, the difference between this calculation and the observed failure load may be explained by: (1) broken fibers observed in the CF tow loops of the as-received woven tape, which decreases the number of load-carrying CF fibers in each tow; and (2) nonuniform loading of CF tows leading to asynchronous failure of the carbon fibers. These two factors reduced the load carrying capacity of the 30 loaded CF tows by 1323 N, on average.

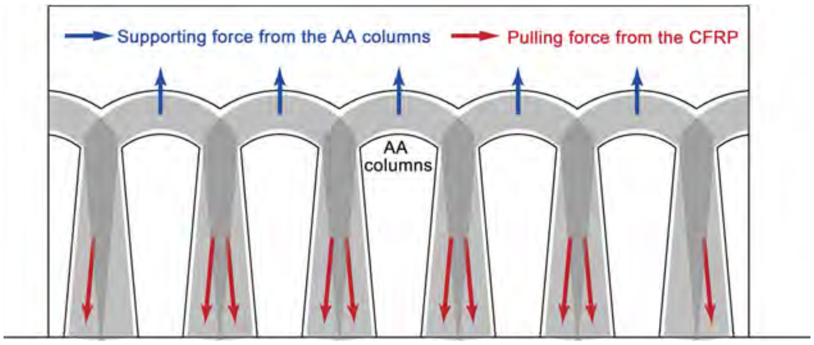
Supporting force from the AA columns
Pulling force from the CFRP
AA columns

Figure 2.12: Loading diagram of one layer of CF loops in a 25.4 mm wide sample.

2.3.2 AA matrix failure

The 4-CF-layer builds failed by breaking of the AA matrix. Analysis of the fracture surfaces (Figure 2.13) shows that the CFRP-AA joint interface was intact while the AA matrix failed in the stress concentration directly above the channel loops. This suggests that the UAM CFRP-AA joint is stronger than the AA matrix. The vent holes shown by the arrow are filled with epoxy; because epoxy is applied to the dry fabric outside of the UAM region before vacuum bagging, this indicates that the channels that house the CF tows are completely wetted. From the DIC strain map shown in Figure 2.14, the strain initially concentrates at the interfacial CFRP-AA area from the right side of the joint, shown in Figure 2.14 (b). As strain at the interface increases, severe strain concentration occurs at the top-of-loops region indicated in Figure 2.14 (c). Finally, the AA matrix cracked along the top edge of the loops when the strain of the AA matrix at the top-of-loops region reached 0.6%, leading to aluminum matrix failure shown in Figure 2.14 (d). The average peak load for the samples is 7238 N, which corresponds to a stress of 129.5 MPa. The only peak in the load vs. displacement curve in Figure 2.9 corresponds to failure of the AA matrix. The load drops to zero after this peak because the sample failed outside of the joint region, resulting in no fiber pullout.

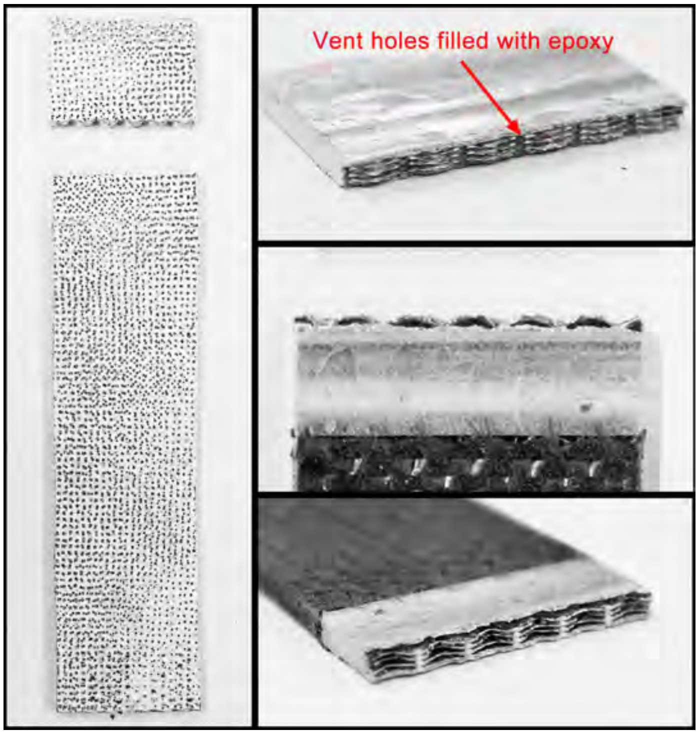

Figure 2.13: 4-CF-layer sample after testing (speckled for DIC measurements).

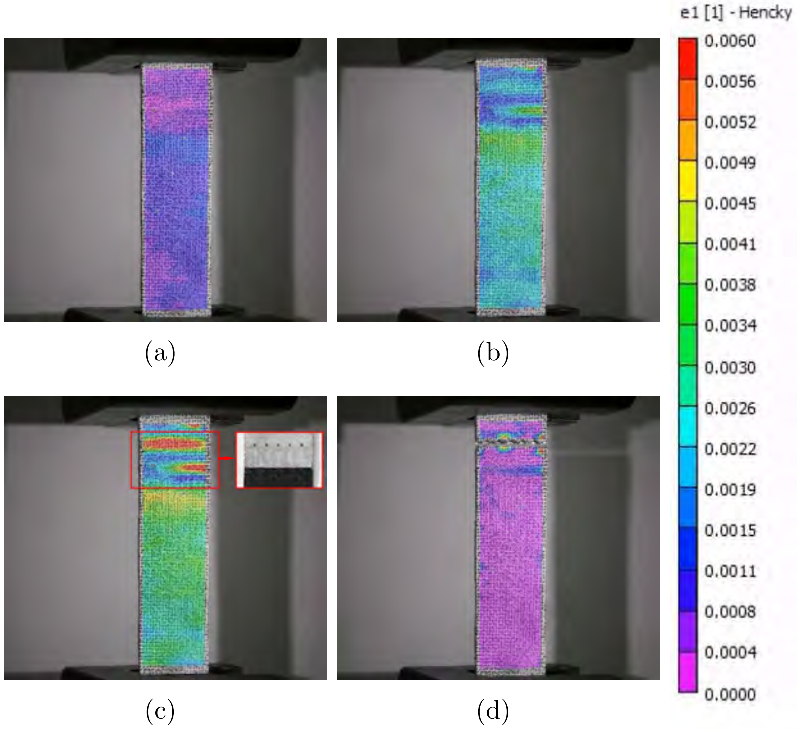

(a) (b)

(c) (d)

Figure 2.14: DIC strain maps at different displacements for a 4-CF-layer sample failing in the AA matrix: (a) 0.011 mm; (b) 0.045 mm; (c) 0.076 mm; and (d) 2.13 mm.

The schematic of the projection perpendicular to the loading direction of the surface along the AA failure interface is shown in Figure 2.15. The projected area of the AA matrix along the failure interface is 36.06 mm^2. Since the UTS of the AA matrix (UAM welded AA 6061-H18) is 195 MPa, the theoretical peak load of this failure mode is 7032 N. The difference between experimental and theoretical peak loads may be caused by the adhesive strength of the epoxy at the end of the CFRP tows and vent holes.

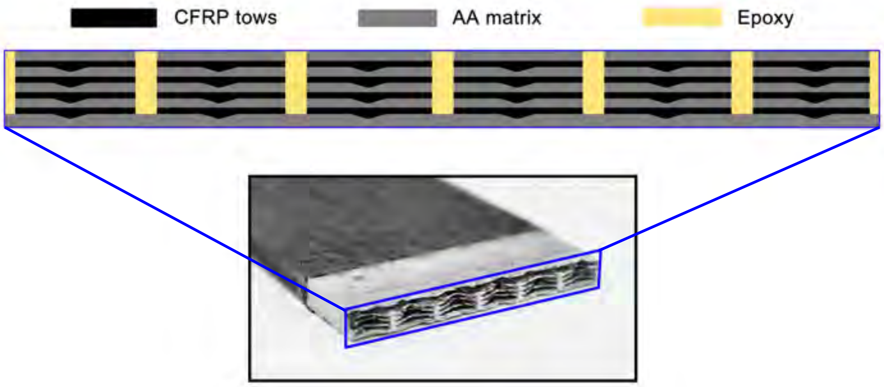

Figure 2.15: Schematic of the projection of an AA failure interface.

2.4 Cross-tensile test

The cross-tensile (CTS) tests were performed based on the JIS 3137 standard. The samples were prepared with the dimensions specified by the standard, shown in Figure 2.16. The samples were designed with three layers of CF fabric with ten loops embedded along both sides of an AA strip to produce 2 CFRP tabs on each test sample. The AA matrix of the samples was welded by nine layers of tape and three layers of sheet, which is identical to the configuration of 3-CF-layer samples in Section 2.1.2. All the tape layers were welded in a configuration with two tapes side-by-side to make the AA part 50 mm wide. The samples were tested on an MTS load frame at the rate of 10 mm/min. The setup is shown in Figure 2.17. Pictured in Figure 2.18 are the CTS samples before testing.

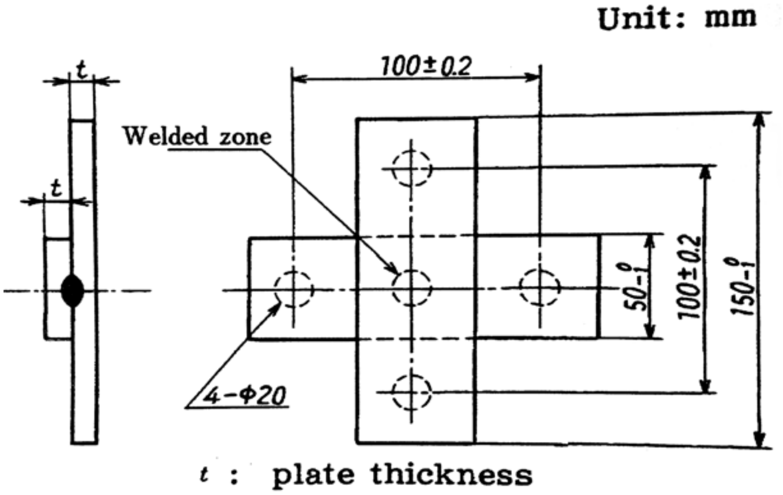
Unit: mm
t
t
100±0.2
Welded zone
50-1 0
100±0.2
150-1 0
4-Φ20
t : plate thickness

Figure 2.16: Shape and dimensions of CTS test pieces from JIS 3137.

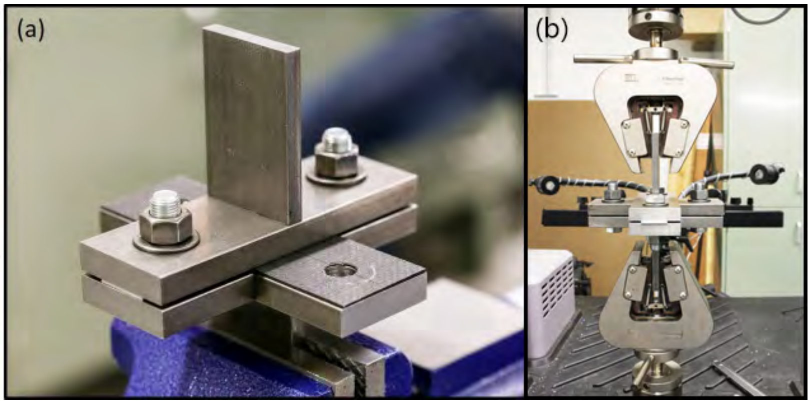

Figure 2.17: (a) Fixture for cross-tension tests; (b) cross tensile testing setup consisting of an MTS load frame and the fixture.

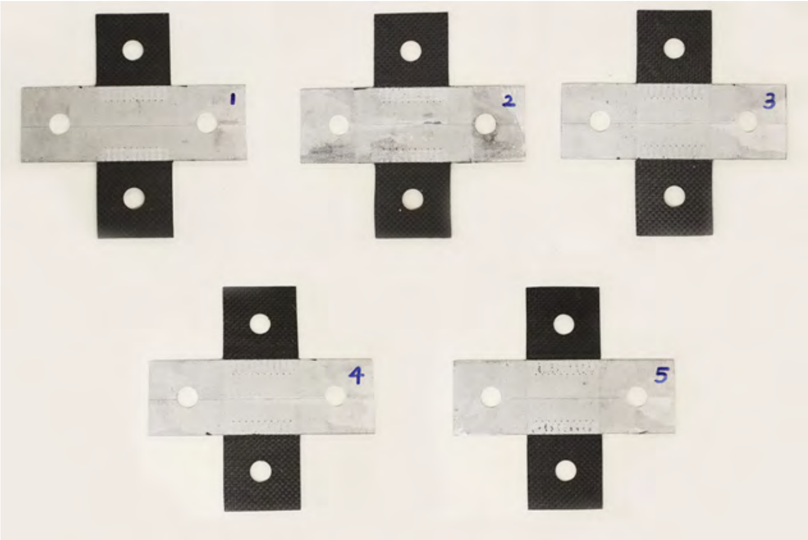

Figure 2.18: CTS samples before testing.

Figure 2.19 shows the load vs. displacement curves for five samples recorded by the load frame. It is noted that the displacement data indicates the crosshead displacement and is not a measurement based on DIC data. The peak loads and failure modes are listed in Table 2.3. Figure 2.20 shows the images of failed samples. For sample 3, one side failed by AA delamination, and the CF loops pulled out, indicating the sample's weaker AA-AA bonding strength. Most of the samples failed by shearing the CF tows along both edges of the joints.

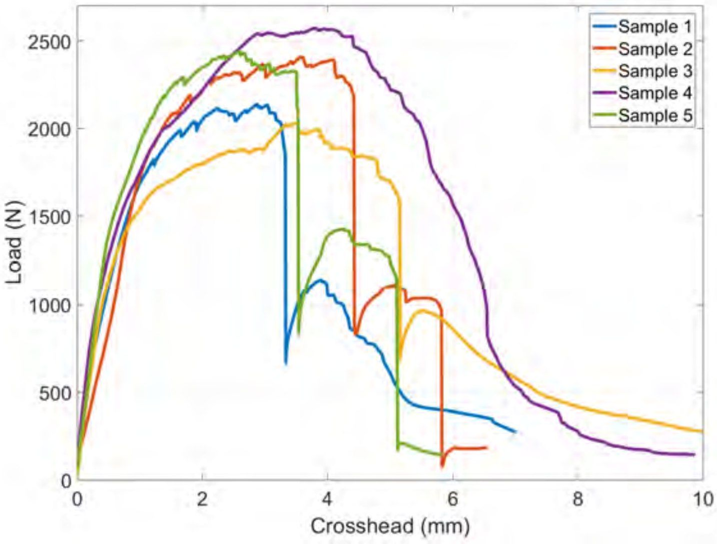

Figure 2.19: Load vs. displacement plot for the CTS samples.

Table 2.3: Peak loads of cross-tension tests

	Peak load	**Failure mode**
Sample 1	2138 N	Mostly CF tows shearing with three tows pullout
Sample 2	2409 N	CF tows shearing
Sample 3	2030 N	CF tows shearing on one side, AA delamination on the other side
Sample 4	2571 N	CF tows shearing
Sample 5	2442 N	CF tows shearing
Average	2318 N	
Standard deviation	225 N	

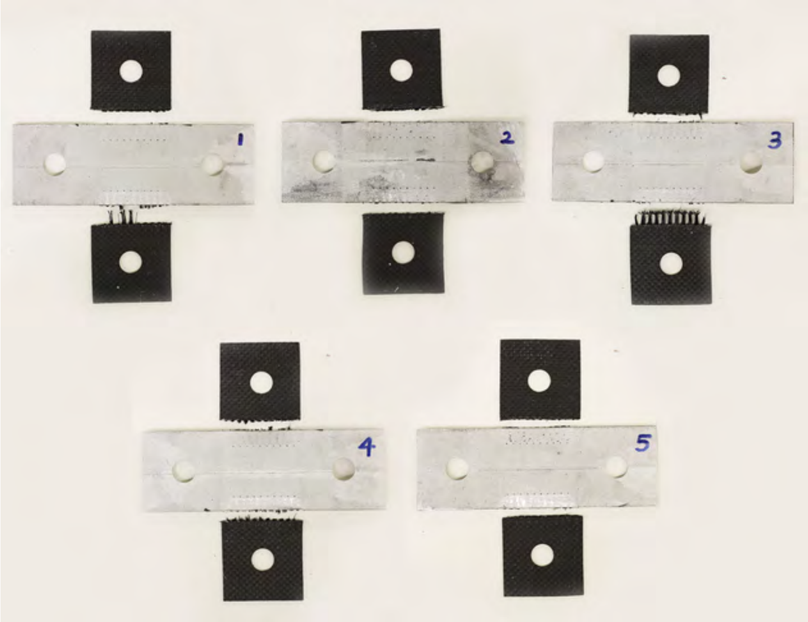

Figure 2.20: CTS samples after testing.

2.5 Summary

Ultrasonic additive manufacturing was applied to create joints between AA 6061 and CFRP by mechanical interlocking, producing a high-strength joint with distinct features relative to existing techniques. One feature is the designable failure mode. Samples with 3 layers and 4 layers of CF were built and mechanically tested. Tensile tests show that the peak loads for 1.8 mm thick 3-CF-layer samples and the 2.2 mm thick 4-CF-layer sample are 4677 N and 7238 N, respectively. The failure modes of both sample geometries were analyzed by strain distribution maps recorded through DIC. Failure mechanism analyses on both sample constructions demonstrate that the failure mode, i.e., CF tow failure or AA matrix failure, can be designed by tuning the CF/AA ratio. The ideal failure mode for CFRP-AA joints may vary in different situations. Since UAM is an additive manufacturing process, the failure mode of the joints can be designed by simply adjusting the number of AA and CF layers. For example, if the thicknesses of the aluminum and CFRP parts are given, a larger number of embedded CF layers will result in AA failure, providing an efficient joint in terms of specific strength and stiffness, while a CF failure mode can be created by embedding fewer CF tows, resulting in higher energy absorption. This ability to change the CF:AA ratio to achieve a predicted performance outcome is an important feature of the UAM CFRP-AA joint. Another special characteristic of the UAM CFRP-AA joint is that it maintains the thickness of the aluminum part across the joint; the joints require no overlaps and associated discontinuities. The looped channel geometry makes it possible to create a continuous joint between CF and aluminum with any arbitrary interface profile. With the approach presented here, metal tabs can be added to CFRP parts for subsequent welding of these parts to the metal structure via resistance spot welding. The ability to integrate CFRP structures and metal structures without requiring changes to existing metal welding infrastructure is regarded as a major benefit of the approach presented here. Although this study focused on AA-CF transitions, this design can be optimized for other metal-fiber combinations.

Chapter 3: Effect of RSW on CFRP-AA UAM Joints

A study has been conducted to investigate the feasibility of joining the CFRP-AA transition joints to metal structures. The RSW weldability between UAM 6061-H18 and AA 6061-T6 has been investigated. Microhardness mapping has been performed to characterize the heat affected zone of the RSW. The safe location of the RSW has been experimentally investigated to avoid strength compromisation due to RSW.

3.1 Investigation of the effect of RSW on UAM aluminum

One-inch wide AA 6061-H18 strips were created by welding 12 layers of foil tapes using UAM, which matches the thickness of 3-CF-layer samples in Section 2.1.2. The strips are then joined to bulk 6061-T6 strips via RSW to create samples for tensile and cross-tensile tests. Twenty-four samples were prepared in total, 12 of them being UAM 6061-H18 joined to bulk AA 6061-T6, and 12 of them being bulk AA 6061-T6 sheets joined together. Table 3.1 listed the weld parameters used for the UAM parts. The RSW parameters are listed in Table 3.2.

Table 3.1: UAM weld parameters

Welding Force	5000 N
Welding Speed	127 cm/min
Amplitude	32 μm
Heat-plate Temperature	Room Temperature (22 °C)
Spot Dwell	300 ms
Sonotrode Roughness	14 μm Ra

Table 3.2: RSW parameters for UAM 6061-H18 and bulk 6061-T6

Cycles	Hold 10 – Weld 10 – Hold 10 (60 Hz)
Current	38 kA
Force	350 kg
Tip	16 mm DR50

3.1.1 Tensile testing

Figure 3.1 and Figure 3.2 show the samples before and after tensile testing, respectively. All the UAM-bulk samples failed by a plug from the UAM side of the joint as shown in the red box. Sample 3 of the bulk-bulk case failed with plug fracture. All the other bulk-bulk samples failed by interface fracture, pictured in the yellow box from Figure 3.2, which indicates good quality of the RSW. Figure 3.3 shows the load vs. crosshead displacement curves for all tests. The curve shapes are consistent within each case. The only bulk-bulk curve with a similar shape to UAM-bulk curves is sample 3, which exhibits plug fracture (same as UAM-bulk sample failure mode). The peak loads and nugget dimensions for the tensile samples are listed in Table 3.3. The average peak loads for UAM-bulk and bulk-bulk samples are 5115.2 N and 6843.5 N, respectively. The strength of bulk-bulk samples is higher than UAM-bulk samples, which is presumably due to the higher strength of the AA 6061 due to T6 heat treatment. From the table, it can also be found that a higher peak load usually corresponds to a larger nugget diameter.

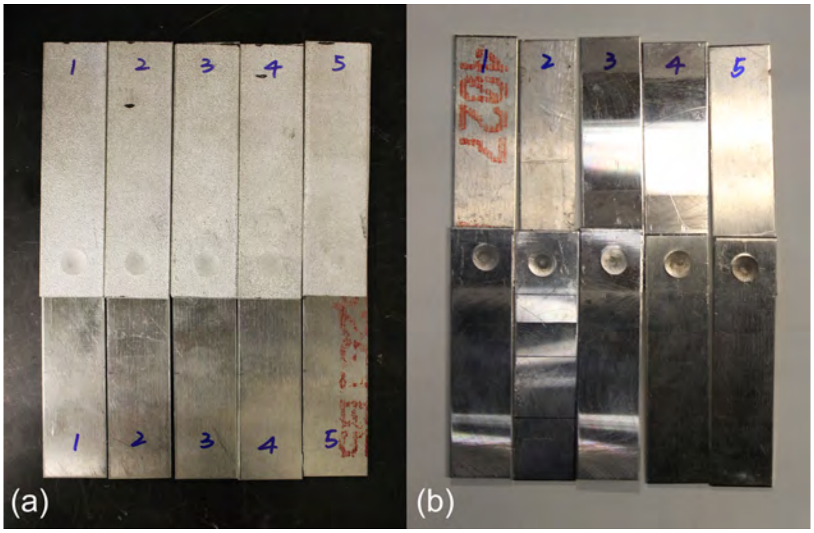

Figure 3.1: Tensile samples before testing: (a) UAM-bulk samples; (b) bulk-bulk samples

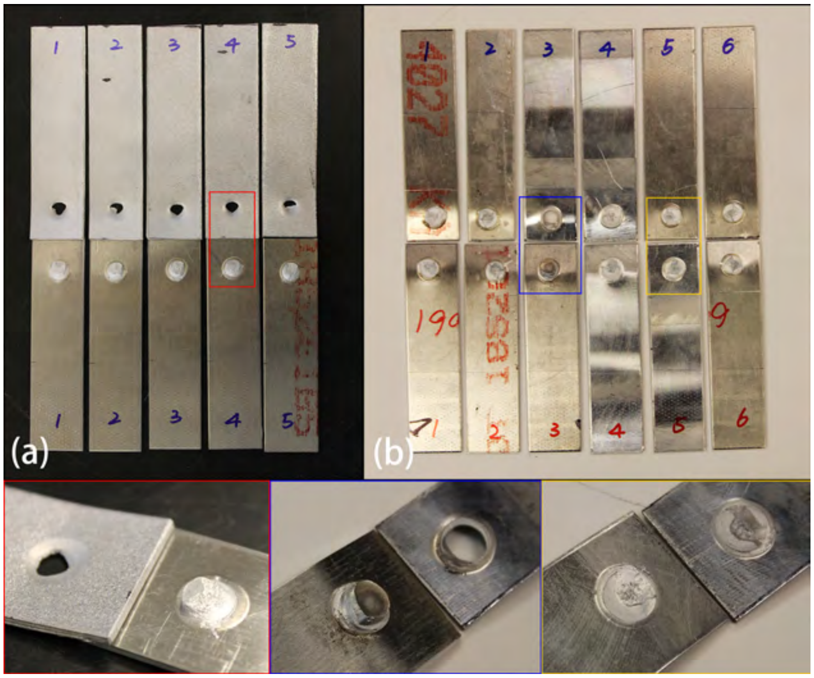

Figure 3.2: Tensile samples after testing with close-up images of representative failed joints: (a) UAM-bulk samples; (b) bulk-bulk samples

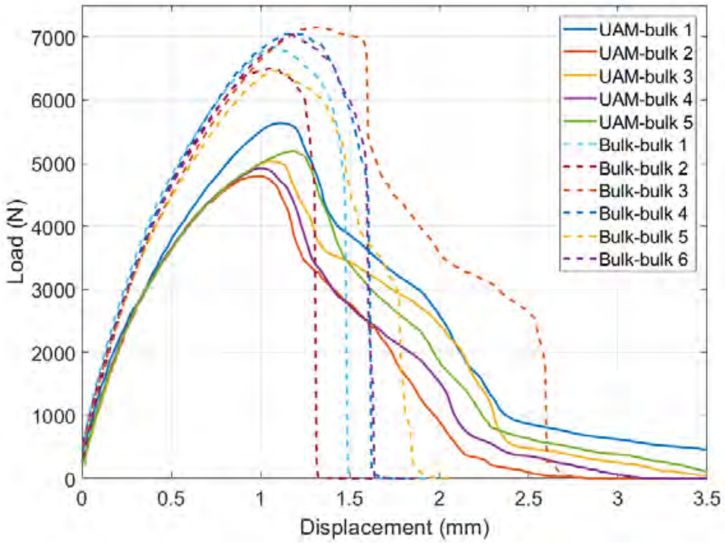

Figure 3.3: Load vs crosshead displacement plot of tensile tests on 2nd round RSW samples.

Table 3.3: Tensile test results of RSW samples of UAM AA 6061-H18 and bulk AA 6061-T6

	UAM - bulk		Bulk - bulk	
	Peak load (N)	d (mm)	Peak load (N)	d (mm)
Sample 1	5638	8.42	6843	9.54
Sample 2	4792	7.55	6501	9.29
Sample 3	5037	7.99	7154	9.50
Sample 4	4918	7.61	7069	9.61
Sample 5	5191	8.03	6461	8.80
Sample 6	N/A	N/A	7033	9.52
Average	5115.20	7.92	6843.50	9.38
Standard deviation	327.31	0.35	298.93	0.30

3.1.2 Cross-tension testing

Figure 3.4 and Figure 3.5 picture the cross-tensile samples before and after testing. One of the UAM-bulk samples is saved for optical imaging. All the samples, including UAM-bulk and bulk-bulk, failed by plug fracture. For the UAM samples, all the plugs are pulled from the UAM side. The data plotted in Figure 3.6 exhibits a high variability in both peak loads and curve shapes. Peak loads and nugget dimensions are listed in Table 3.4. The average peak load of bulk-bulk samples (3807.4 N) is much higher than UAM-bulk samples (1714.7 N), which is also presumable due to the strength difference of bulk and UAM material. The correlation between peak load and nugget dimension can also be observed from the summary of results in Table 3.4. All the samples failed by plug fracture, which is evidence of high-strength RSW in AA. Therefore, this set of RSW parameters can generate RSW with satisfactory strength and be applied to subsequent RSW studies in AA.

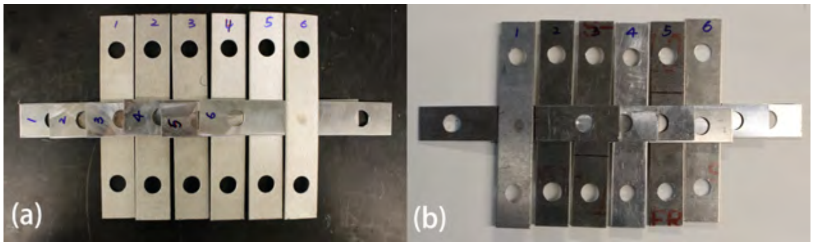

Figure 3.4: Cross-tensile samples before testing: (a) UAM-bulk samples; (b) bulk-bulk samples

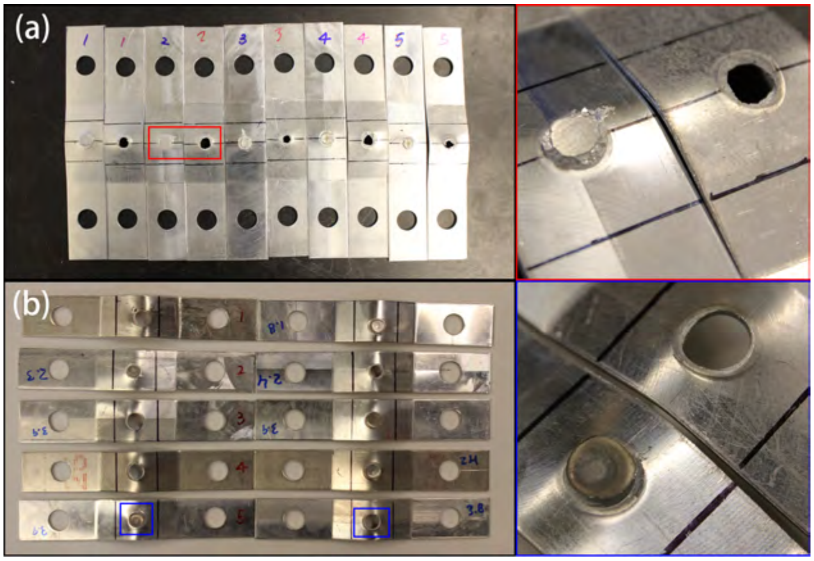

Figure 3.5: Cross-tensile samples after testing with close-up images of representative failed joints: (a) UAM-bulk samples; (b) bulk-bulk samples

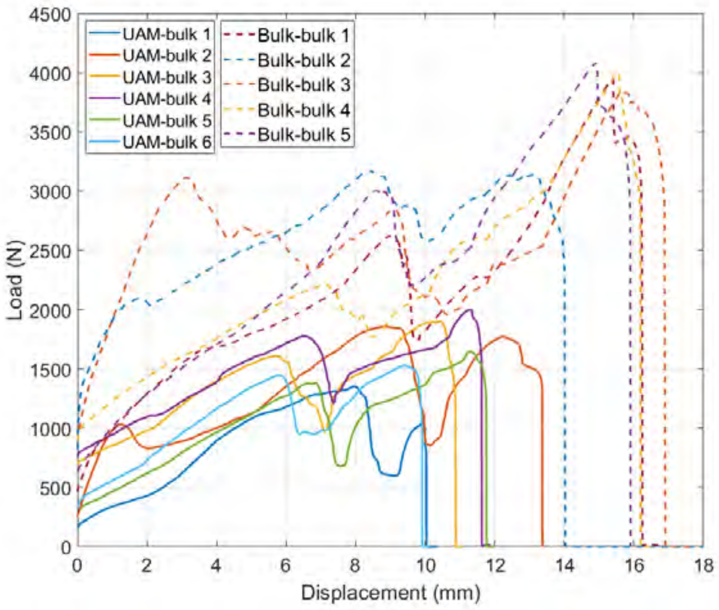

Figure 3.6: Load vs crosshead displacement plot of cross-tensile tests on RSW samples.

Table 3.4: Cross-tensile test results of RSW samples

	UAM - bulk		Bulk - bulk	
	Peak load (N)	d (mm)	Peak load (N)	d (mm)
Sample 1	1353	8.55	3951	8.84
Sample 2	1856	8.47	3170	7.58
Sample 3	1901	5.66	3835	9.69
Sample 4	1999	7.44	4002	9.08
Sample 5	1652	6.24	4079	9.26
Sample 6	1527	6.36	N/A	N/A
Average	1717.67	7.12	3807.40	8.89
Standard deviation	247.18	1.22	367.18	0.80

3.2 Investigate the heat affected zone from RSW

3.2.1 Literature review

A schematic of a steel-steel RSW cross-section is shown in Figure 3.7. Though the figure is welded steel and not aluminum, it shows the distribution of different regions, including fusion zone and heat affected zone, which applies to our case. Figure 3.8 shows the temperature distribution calculated from FEA. From the temperature ratio vs. non-dimensional radius plot, the temperature at the workpiece interface is much higher than at the electrode interface, but the heat only affects the region within the contact area. As for the electrode interface, the temperature within the contact area is low. However, there is a temperature peak when the radius is 1.2 times the radius of the contact area. The FEA result of weld nugget geometry and isothermal distribution is also shown in Figure 3.8.

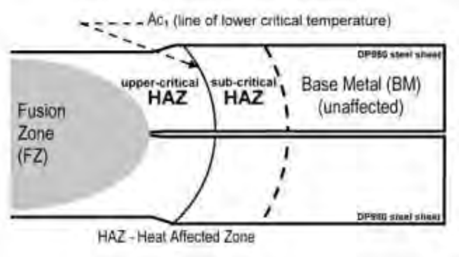
Ac_1 (line of lower critical temperature)
DP980 steel sheet
upper-critical HAZ
sub-critical HAZ
Base Metal (BM) (unaffected)
Fusion Zone (FZ)
DP980 steel sheet
HAZ - Heat Affected Zone

Figure 3.7: Schematic cross-section of a resistance spot weld [20].

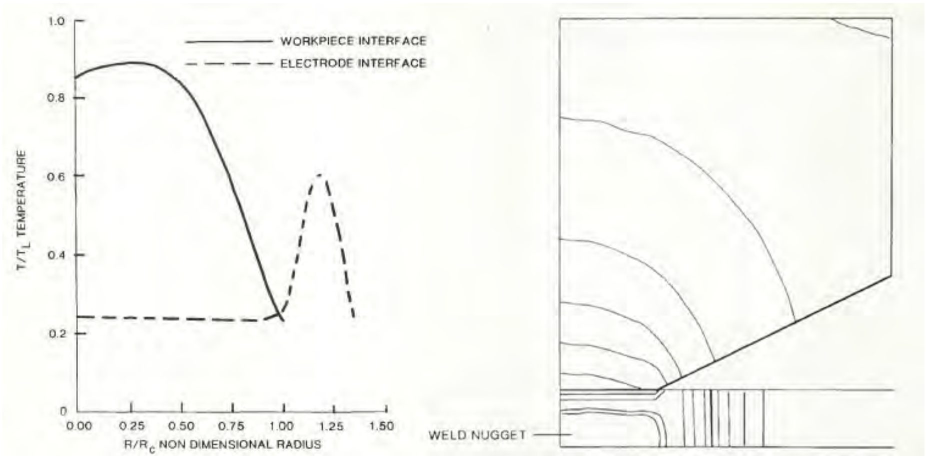

(a) (b)

Figure 3.8: (a) Temperature ratio vs. non-dimensional radius; (b) weld nugget geometry and isothermal distribution [35].

Experimentally, the HAZ of resistance spot welding is often identified by optical cross-section imaging. Microhardness indentations can be used to seperate non-affected base materials from heat affected materials due to the gradient of the softened HAZ zone. An image of a typical cross-section with indentations in shown in Figure 3.9. Two sets of microhardness indentations were located at the HAZ and the base material.

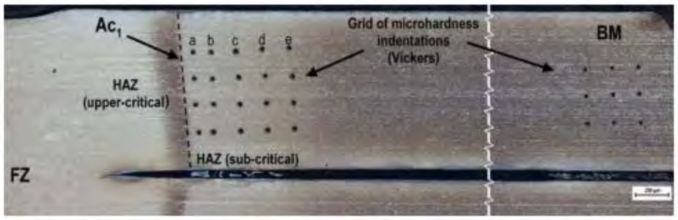
Ac$_1$
a b c d e
Grid of microhardness indentations (Vickers)
BM
HAZ (upper-critical)
HAZ (sub-critical)
FZ

Figure 3.9: Cross-section micrograph of resistance spot welded dual-phase steel with two sets of microhardness indentations [20].

3.2.2 Hardness testing

A UAM-bulk RSW sample was cross-sectioned and polished for hardness testing. A preliminary hardness test was performed on a machine with manual Vickers indentation by a 200 N force. To find the HAZ, some indents were made along with the interface of two AA pieces as shown in Figure 3.10. The hardness distribution obtained from the indents was plotted for UAM and bulk aluminum in Figure 3.11. The hardness of unwelded bulk 6061-T6 is about 110 HV from the tests, which agrees with the ASM material datasheet. The UAM 6061-H18 without RSW is softer with a hardness value of around 60 HV. In the HAZ, the two kinds of 6061 aluminum were melted and mixed, resulting in hardness values around 67 HV. From this plot, an approximated HAZ can be found between two locations where the hardness changed rapidly, as marked by two dash lines in Figure 3.11. Therefore, the area affected by the heat is from offset -17 mm to -6 mm, which means the diameter of HAZ is 11 mm. This value is used for investigation in the effect of distance between RSW and CF on UAM CFRP-AA transition structures in Section 3.3.

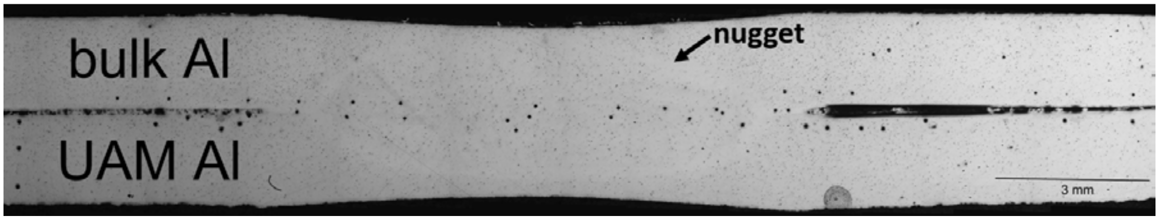

Figure 3.10: Optical image of the cross-section of a UAM-bulk RSW sample with indents for hardness testing.

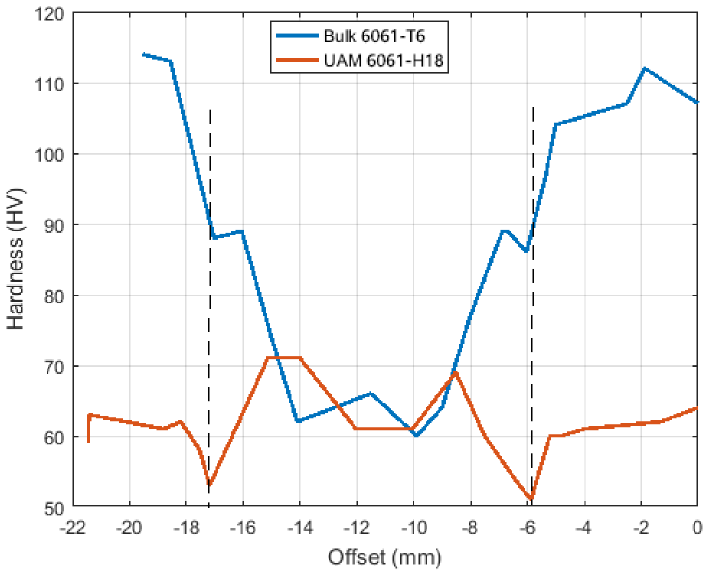

Figure 3.11: Hardness distribution along two lines close to the interface.

After the initial line scanning, a hardness mapping test was performed to get a comprehensive understanding of the HAZ. To obtain the hardness map, a load of 100 gram-force is used with an indentation spacing of 200 μm. Figure 3.12 shows the resultant hardness map from the sample. Comparing the area not affected by the RSW, the bulk 6061-T6 has a hardness of approximately 110 HV, which is higher than the 60 HV hardness of UAM AA. The middle region is the HAZ, where both bulk and UAM AA are softened. In the ellipse nugget region, signs of material mixing are observed. The HAZ is 12 mm from this map, which is slightly larger than the initial HAZ sizing from line scanning.

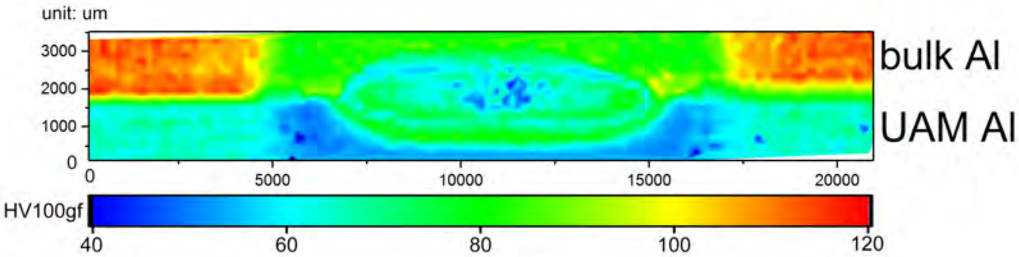

Figure 3.12: Hardness map of a UAM AA/bulk AA RSW.

3.3 Experimentally investigate the safe location of RSW on CFRP-AA joints

Twenty-five UAM transition coupons were prepared to be 25.4 mm wide with a 50 mm long AA tab, pictured in Figure 3.13. The AA matrix consists of 1 layer of two side-by-side tapes and 11 layers of sheet welded foils. An RSW is made on each sample to a bulk 6061-T6 AA tab. The samples are divided into five groups. For each group, there is 1 sample from each UAM welded flange. The locations of the center of RSW spots (RSW offset defined in Figure 3.14 (a))are planned to be R, 2R, 3R, 4R, and 5R (with the radius, R=5.5 mm, based on the hardness line scanning HAZ measurement from Section 3.2) from the CFRP-AA joint edge. These 5 RSW location cases are randomly assigned to 5 sample groups. However, only 1 of the 5 samples was successfully welded to the bulk AA tab at the location of R from the joint edge. All welds at further distances from the CFRP-AA interface were successful. From the 21 successfully spot welded samples, one sample from each R, 2R, and 3R group was cross-sectioned for optical imaging (all from flange E). Therefore, 18 samples with RSW locations of 2R, 3R, 4R, and 5R were prepared for tensile tests as shown in

Figure 3.14. After the RSW was performed, the extra bulk AA tabs were cut off. An AA spacer was attached to each tensile sample using epoxy.

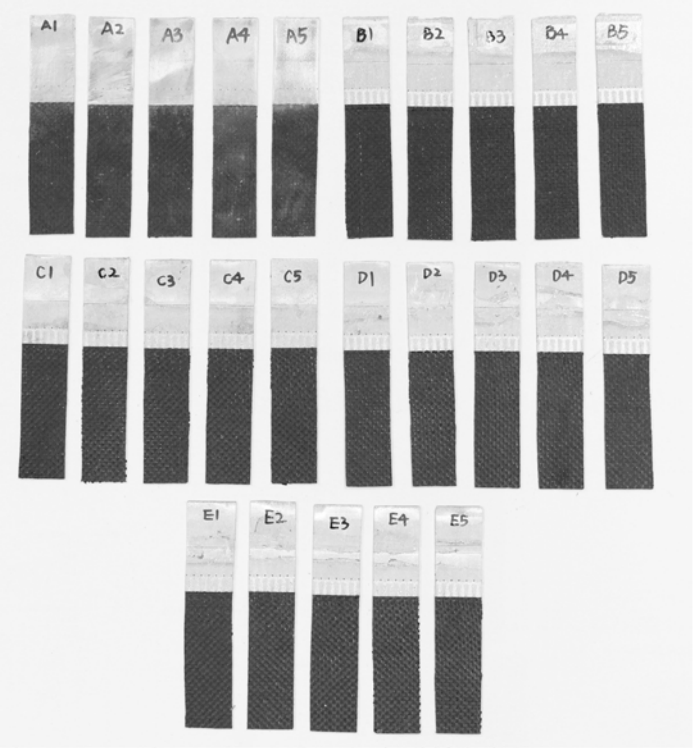
A1
A2
A3
A4
A5
B1
B2
B3
B4
B5
C1
C2
C3
C4
C5
D1
D2
D3
D4
D5
E1
E2
E3
E4
E5

Figure 3.13: UAM transition coupons for RSW.

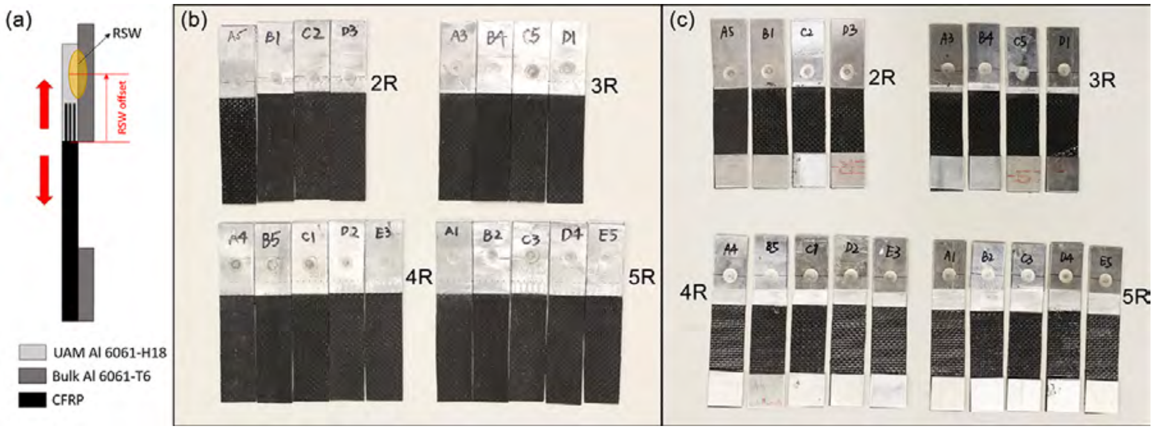
(a)
RSW
RSW offset
UAM Al 6061-H18
Bulk Al 6061-T6
CFRP
(b)
A5
B1
C2
D3
2R
A3
B4
C5
D1
3R
A4
B5
C1
D2
E3
4R
A1
B2
C3
D4
E5
5R
(c)
A5
B1
C2
D3
2R
A3
B4
C5
D1
3R
A4
B5
C1
D2
E3
4R
A1
B2
C3
D4
E5
5R

Figure 3.14: UAM transition coupons welded to bulk AA tab by RSW and prepared for tensile tests: (a) schematic of the samples; (b) front; (c) back.

3.3.1 Tensile tests

The samples were tested in tension at 1.27 mm/min to investigate the relationship between tensile strength and RSW location. As shown in Figure 3.15, all the samples failed by CF breaking. There is no apparent damage observed on the CF tows except for the samples of the 2R group. The CF tows of these four samples were damaged by the RSW spot at the center.

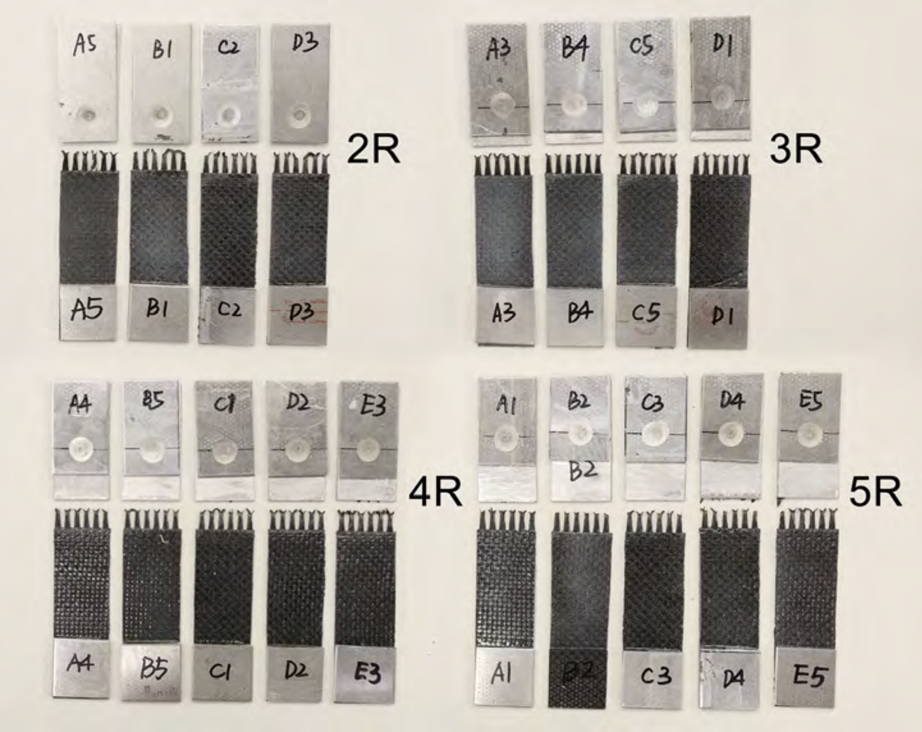
A5
B1
C2
D3
2R
A3
B4
C5
D1
3R
A5
B1
C2
D3
A3
B4
C5
D1
A4
B5
C1
D2
E3
4R
A1
B2
C3
D4
E5
B2
5R
A4
B5
C1
D2
E3
A1
B2
C3
D4
E5

Figure 3.15: UAM transition coupons welded to bulk AA tabs by RSW after tensile tests.

Figure 3.16 shows the scatter diagram of the samples. The grey vertical dashed line indicates the location where CF tows end. The scarlet horizontal dashed line shows the industry specification of the joint strength. For each of the samples, the dot is the center of the RSW and the horizontal error bar indicates the area of the RSW nugget. Note that flange D is defective because the epoxy did not fully cure. Consequently, the peak loads for all samples from flange D are not representative of a properly cured joint. From the samples with an RSW offset of around 0.45 inch (2R), 3 of the 4 peak tensile loads are below the spec. Therefore, making an RSW at 2R offset damages the joint strength. When the RSW is made at roughly 0.65 inch (3R), the strength significantly increased from 2R within each flange. The peak load of samples with an RSW at 4R increased from 3R for flange A and C, but almost keep the same as 3R for flange B. When the RSW moves to 1.05 inch (5R), the peak loads decrease for a large amount for flange A and C. Looking into the DIC strain map in Figure 3.17, the load is severely non-uniformly distributed for these samples, which may result from non-uniform gripping due to thickness differences caused by the RSW process. For these samples, the RSW was performed on top of the UAM seam between two weld passes, causing the AA tab of the CFRP-AA joint to bend during the RSW process. The sample with RSW at 5R from flange B does not have this issue because the RSW failed by cracking along the UAM seam at the first testing attempt. Therefore, the AA tab welded by RSW was removed when the actual tensile test for the CFRP-AA joint was performed.

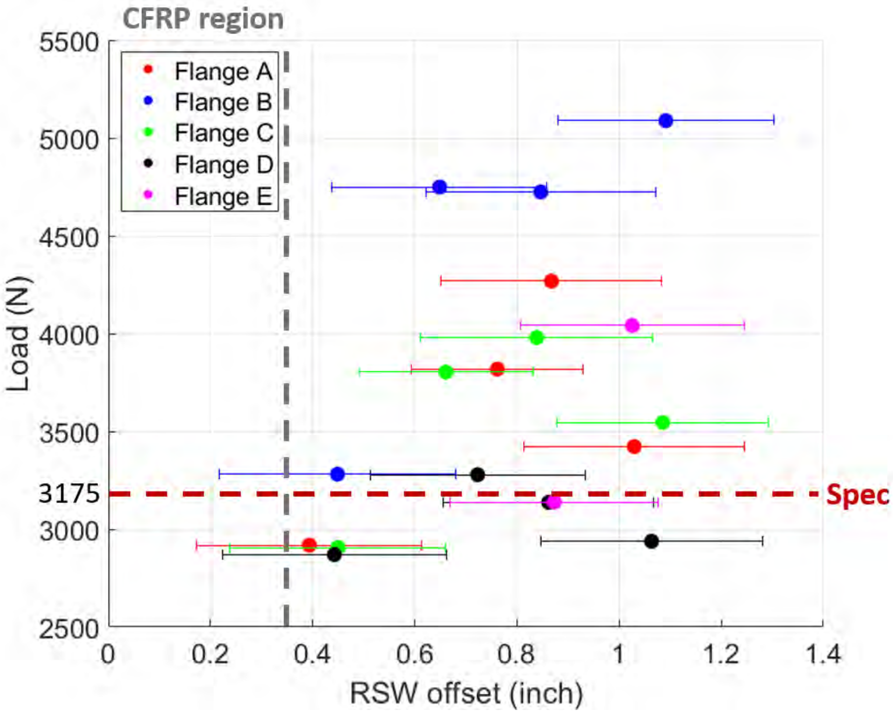

Figure 3.16: Scatter diagram of peak tensile load vs RSW location.

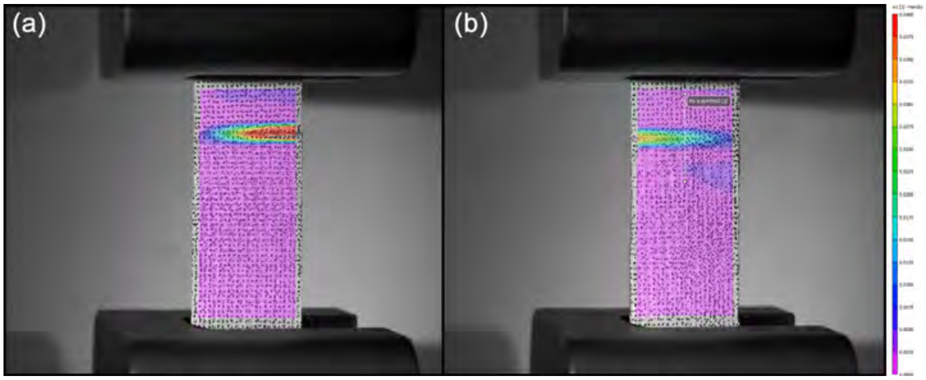

Figure 3.17: DIC strain map indicates nonuniform loading of samples with RSW at 5R: (a) sample from flange A; (b) samples from flange C.

3.3.2 Optical images

Figure 3.18 includes three images of samples from flange E with RSWs at 1R, 2R, and 3R. Firstly, the CF tows of the sample with an RSW at 1R are seriously damaged at the spot region in the center of Figure 3.18 (a). When the RSW moves further to 2R, the CF tows are still damaged, and the vent hole is melted. From Figure 3.18 (c), the CF tows and the vent hole are intact, with the RSW located at 3R from the CF-AA joint edge. This agrees with the analysis from the peak tensile load scatter diagram that an RSW at 3R will not severely harm the joint strength. Note there are some voids in the images for all three cases. This may have occurred during the RSW due to the extra epoxy at the surface of the CFRP-AA coupon, which was not completely removed before RSW.

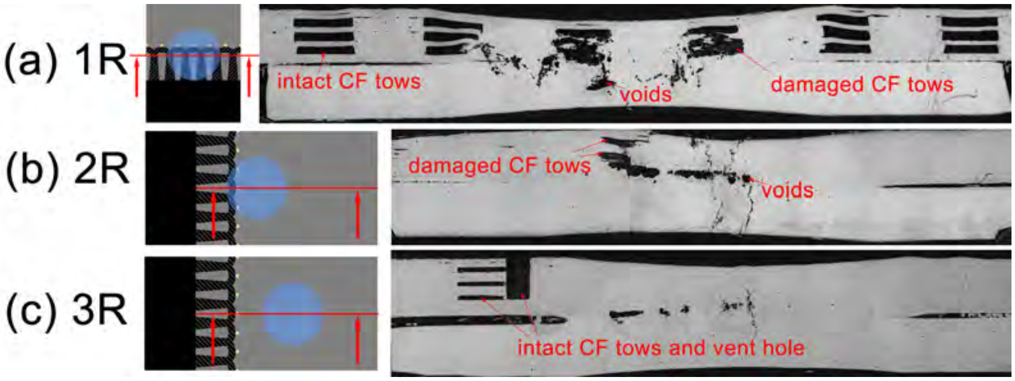

Figure 3.18: Images of CFRP-AA coupons after RSW at different locations. Red lines and arrows in the schematic to the left of the image indicates the corresponding imaging location.

3.4 Summary

RSWs were performed between UAM 6061 and bulk 6061 to create tensile and cross-tensile samples to characterize the weld strength. Comparing the results of UAM-bulk and bulk-bulk samples, RSWs performed on bulk-bulk samples are stronger than RSWs performed on UAM-bulk samples. This may result from the different material strength between bulk 6061-T6 and UAM 6061-H18. The spec value UTS of 6061-T6 is 310 MPa. The experimental UTS of UAM 6061-H18 is 195 MPa. The tensile and cross-tension peak loads of UAM-bulk samples are 5115.2 N and 1714.7 N, respectively. Since the strength of UAM-bulk is satisfactory, the same RSW parameters were used for all subsequent RSW-related studies on AA.

A hardness study was performed on one UAM-bulk RSW to find the HAZ size. The HAZ diameter is obtained to be 11 mm from a hardness line scanning at the cross-section of the RSW. Also, a microhardness mapping was performed, and the HAZ diameter is identified as 12 mm. However, this mapping was performed after the mechanical testing. Therefore, the HAZ radius (R) is being assigned as 5.5 mm (from the line scanning result) in the following paragraph.

Twenty-five CFRP-AA UAM joint coupons were constructed for this task. Twenty-one of the coupons were successfully welded to AA tabs with RSW at specific locations. From tensile tests on the samples, the peak tensile load significantly decreased when an RSW was performed 2R (11 mm) from the AA/CFRP interface. When the RSW is performed at least 3R from the interface, the peak tensile load is at a normal level, which means the RSW does not harm the joint strength. The CF tows are seriously damaged by the heat from RSW when performed at 1R or 2R from the AA/CFRP interface, which is also confirmed by optical micro-images. When the RSW is performed at 3R (16.5 mm), the CF tows are intact. In conclusion, for a 1.75 mm thick AA/CFRP UAM joint to be joined with RSW to a 1.75 mm thick AA 6061-T6 tab, the RSW location should be at least 16.5 mm from the AA/CFRP interface to prevent any decrease in the UAM CFRP-AA joint strength.

Chapter 4: CFRP-AA Beams Joined by UAM and RSW

4.1 Literature survey

To investigate the role of CFRP-metal joints in a vehicle structure, it is necessary to evaluate the performance of the joints via structure-level tests. In a car frame, top-hat and double-hat thin-walled beams are widely used due to their high performance in both specific strength and energy absorption (EA). Bending and axial crushing are the two most common tests that are performed to evaluate the performance of the beams. Sato et al. [38] investigated the relationship between sheet thickness and bending crash performance of hat-shaped structures. Dynamic and quasi-static bending tests are performed on top-hat structures made from various types of high-strength steels with different wall thicknesses. White et al. [49, 50] performed both dynamic and quasi-static axial crush tests on top-hat and double-hat structures made by spot-welded mild-steel hat sections.

Efforts to evaluate the performance of CFRP in hat-shaped beams have been made by Liu et al. [29, 28] via axial crush and bending tests of CFRP double-hat beams. The results show that the energy absorption of CFRP beams is twice that of conventional metallic tubes. Additionally, the study proved that the double-hat beam shape exhibits benefits in energy absorption compared with most alternative beam shapes. However, manufacturing CFRP tubes with top-hat or double-hat configurations is challenging because the widely used metal joining methods are not applicable to CFRP. Typical transition joining methods such as adhesives and rivets exhibit issues in fatigue life, stress concentration, damage initiation, or corrosion [7, 30].

In this study, AA flanges are created on the edges of CFRP hat sections using the joining method developed by this research project. The AA flanges enable resistance spot welding (RSW) to an AA plate or another CFRP hat with AA flanges to build top-hat or double-hat structures, respectively. Similar CFRP structures without metal flanges are joined using pop rivets for benchmarking against the UAM/RSW joints. Four-point bend tests are performed on top-hat structures. Dynamic axial crush and quasi-static torsion tests are performed on double-hat structures. The crush force efficiency is calculated in bend and axial crush tests, which is a dimensionless quantity that characterizes the sample's performance to maintain a high load-carrying ability after the initial cracking. This paper uses crush force efficiency and EA as primary metrics to evaluate the mechanical performance of the CFRP hat-shaped beams.

4.2 Sample preparation

4.2.1 CFRP-AA hybrid structures

In order to produce structures for testing, CFRP hat sections with integral AA flanges are fabricated using UAM CF-AA joints [11]. The CF fabrics being used to construct transition joints are 3K CF tape supplied by Fibre Glast Developments Corp. The CF tape has a bidirectional plain weave with looped weft tows for clean-finished edges. Five warp CF tows are removed from the edge to expose these loops.

During the UAM process, an AA 6061-T6 baseplate is bolted to a vacuumed adapter plate, as shown in Figure 4.1 (a). The 0.152 mm thick AA 6061-H18 foil feedstock is welded onto the baseplate using parameters listed in Table 4.1. The in-plane ultimate tensile strength of the AA matrix built from this setup is 195 MPa [39]. After four layers of 25.4 mm wide AA foil tape are welded layer-by-layer on the baseplate, forming a 0.608 mm thick base matrix, channels to house the CF tow loops are machined as shown in Figure 4.1 (b). The channel dimensions are designed to match the dimensions of 3K CF tow loops as described above. A layer of CF loops are placed in the channels as shown in Figure 4.1 (c). To encapsulate the loops, a layer of 6061-H18 foil sheet is welded over them. In contrast to the automatically fed foil tape, the sheet is held to the substrate with vacuum [11]. After the sheet layer is welded to consolidate the CF tows, more 6061-H18 foil tape layers are welded to create an AA matrix for embedding the subsequent CF layers. Figure 4.1 (d) shows a sample with one layer of CF embedded. Following (b), (c), and (d), more CF layers are embedded in the sample. For the transition joints investigated in this paper, there are 3 CF layers embedded as the side view illustrates in Figure 4.2. Figure 4.1 (e) shows the front and back of two transition flanges that are removed from the baseplate and ready for layup.

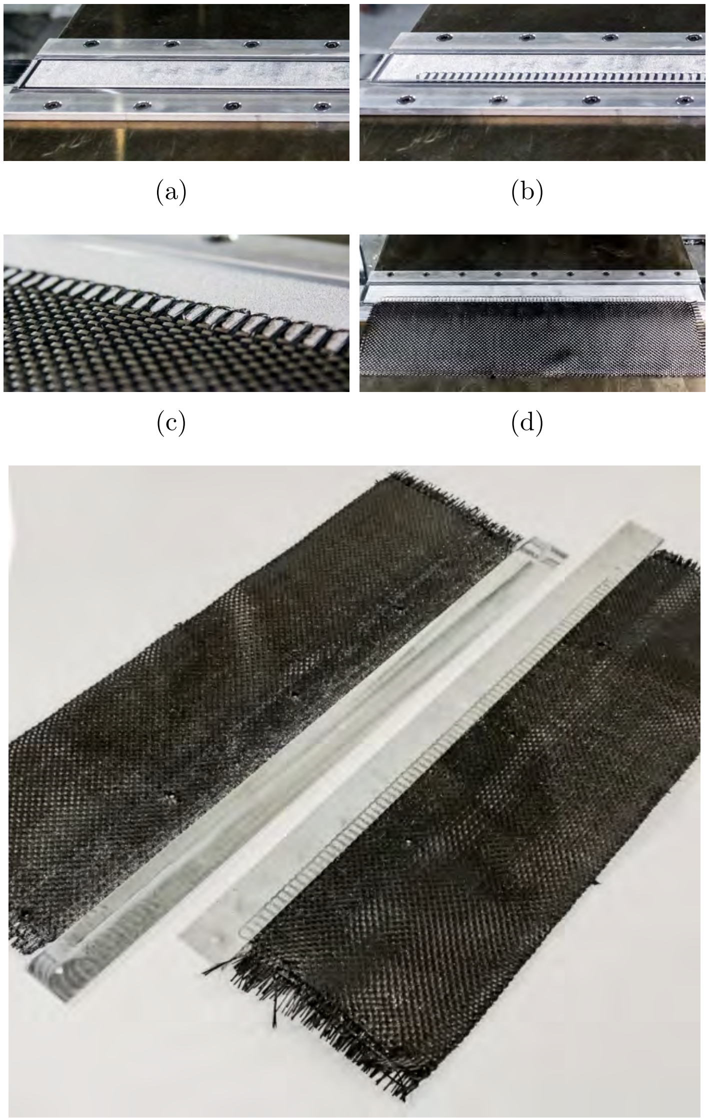

(a) (b)

(c) (d)

(e)

Figure 4.1: Procedures to construct CF-AA transition joints.

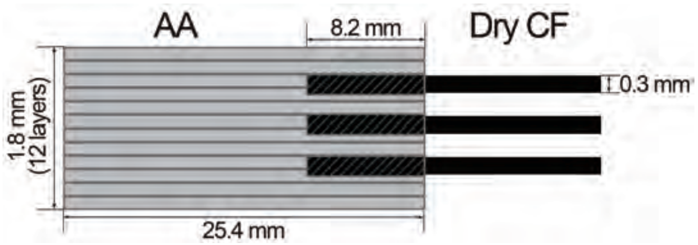

Figure 4.2: Side view of a 3-CF-layer transition joint (schematic not drawn to scale).

Table 4.1: Welding parameters for AA 6061-H18 foils

	Force (N)	Amplitude (μm)	Speed (cm/s)	Dwell time (ms)
Tape	4000 N	32 μm	84.7 mm/s	300 ms
Sheet	4000 N	30 μm	33.9 mm/s	150 ms

After the AA flanges are constructed using UAM, two flanges are mounted in a mold, as shown in Figure 4.3, and prepared for layup and curing. The dry CF fabrics on the flanges are laid up with four extra plain weave CF pre-preg layers at 0° or 90° directions, supplied by Axiom Materials, Inc. Additional CF pre-preg layers are interleaved with the dry CF fabrics to connect the two flanges, as well as match the thicknesses of the CFRP the AA flanges. As explained by Figure 4.4, the seams between CF fabrics are designed to be staggered in order to prevent weak points in the CFRP structure. The hat section is then cured using epoxy resin films in an autoclave under 0.4 MPa pressure at 121°C. Figure 4.5 shows the dimensions of a complete hat section.

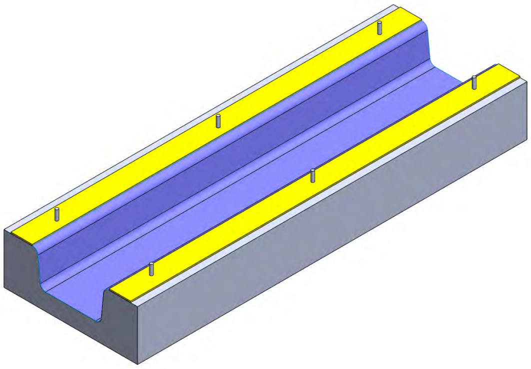

Figure 4.3: Mold for CFRP laying up of the hybrid hat structure.

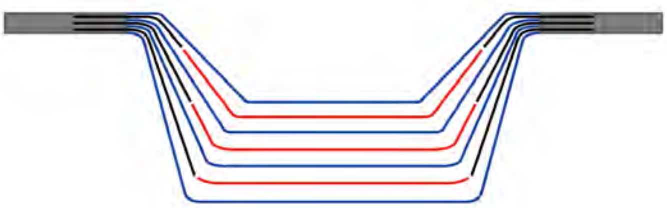

Figure 4.4: Layup configuration for a CFRP hat with AA flanges. Black layers are dry CF fabrics joined with the AA flanges. Red and blue layers are additional CF pre-preg fabrics. Layup is not shown to scale.

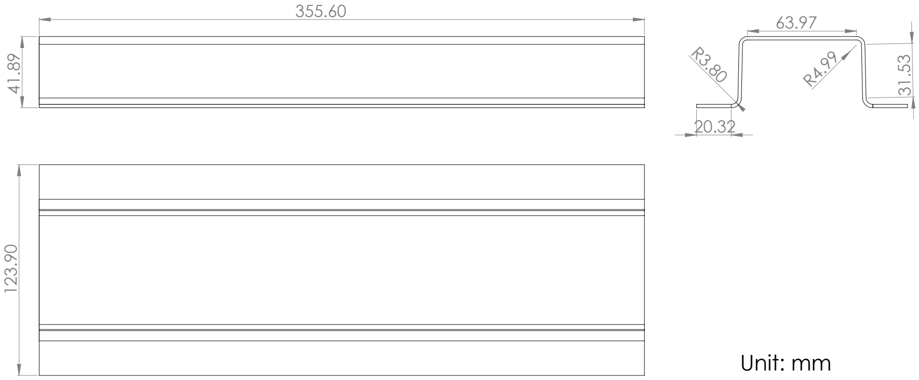

Figure 4.5: Dimensions of a hybrid hat structure.

For four-point-bend tests, the CFRP-AA hybrid hat sections are welded to 1.0 mm thick TM30 AA plates by RSW through the AA flanges to construct top-hat structures. For axial crush tests and torsion tests, double-hat structures are constructed by joining two hybrid hat sections using RSW. For both structures, the RSW spacing is 40 mm, and the welding parameters are listed in Table 4.2. Figure 4.6 and Figure 4.7 show the RSW process to build the top-hat and double-hat structures, respectively. The completed structures are shown in Figure 4.8.

Table 4.2: RSW parameters

Cycles	5 cycles at 60 Hz
Current	27 kA
Force	550 kgf
Tip	16 mm DR 50

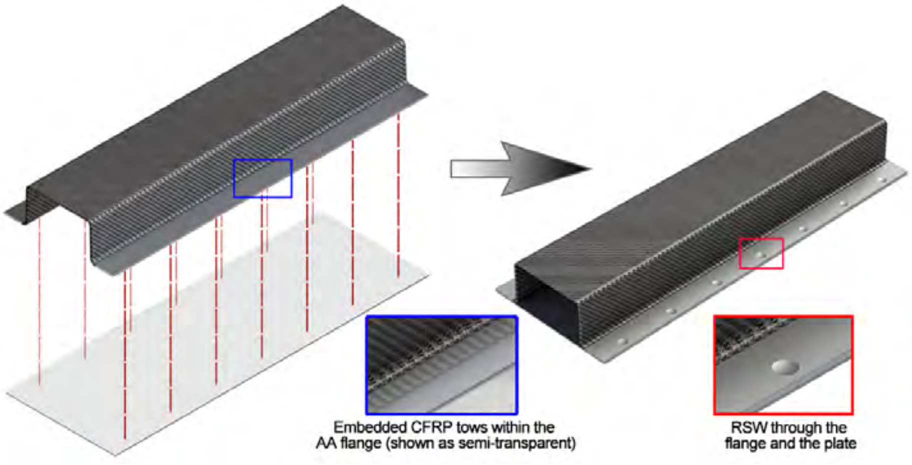
Embedded CFRP tows within the AA flange (shown as semi-transparent)
RSW through the flange and the plate

Figure 4.6: Using RSWs to join a UAM hat with an AA plate to construct a top-hat section.

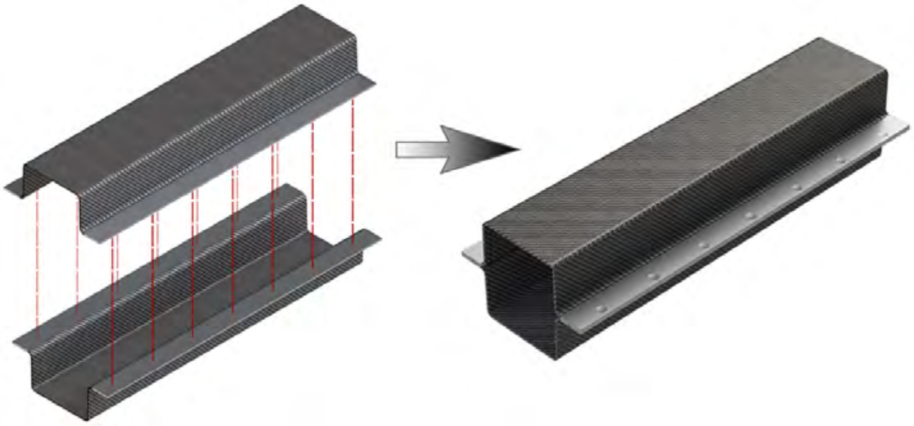

Figure 4.7: Using RSWs to join two UAM hats to construct a double-hat section.

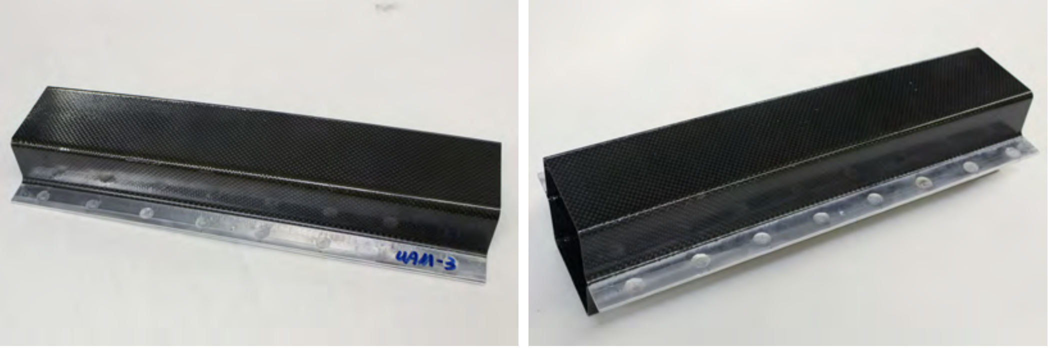

(a) (b)

Figure 4.8: (a) A UAM top-hat structure; (b) a UAM double-hat structure.

4.2.2 Riveted structures

For benchmarking, CFRP hat sections without AA flanges are manufactured. They are laid up with seven layers of plain weave CF pre-preg in 0/90° to match the thickness of the CFRP-AA hybrid hats. Unlike the AA flanges on the hybrid hat sections, the CFRP flanges are unable to be metallically joined. Hence, the samples are constructed using pop rivets from Industrial Rivet & Fastener Co. The CFRP-AA top-hat structures are manufactured by joining a CFRP hat with an AA plate, and CFRP-only double-hat consists of two CFRP hats joined by rivets. The nominal tensile and shear strengths of the rivets are 2224 N and 1690 N, respectively, based on the datasheet. Figure 4.9 shows the riveted top-hat structures and double-hat structures.

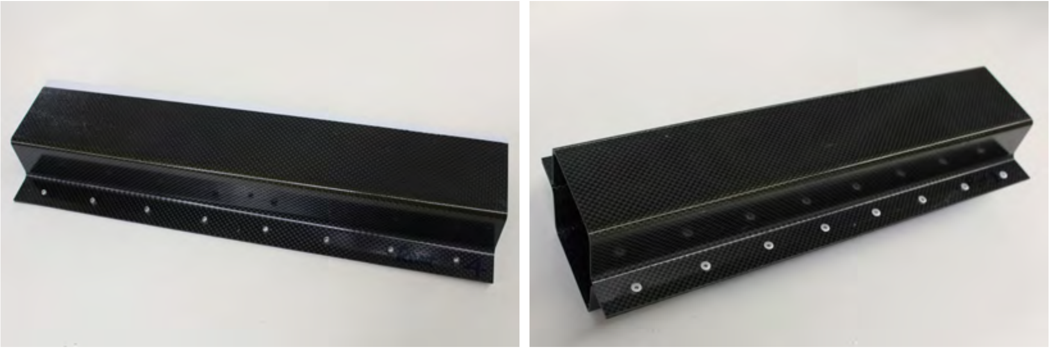

(a) (b)

Figure 4.9: (a) A riveted top-hat structure; (b) a riveted double-hat structure.

4.2.3 Notation of sample configuration and load cases

For clarification, this paper will refer the samples using notations formatted as "type-load case-number". The "type" is either "UAM" or "rivet", and the "number" refers to the number of the specific sample. The configurations of the samples are summarized in Table 4.3.

Table 4.3: Summary of sample configurations. CFRP: CFRP hat, AA: AA plate.

Notation	Load case	UAM			Rivet		
		Top	Bottom	Joint	Top	Bottom	Joint
b	Quasi-static four-point bend	CFRP	AA	UAM +RSW	CFRP	AA	Pop rivets
c	Dynamic axial crush		CFRP			CFRP	
t	Quasi-static torsion						

4.3 Four-point-bend tests

4.3.1 Experimental method

Three UAM and four riveted top-hat structures are tested in four-point-bend using an MTS C43-504 load frame at a rate of 3.87 mm/min with a 30 mm support span. From the load and displacement data recorded by the load frame, the energy absorption (EA) is calculated by integrating the load over the displacement,

$$EA = \int_0^d F(x)dx.$$

The average load ($F_{average}$) is calculated by dividing the energy absorption by the displacement at failure:

$$F_{average} = \frac{EA}{d}.$$

The crush force efficiency (ϵ) is defined as the ratio between average load and peak load,

$$\epsilon = \frac{F_{average}}{F_{max}}.$$

This ratio is generally used as the primary metric to evaluate crashworthiness under the four-point bend loading condition.

To investigate the strain distribution during tests using DIC, the samples are painted in white and then speckled with black spots on the outside of a sidewall. Two cameras capture the side of the sample at 4 Hz, and the strain map of the sidewall is created by the DIC system.

4.3.2 Results and discussion

Load vs. displacement curves for the samples are plotted in Figure 4.10. The UAM samples reach their first peak at 10 mm of displacement, which indicates initial cracking in the CFRP. After this point, the loads gradually decrease as the tests continue. Sample UAM-b-1 exhibits a reloading and reaches a second peak load before ultimate failure. All the UAM samples show the ability to continuously carry loads near 5000 N after the initial peaks until complete CFRP failure at displacements of 42 to 53 mm. In contrast, the riveted samples all exhibit rapid load decreases after the initial peaks, which correspond to rivets failing. They are unable to support a load above ~5500 N as soon as the first rivet fails. The load curves of riveted samples do not reach zero because the tests are stopped after each sample slips off one of the roller supports.

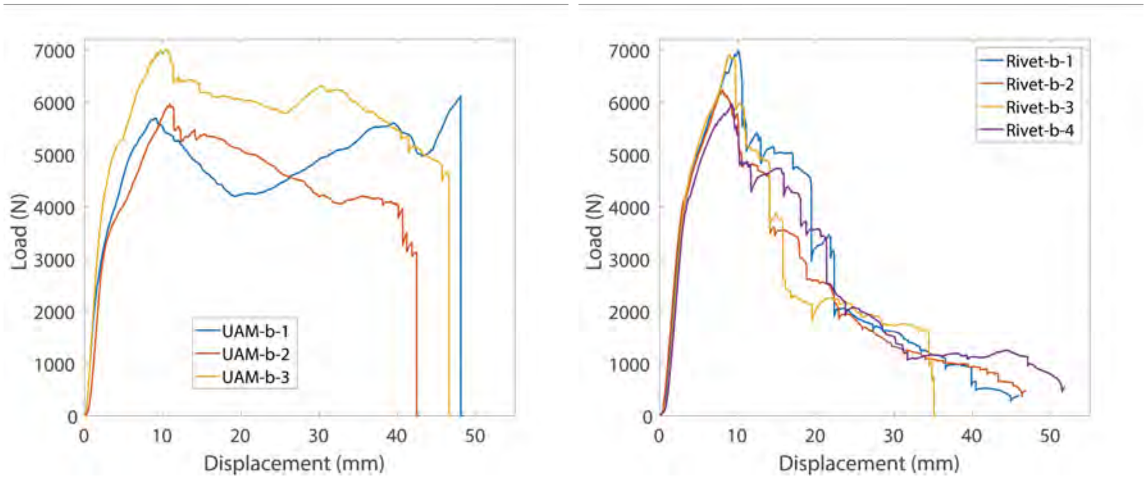

(a) (b)

Figure 4.10: Load vs. displacement curves for four-point bend tests on (a) UAM samples and (b) riveted samples.

Quantitative test results are listed in Table 4.4. The average peak load of riveted samples is 4% higher than that of the UAM samples, while the average energy absorption of the UAM samples is 86.3% larger. With significantly higher average loads, the UAM samples also have a 0.777 crush force efficiency, which is 83.7% higher than the rivet samples. Although the average peak load of the UAM samples is slightly lower than that of riveted samples, the UAM samples exhibit significant benefit in both energy absorption and crush force efficiency.

Table 4.4: Four point bend results for top-hat structures.

	Peak load (N)	Energy absorption (J)	Average load (N)	Crush force efficiency
Rivet-b-1	6983	131	2852	0.41
Rivet-b-2	6238	117	2501	0.41
Rivet-b-3	6904	110	3103	0.45
Rivet-b-4	5958	130	2501	0.42
Average	6520.8	122.0	2739.3	0.423
Standard deviation	502.4	10.2	293.6	0.019
UAM-b-1	6109	230	4784	0.78
UAM-b-2	5961	187	4413	0.74
UAM-b-3	7017	265	5685	0.81
Average	6262.3	227.3	4960.7	0.777
Standard deviation	571.8	39.1	654.1	0.035

Four representative strain maps of sample Rivet-b-1 during four-point bend testing are shown in Figure 4.11 (a). At the beginning of the test, the strain distribution agrees well with the theoretical loading condition for four-point-bending tests. As the upper loading pins continue pressing on the sample, two cracks initiate at these two loading points as shown in Figure 4.11 (b). As the bending progresses, the higher stiffness of the CFRP flanges makes them unable to bend along with the AA plate. Finally, the significant moduli mismatch between the AA plate and the CFRP flanges leads to a separation between them, which can no longer be prevented by the rivets, as pictured in Figure 4.11 (c). At this point, the central rivets that hold the AA plate and the CFRP flange together fails. Toward the end of the test, the CFRP hat has completely cracked and slipped from the left lower support. Pictures of failed samples are shown in Figure 4.12.

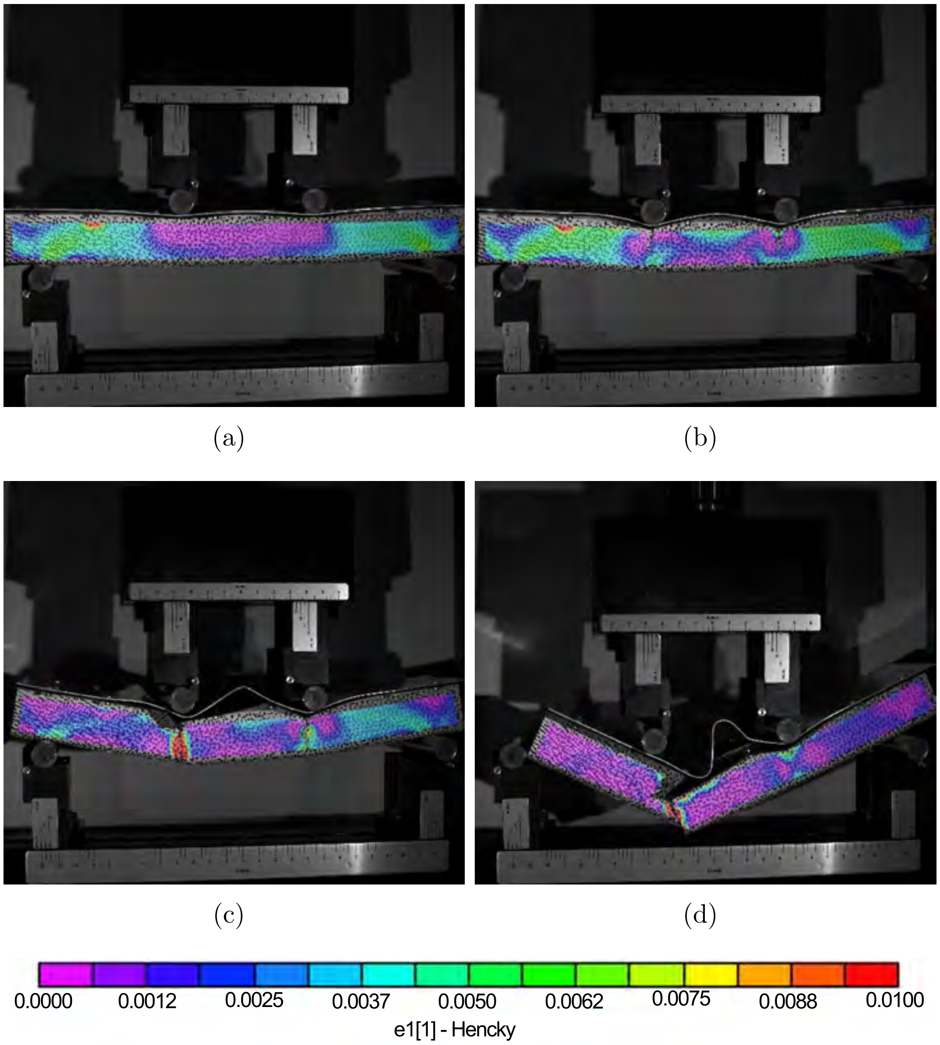
(a)

(b)

(c)

(d)

0.0000
0.0012
0.0025
0.0037
0.0050
0.0062
0.0075
0.0088
0.0100
e1[1] - Hencky

Figure 4.11: Strain maps of sample Rivet-b-1 during testing: (a) strain distribution at the beginning of the test; (b) cracks initiate under two upper loading noses; (c) cracks propagate, a rivet fails, and the AA plate separates from the CFRP; (d) test ends when the left side of the sample slips off the left support.

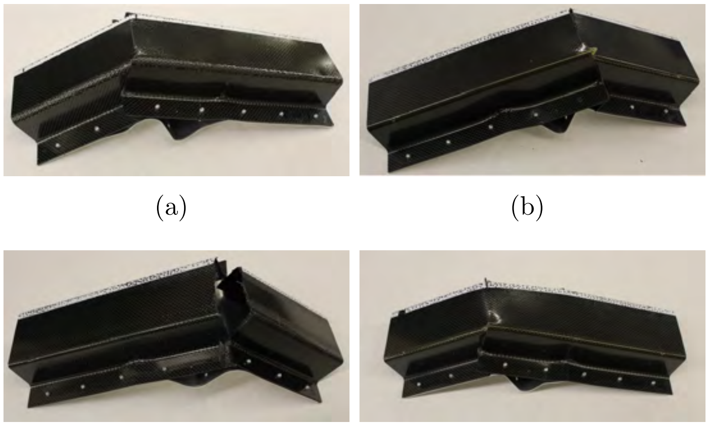

(a) (b)

(c) (d)

Figure 4.12: Riveted top-hat structures after four-point-bend tests: samples (a) Rivet-b-1; (b) Rivet-b-2; (c) Rivet-b-3; (d) Rivet-b-4.

For the UAM samples, four representative DIC strain maps for sample UAM-b-1 are shown in Figure 4.13. The strain distribution and crack initiation in the CFRP are similar to those of sample Rivet-b-1, as shown in Figure 4.13 (a) and (b), respectively. However, as the test continues, the AA flanges are able to deform with the AA plate as pictured in Figure 4.13 (c). The cracks in the CFRP continue to propagate, and the joints remain intact until the CFRP hat fails as shown in Figure 4.13 (d). Pictures of UAM samples after testing are shown in Figure 4.14.

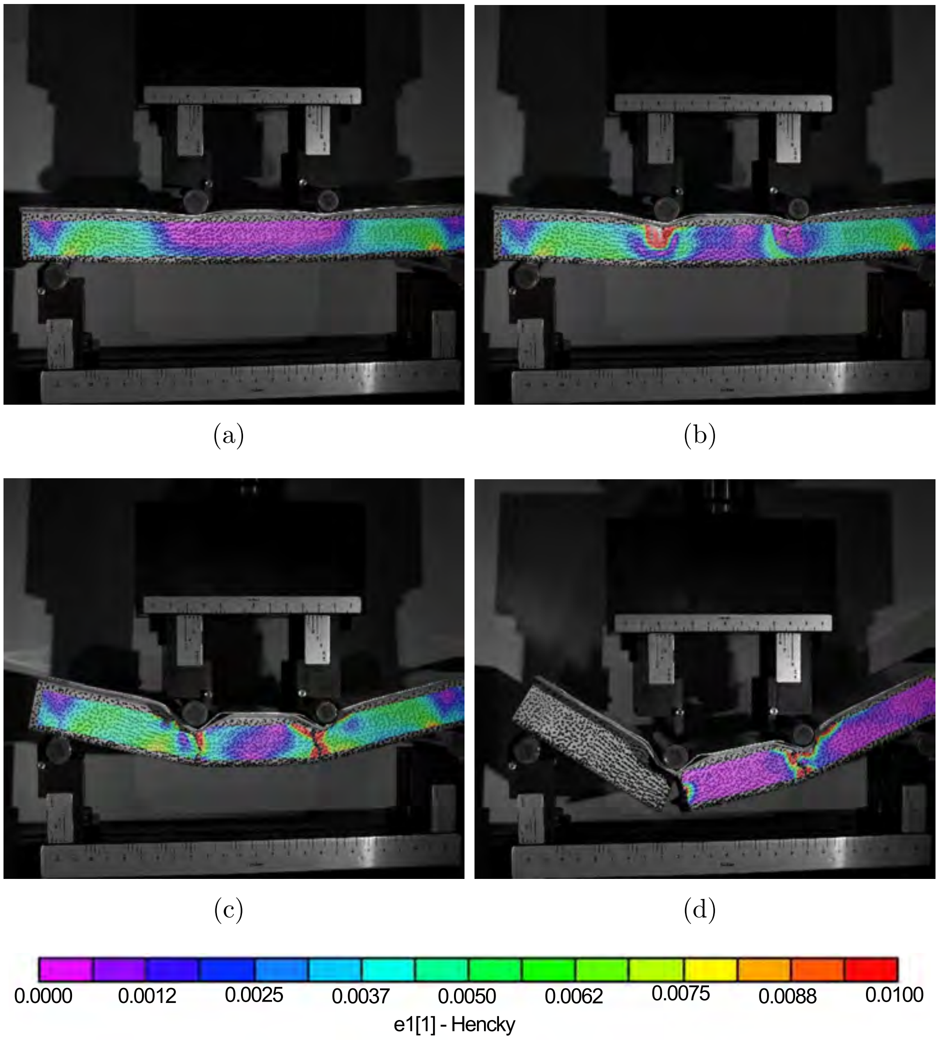
0.0000
0.0012
0.0025
0.0037
0.0050
0.0062
0.0075
0.0088
0.0100
e1[1] - Hencky

(a) (b) (c) (d)

Figure 4.13: Strain maps of sample UAM-b-1 during testing: (a) strain distribution before any cracks initiate; (b) cracks initiate under two upper loading noses; (c) cracks propagate and the flange deforms with the AA plate; (d) test ends when CFRP hat fails.

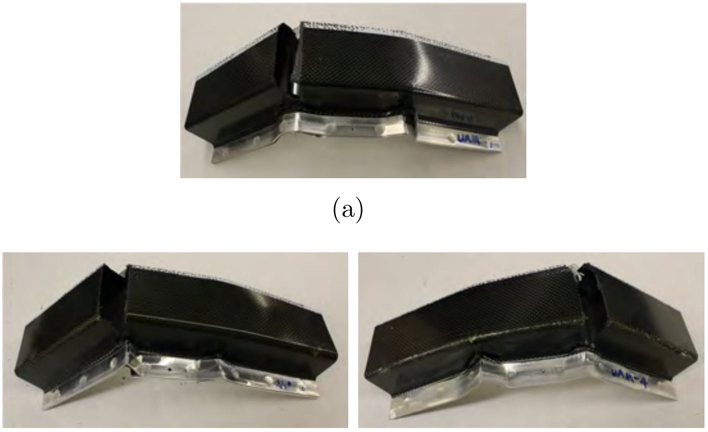
(a)

(b) (c)

Figure 4.14: UAM top-hat structures after four-point-bend tests: samples (a) UAM-b-1; (b) UAM-b-2; (c) UAM-b-3.

Close-up images of failed samples are shown in Figure 4.15. Figure 4.15 (a) includes a failed rivet, common to all the riveted samples. Figure 4.15 (b) shows a crack on the UAM flange. This is a typical failure observed in the UAM samples. The only sample with UAM delamination is UAM-b-1, which is shown in Figure 4.15 (c).

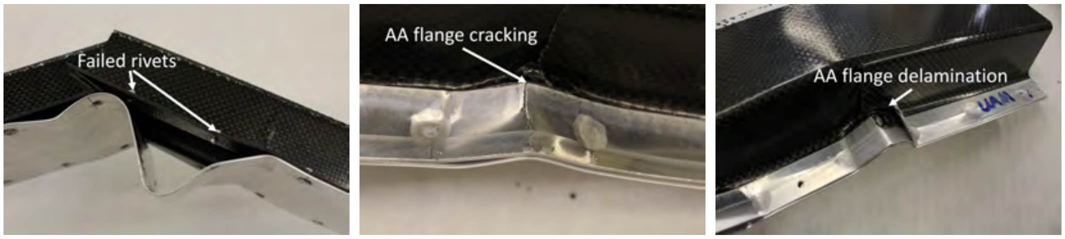

(a) (b) (c)

Figure 4.15: Detailed pictures of joint failures for hat-plate structures: (a) rivet failure; (b) UAM flange cracking; (c) UAM flange delamination.

4.3.3 Conclusion

The top-hat structures with UAM AA flanges have a significant benefit for crashworthiness with minimal decrease in the peak load while under the four-point bend testing condition. The UAM samples are able to support a substantial amount of load after the initial cracking in the CFRP occurs. The reason is explained from the DIC strain maps that the UAM AA flanges are able to undergo large deformations and, consequently, to avoid joint failure or structural collapse.

4.4 Axial crush tests

4.4.1 Experimental method

Axial crush tests are performed on four riveted and three UAM double-hat structures using an Instron Dynatup 8120 drop tower with a 102 kg head weight, as pictured in Figure 4.16. Fixtures are designed to constrain the ends of the double-hat structures. Shown in Figure 4.17, a top fixture is used to ensure the loading is evenly distributed to the top end of the sample. A channel is machined to keep the top plate from slipping off the structure. The bottom fixture is designed with a plug bolted onto a base plate, and a c-clamp to fasten the double-hat structure to the plug.

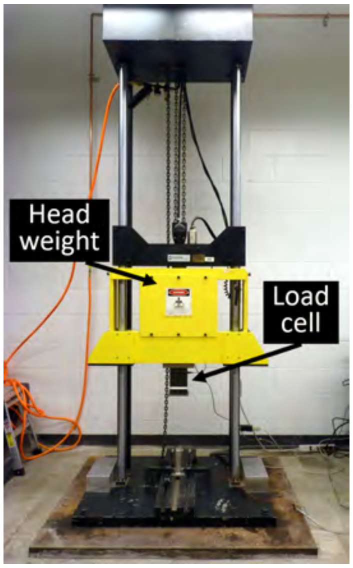
Head weight
Load cell

Figure 4.16: Drop tower for axial crush testing.

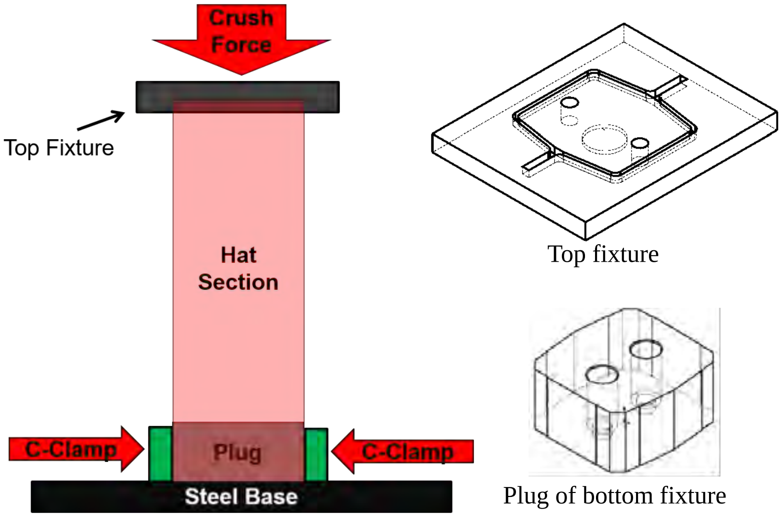
Crush Force
Top Fixture
Hat Section
C-Clamp
Plug
C-Clamp
Steel Base
Top fixture
Plug of bottom fixture

Figure 4.17: Schematics of fixtures for axial crush testing.

Figure 4.18 shows the axial crush test setup. A Phantom high-speed camera is set up to record the displacement by taking images of the speckled tape on the drop-tower crosshead. Two Photron high-speed cameras are used for capturing images of the samples during the test for DIC analysis. The signal from the load cell is run through a Vishay signal conditioner and recorded on a digital oscilloscope. Pictures of a riveted sample in the fixture before and after testing are shown in Figure 4.18 (b) and (c), respectively. One side of the samples are painted white and then speckled for DIC analysis. However, shortly after the impact, the DIC system cannot precisely process the captured images due to the airborne CFRP fragments that block the view of the structure from the cameras. Therefore, the strain maps are not shown in this article. Figure 4.19 shows pictures of a riveted sample during axial crush testing.

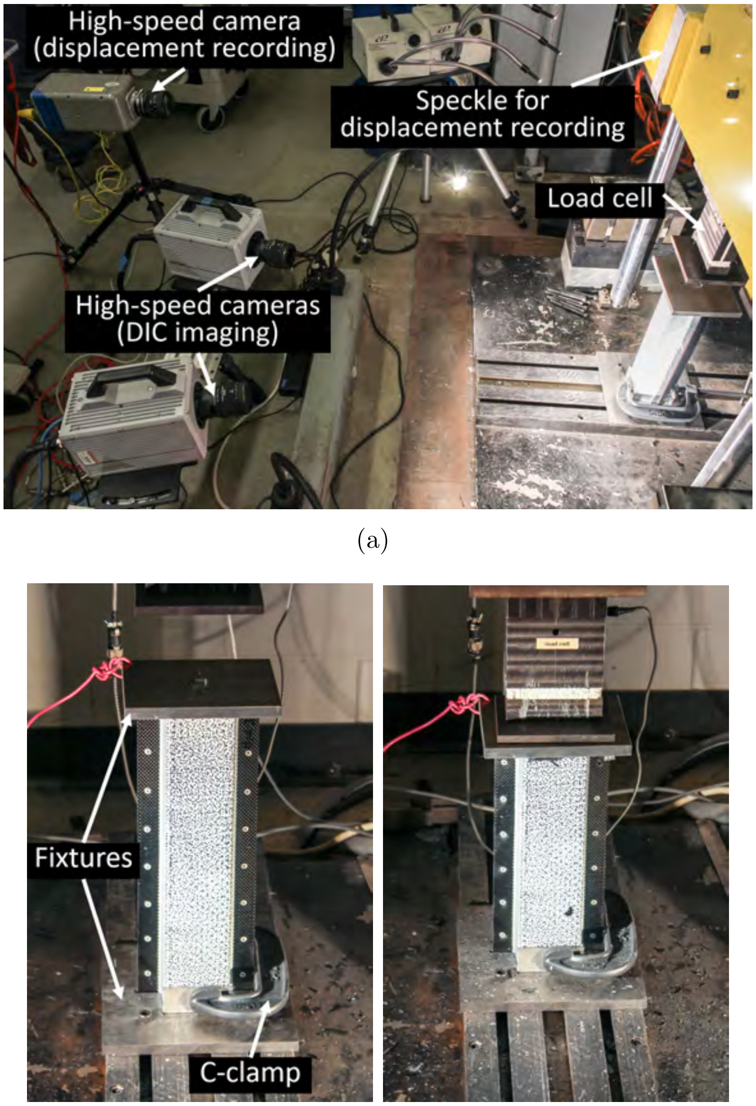
High-speed camera
(displacement recording)
Speckle for
displacement recording
Load cell
High-speed cameras
(DIC imaging)
Fixtures
C-clamp

(a)

(b) (c)

Figure 4.18: Axial crush testing setup: (a) cameras set up for data collection; (b) riveted sample in the fixture before testing; (c) riveted sample in the fixture after crushing.

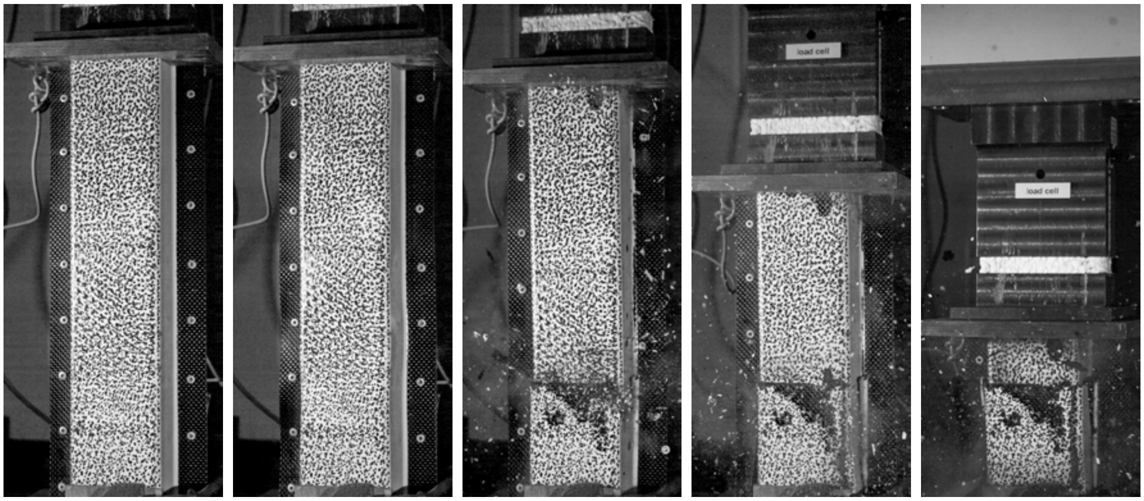

(a) t=0; d=0 (b) t=0.8; d=4.5 (c) t=5; d=20.4 (d) t=27; d=100.0 (e) t=82; d=207.2

Figure 4.19: Sample Rivet-c-3 during axial crush testing. Units: time - ms; displacement - mm.

4.4.2 Results and discussion

Figure 4.20 shows load vs. displacement curves from the dynamic axial crush tests. The three typical stages in the dynamic axial crush tests of thin-walled composite structures can be identified in the curves. The peak crushing loads indicate the impact when the header hits the top fixture. The riveted samples exhibit a higher initial peak crushing force than the UAM samples, which indicates the load transmitted to the occupants from a crashworthiness perspective. After the peak force, there is a transition zone that extends to a displacement of 20 mm, where the load drops from the initial peak and oscillates until reaching the stable zone. The final stage is a stable crush zone that extends until the test ends. The UAM samples have the smallest crushing length, which indicates a safer space for the occupants when a crash occurs. The energy absorption is calculated by integrating the load over the displacement. These curves are plotted versus displacement in Figure 4.21.

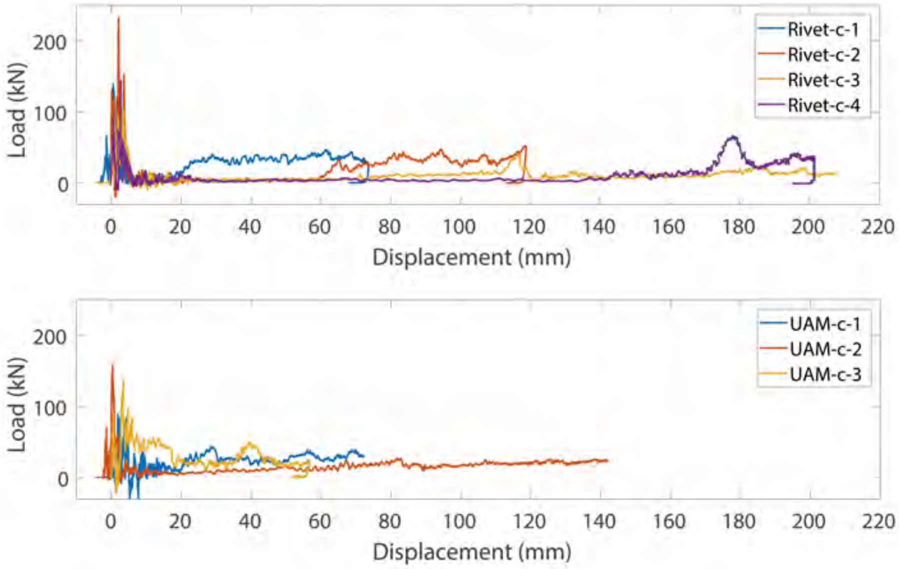

Figure 4.20: Load vs. displacement plots of axial crush samples: (a) riveted samples; (b) UAM samples.

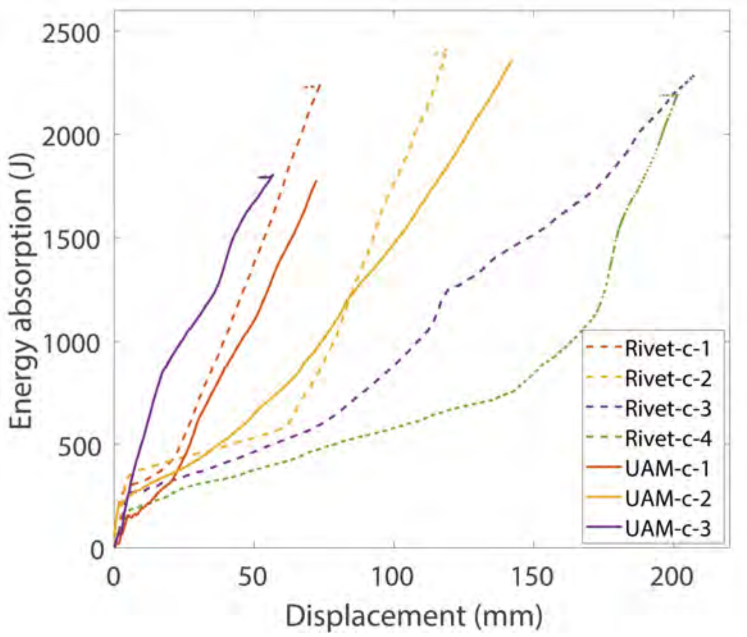

Figure 4.21: Energy absorption vs. displacement plot of axial crush samples.

Tabulated axial crush test results are listed in Table 4.5. The UAM samples have a 40% shorter crushing distance and 18% lower peak crushing load. To calculate the energy absorption, average load, and crush force efficiency, values corresponding to displacements of 0 to 50 mm of crosshead travel after the first impact are used. The UAM samples show ability to absorb 66% more energy and have 97% higher crush force efficiency compared with the riveted samples. Hence, the results indicate that the UAM samples are superior to the benchmark samples in terms of crashworthiness.

Table 4.5: Dynamic axial crush performance of riveted and UAM samples.

	Maximum distance (mm)	Peak Load (kN)	Energy absorption (J)	Average Load (kN)	Crush force efficiency
Rivet-c-1	73.7	139.7	1378.4	27.6	0.20
Rivet-c-2	118.9	233.1	533.3	10.7	0.05
Rivet-c-3	207.2	105.3	465.3	9.3	0.08
Rivet-c-4	201.4	144.8	377.3	7.6	0.05
Average	150.3	155.7	688.6	13.8	0.095
Standard deviation	65.1	54.5	464.3	9.3	0.071
UAM-c-1	72.2	89.6	1101.2	22.0	0.24
UAM-c-2	142.0	159.0	648.5	13.0	0.08
UAM-c-3	56.7	136.6	1672.8	33.5	0.24
Average	90.3	128.4	1140.8	22.8	0.187
Standard deviation	45.4	35.4	513.3	10.3	0.092

Pictures of all axial crush samples after testing are shown in Figure 4.22. Samples Rivet-c-1, Rivet-c-2, and Rivet-c-3 remain intact at the bottom of the structure. However, Rivet-c-4 broke into several pieces under the axial crush load. For the UAM samples, they are all able to maintain the integrity of the base of the structure during crushing. UAM-c-2 is the only UAM sample that has large front and back fronds and crushed farther than the other two samples as a result.

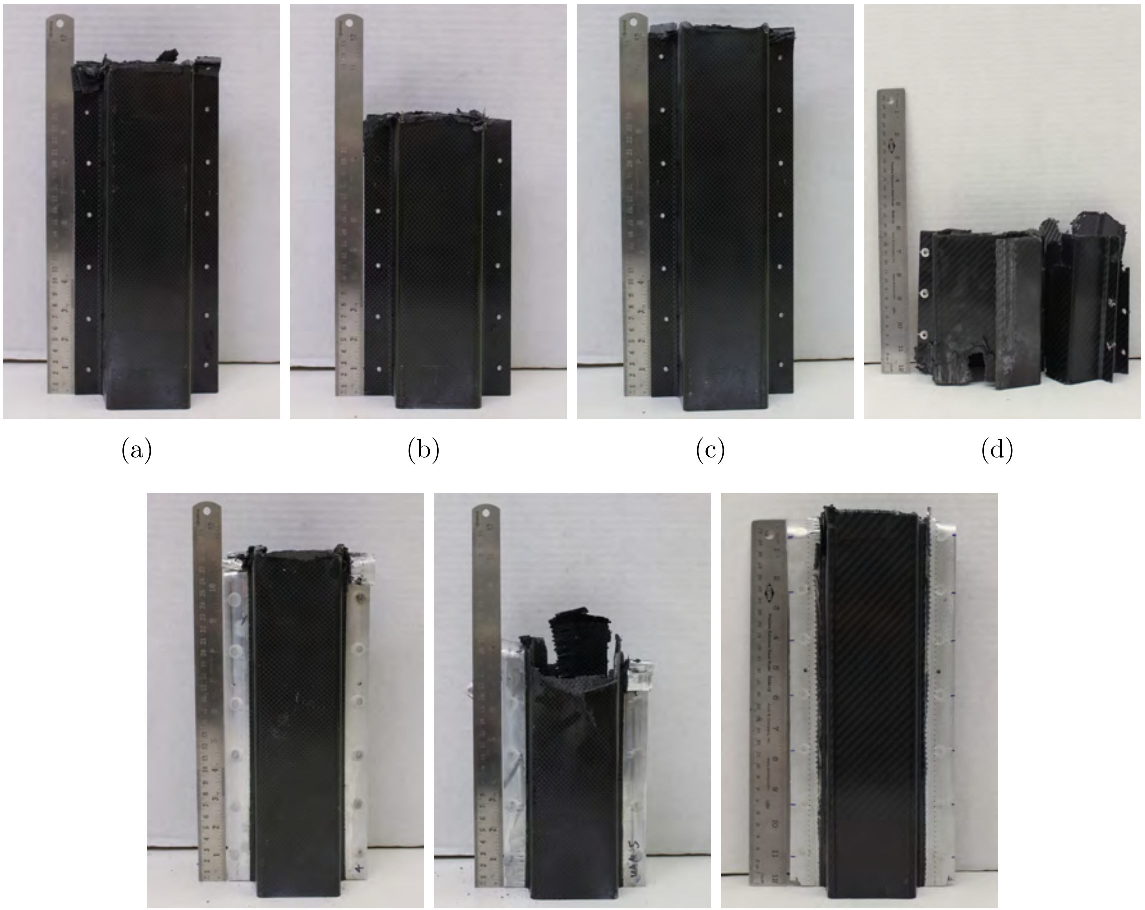

(a) (b) (c) (d)

(e) (f) (g)

Figure 4.22: CFRP double-hat structures after axial crush testing: (a) to (d) riveted samples; (e) to (g) UAM samples.

Inspecting the flanges on the failed samples, there is a considerable difference between the failure modes of riveted and UAM flanges. As shown in Figure 4.23 (a), the CFRP flange with rivets crushes into several pieces and wedges into the gap between two flanges. This accelerates the breaking of the next rivet. When the UAM flange is crushed, the AA transition flanges deform and buckle together, as shown in

Figure 4.23 (b). This prevents fragmented flanges from wedging between the hats, which could otherwise accelerate the destruction of the sample.

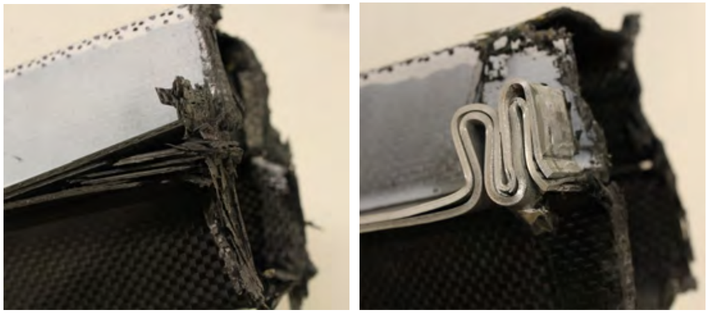

(a) (b)

Figure 4.23: Failed flanges after axial crush testing: (a) riveted samples; (b) UAM samples.

4.4.3 Conclusion

Dynamic axial crush test results show that the UAM AA flanges provide benefit to the double-hat CFRP structures in terms of crashworthiness by decreasing the initial crushing peak force and the crushing distance. The AA flanges prevent the CFRP debris from wedging into the joint region, preventing accelerated structural failure progression.

4.5 Torsion tests

4.5.1 Experimental method

Quasi-static torsion tests are performed at Honda R&D Americas using an MTS 215.42C actuator. The tests are performed at a rate of $1°/s$ and are tested to 100°. The torsion testing setup is shown in Figure 4.24 with both ends of the sample tightly fitted in the fixtures. The right end is rotated by an actuator while the left end remains static. The torque and twist angle are recorded during the tests on four UAM and four riveted samples. All the samples are made with 0/90° CF fabrics. This is not an ideal layup configuration for torsional loading, but the purpose of this test is to evaluate the performance of the joints on the flanges, which makes the CFRP layup configuration of little importance. This test is unique in that it places the discrete joints under a shear load in the plane of the flanges. This loading condition is not applied in the previous structural tests.

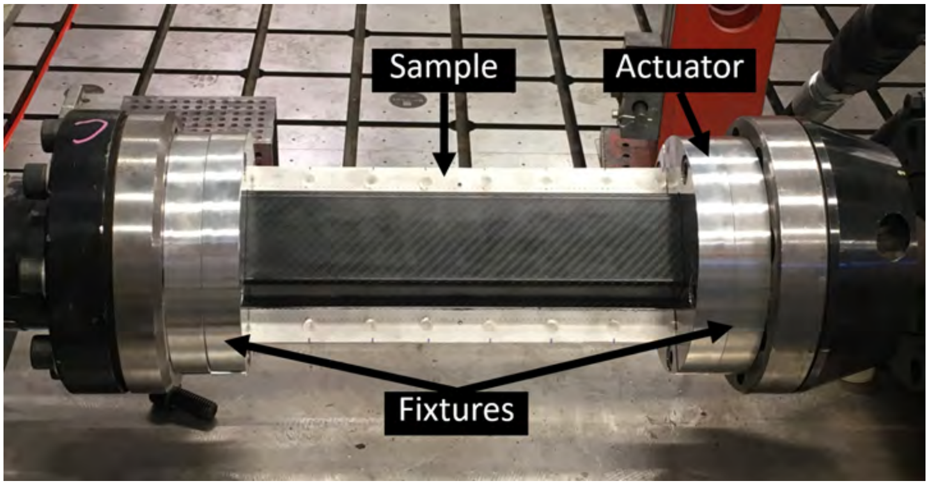

Figure 4.24: Setup for torsion tests.

4.5.2 Results and discussion

Figure 4.25 shows the curves for the rivet samples with different x-axis scales. Figure 4.25 (b) expands the portion of the curves before the failure point. For all four samples, the pre-failure peaks correspond to initial cracking in the structures. The large torque drop of sample Rivet-t-1 corresponds to a big crack in the CFRP.

Unlike sample Rivet-t-1, the primary force drops of the other three samples are caused by the simultaneous shearing of the rivets.

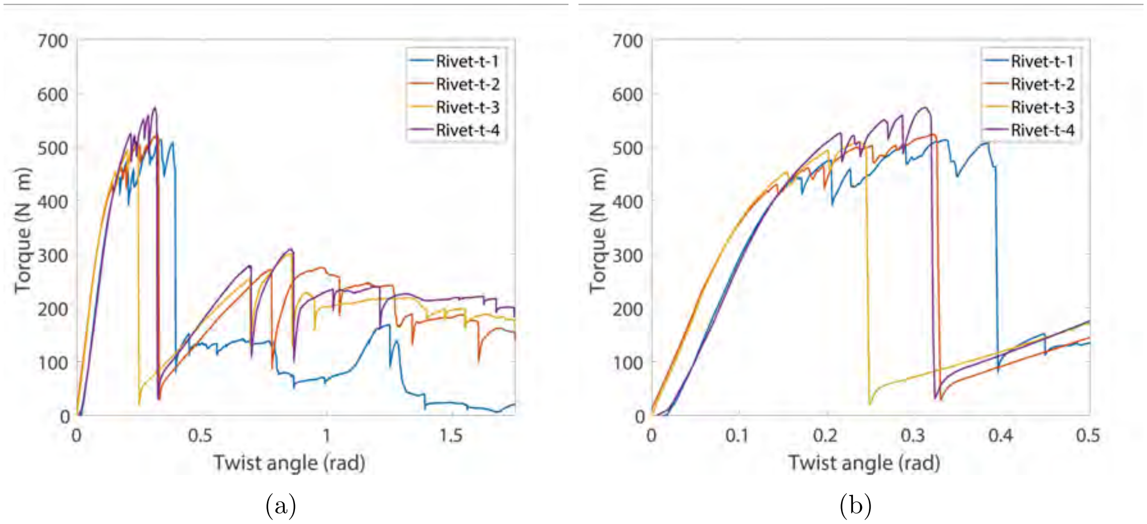

(a)

(b)

Figure 4.25: Torque vs. twist angle curves for rivet samples: (a) 0 to 1.75 rad (100 degrees); (b) 0 to 0.5 rad (29 degrees).

Figure 4.26 shows the torque vs. twist angle curves for UAM samples. The samples exhibit similar peaks as the riveted samples before the large torque drop. After the initial oscillation stage, the UAM samples failed in the bulk portion of the CFRP, which corresponds to the major torque drop in the curves.

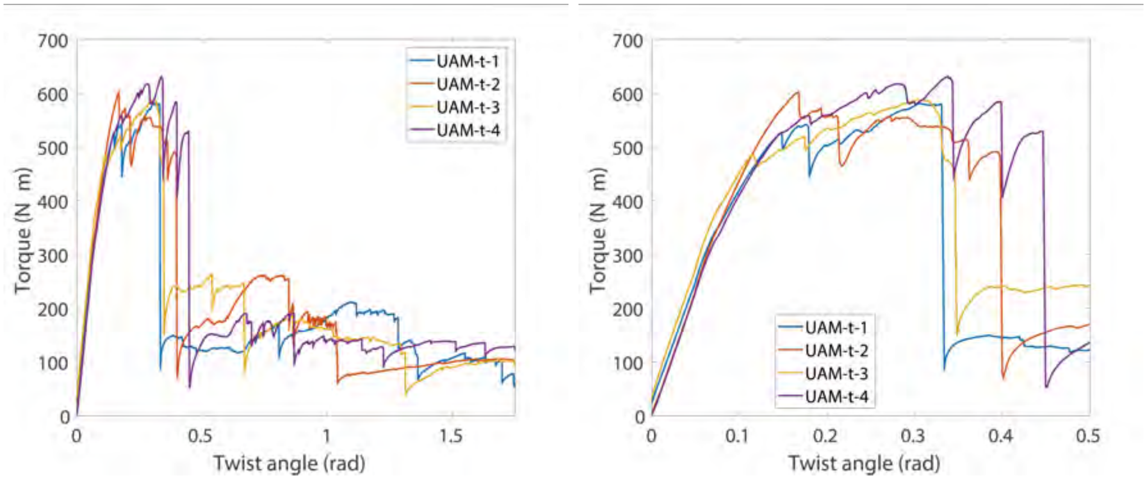

(a) (b)

Figure 4.26: Torque vs. twist angle curves for UAM samples: (a) 0 to 1.75 rad (100 degrees); (b) 0 to 0.5 rad (29 degrees).

The torsion test results are shown in Table 4.6. The average peak torque and energy absorption of the UAM samples are 13% and 48% higher than riveted samples, respectively. The average twist angle at failure of UAM samples is 16% larger than rivet samples. This indicates that the UAM AA flanges not only enable the structure to carry higher torque and absorb more energy, but also help with delaying the failure.

Table 4.6: Torsion test results for UAM and rivet samples

	Peak torque (N*m)	Energy absorption until failure (N*m*rad)	Angle at failure (rad)
Rivet-t-1	512.8	143.7	0.40
Rivet-t-2	522.9	125.1	0.32
Rivet-t-3	509.4	85.6	0.24
Rivet-t-4	573.1	116.8	0.31
Average	529.55	117.80	0.318
Standard deviation	29.59	24.23	0.066
UAM-t-1	581.1	146.3	0.33
UAM-t-2	602.1	181.1	0.39
UAM-t-3	587.4	157.7	0.31
UAM-t-4	631.3	213.5	0.45
Average	600.48	174.65	0.370
Standard deviation	22.35	29.67	0.063

Pictures of post-test UAM samples are shown in Figure 4.28. UAM-t-2 is the only sample where the CFRP hat failed along a 45° direction, which is a typical failure mode for torsion tests. UAM-t-1 is the only sample that has a long CFRP frond that separated from the structure during testing.

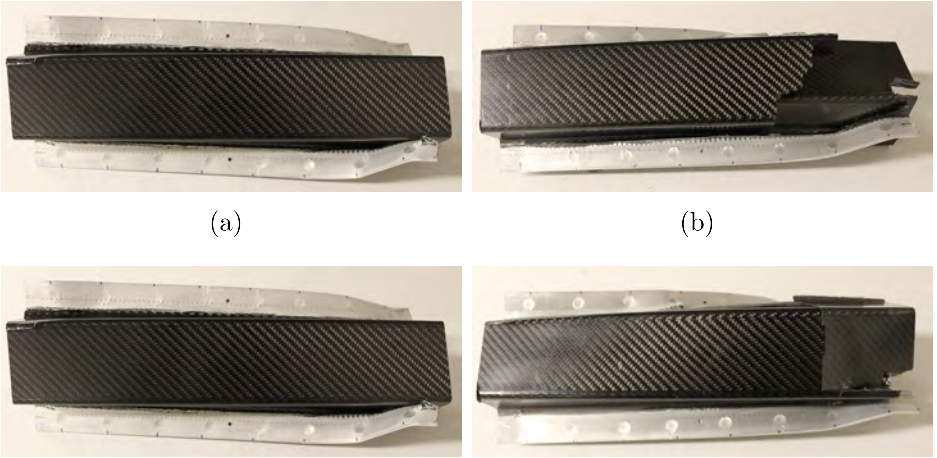
(a) (b) (c) (d)

Figure 4.27: Pictures of the UAM samples after torsion tests: (a) UAM-t-1; (b) UAM-t-2; (c) UAM-t-3; (d) UAM-t-4.

Most samples have a portion of CFRP that has been twisted and broken, as shown in Figure 4.28 (a). Figure 4.28 (b) pictures the common failure mode in the UAM samples, which is CFRP tow shearing along the CFRP-AA interface at the outer corners of the hats. This failure mode is expected because of high stress concentration at this interface coupled with the susceptibility of CFRP to compression and shear loading. Two uncommon failures are also observed in the tested samples. In sample UAM-t-2, a small section of a CFRP-AA flange failed by AA matrix breaking, as shown in Figure 4.28 (c). Another failure is shown in (d), where the AA flange broke around an RSW on UAM-t-4. This is the only instance of RSW failure observed in these tests.

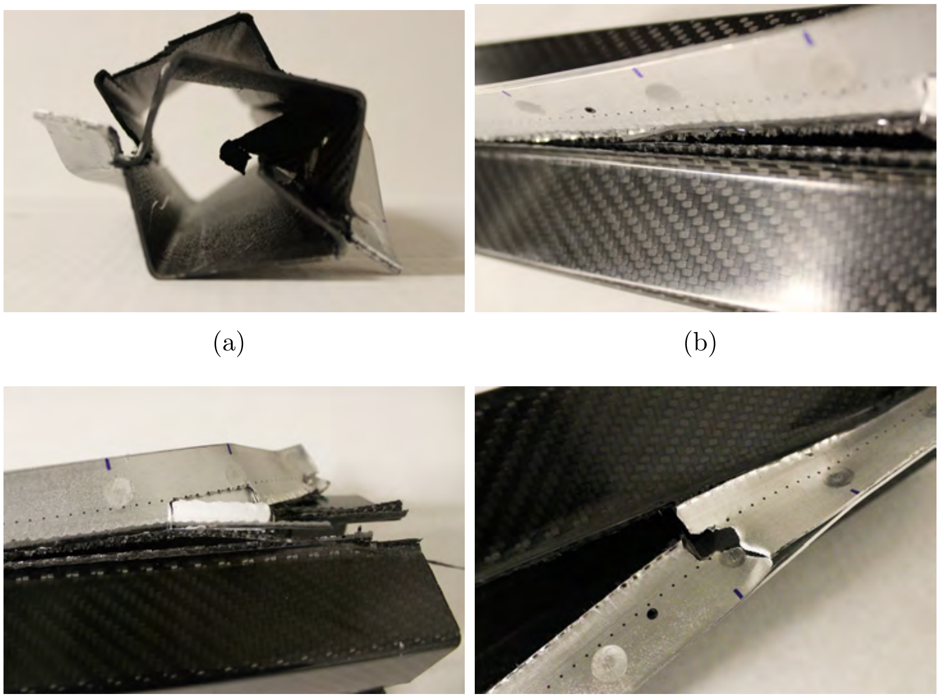

(a) (b)

(c) (d)

Figure 4.28: Failure modes in UAM samples: (a) CFRP hat breaking; (b) CFRP tow shearing; (c) AA matrix breaking; (d) AA flange breaking (RSW plug fracture).

As shown in Figure 4.29, three of the riveted samples failed by shearing ofrivets, and one sample (Rivet-t-1) failed in the CFRP. On sample Rivet-t-1, there is also a long CFRP frond that fell apart, which is similar to the failure of UAM-t-1. For the other three samples, all rivets on the failed side of the sample sheared simultaneously during the tests. Figure 4.30 (a) shows the CFRP flanges that completely separate due to the failure of all rivets along one flange. Because there is no constraint on this side of the sample after the rivet failures occurred, the beam is completely opened during the remainder of the test. This is quite different than the UAM samples, where the two CFRP hats are always constrained by the UAM flanges until the gradual CFRP tow shearing along the CFRP-AA interface. This difference explains why the CFRP hat-breaking mode occurs in UAM samples, but not in riveted samples. Figure 4.30 shows a sheared rivet to illustrate that the rivets did not fail by slipping between the two parts. Instead, they failed by shearing of the rivet shank.

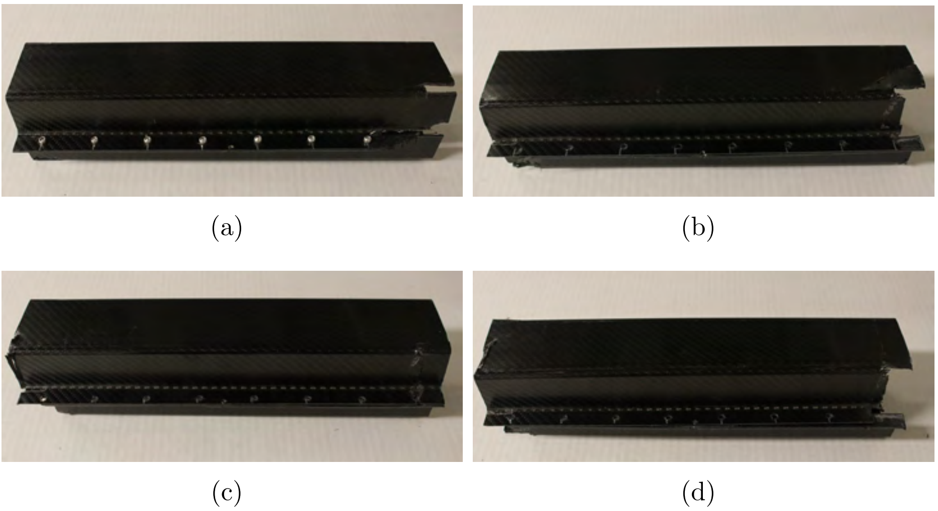
(a) (b) (c) (d)

Figure 4.29: Pictures of each side of the rivet samples after torsion tests: (a) Rivet-t-1; (b) Rivet-t-2; (c) Rivet-t-3; (d) Rivet-t-4.

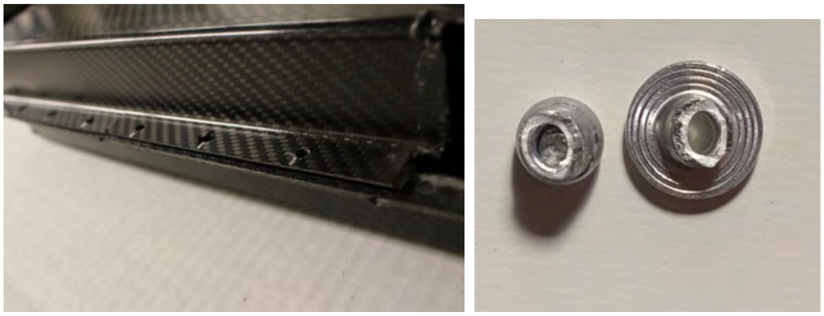

(a) (b)

Figure 4.30: Rivet shearing in rivet samples: (a) all the rivets sheared off along one side of the flange; (b) a sheared rivet.

4.5.3 Conclusion

The quasi-static torsion tests on the double-hat structures suggest that the UAM AA flanges help the structure to maintain integrity under torsional loading. Differing from the abrupt rivet shearing that is present in the benchmark samples, the UAM samples fail gradually and delay the ultimate failure. Furthermore, the AA flange design also provides benefit to the structure with slightly higher peak torque and significantly larger energy absorption.

4.6 Summary

In this study, the CFRP-AA joining constructed by UAM are applied to construct CFRP hat-shaped structures with AA flanges. Hybrid top-hat and double-hat structures were created using RSW to join the AA flanges to an AA plate or another hybrid hat. Baseline CFRP structures are manufactured by joining a CFRP hat to AA plate or another CFRP hat using pop rivets. Structure-level mechanical tests were performed to evaluate the performance of the joints.

- The four-point-bend tests show that average peak loads of UAM and riveted samples are similar while the average energy absorption and crush force efficiency of UAM samples are 86.3% and 83.7% higher than riveted samples, respectively. The riveted samples fail in the rivets leading to separation between the CFRP flange and AA plate. As soon as one or more rivets fail, the load-carrying ability of the sample dramatically decreases. As for the UAM sample, the UAM CFRP-AA transition enables the flanges to deform with the AA plate. Therefore, the UAM transition can avoid abrupt joint failure and continue carrying a high load until the CFRP hat fails.

- The axial crush tests show that UAM double-hat structures exhibit greater consistency in axial crush performance than the riveted double-hat structures. The crushing peak load of UAM samples is 18% lower, and the 90.3 mm average crushing distance of the UAM samples is 40% less when comparing to the riveted baseline samples. In terms of EA at 50 mm crush distance, the average EA of the UAM samples is 66% higher than the baseline samples. The UAM samples also exhibit twice the crush force efficiency of the riveted samples. The UAM AA flanges prevent the CFRP fragments from wedging into the flanges, which would otherwise accelerate the structure failure.

- For the torsion results, the UAM samples have 13% higher peak torque and 48% higher energy absorption until failure compared with riveted samples. The riveted samples fail by abrupt shearing of all rivets on one side, which significantly harms the integrity of the beams. On the contrary, the UAM samples fail by gradual shearing of the CFRP-AA interface and maintain the structural integrity after the initial cracking occurs. The UAM flanges appear to delay the failure by 3°.

Chapter 5: Analytical and Finite Element Models of FRP-metal UAM Joints

5.1 Analytical model

An analytical model has been built for the FRP-metal UAM joints to predict the failure of the joints in tension based on material properties and joint geometries. Firstly, the model calculates the stress in the embedded fibers with a tension loading based on the thick-wall cylindrical pressure vessel theory[8, 17]. Next, Tsai-Wu failure criterion [47] was applied to calculate the tensile load that each loop is able to carry. The load that the embedded FRP component can carry is calculated by multiplying the number of embedded loops by the load per loop. The strength of the metal matrix component is calculated based on the projection area of the cross-section along the fracture line. Finally, the peak load of the joint under tensile loading is the minimum between FRP component and metal matrix peak loads.

The model was developed based on the following assumptions:

1. Inner pressure from the metal pillar that is wrapped around by the fibers is evenly distributed

2. No friction between the embedded FRP and the metal matrix

3. Epoxy bonding between the embedded FRP and metal is negligible
4. Residue stress is not taken into account
5. The dimensions of embedded FRP equal to the dimensions of the channel
6. The curved portion of the loop is one-quarter of a circle with a radius of r_i
7. Stress change does not occur in the circumference direction, but only in the radial direction
8. Shear stress in the FRP is not taken into account.

The mathematical notations used in this section are listed below. Figure 5.1 illustrates the directions and geometry-related notations of the model.

u - radial displacement

ϵ_r - radial strain

ϵ_t - circumferential strain

ϵ_z - transverse strain

σ_r - radial stress

σ_t - circumferential stress

σ_z - transverse stress

E_1 - elastic modulus of the FRP along fiber direction (circumference direction globally)

E_2 - elastic modulus of the FRP perpendicular to fiber direction (radial or transverse direction)

E - $\sqrt{E_1/E_2}$

v_{nn} - Poisson's ratio in nn direction, where n=1 is circumference direction, n=2 is radial direction, and n=3 is transverse direction

p_i - stress applied to the inner circumference of the FRP

r_i - inner radius of the embedded FRP loop

r_a - outer radius of the embedded FRP loop

T - tensile load carried by each embedded FRP tow, the load carried by each FRP loop is 2T

θ - tilt angle of the straight portion in the loop

d - thickness of the FRP loop

k - coefficient of FRP strength due to stress concentration

N - total number of layers of FRP

F_F - fracture load of the FRP component

F_M - fracture load of the maatrix component

L_f - number of FRP layers

D_f - FRP loop spacing, i.e., loop arc center-to-center distance

h - FRP-metal joint thickness

A_m - bearing area of the metal

σ_m - tensile strength of the metal

A_e - area of the epoxy on the matrix failure fracture surface

σ_e - tensile strength of epoxy-metal bonding

X_t - longitudinal tensile strength

X_c - longitudinal compressive strength

Y_t, Z_t - transverse tensile strength

Y_c, Z_t - transverse compressive strength

S_{12}, S_{23}, S_{31} - shear strength

$$F_{12} - -\frac{1}{2}\sqrt{\frac{1}{X_t X_c Y_t Y_c}}$$
$$F_{23} - -\frac{1}{2}\sqrt{\frac{1}{Y_t Y_c Z_t Z_c}}$$
$$F_{31} - -\frac{1}{2}\sqrt{\frac{1}{Z_t Z_c X_t X_c}}.$$

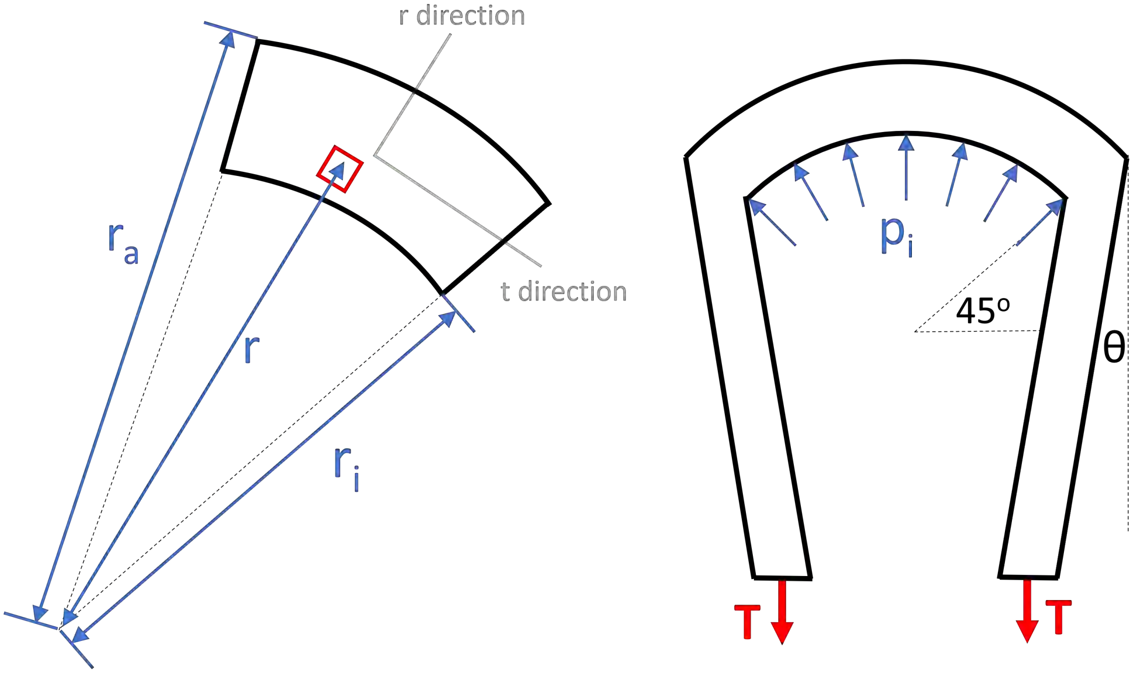

Figure 5.1: Schematic of the FRP loop for analytical modeling. Loop spacing is defined as the center-to-center distance between the two corners of the FRP tow in the loop.

The coefficients and parameters being applied in this study to obtain the correlation between model and experiments are listed in Table 5.1. The geometrical values are from the design described in Section 2.3. The mechanical properties of CFRP and AA matrix are from experiments or literature.

Table 5.1: Analytical model parameters of CFRP-AA joints

	Unit	Value	Source
θ	degree	8.3	Loop geometry
d	mm	0.1778	Loop geometry
channel width	mm	1.5875	Loop geometry
E_1	GPa	135.5	Literature [15]
E_2	GPa	8.9	Literature [15]
v_{12}, v_{13}	N/A	0.33	Literature [57]
v_{23}	N/A	0.48	Literature [57]
X_t	MPa	1688	Experiments (Appendix B)
X_c	MPa	268	Experiments (Appendix B)
Y_t	MPa	99.3	Literature [15]
Y_c	MPa	218	Literature [57]
S	MPa	89	Literature [57]
k	N/A	0.8	Calibration using experimental results
σ_m	MPa	195	Experiments
σ_e	MPa	50	Product datasheet

5.1.1 Stress in embedded FRP loops

When tension load is applied to the looped FRP, compressive stress is applied to the metal pillar that the FRP loop wraps around, which results in a compressive reaction force to the FRP loop. Based on the assumption that the compressive stress in the radial direction at the inner circumference of the loop is evenly distributed, the stress p_i can be calculated by

$$\int_{\frac{\pi}{4}}^{\frac{3\pi}{4}} p_i \sin\alpha d\alpha * d = 2\ \mathrm{T}\cos\theta \to p_i = \frac{\sqrt{2}T\cos^2\theta}{dr_i}. \tag{5.1}$$

The stress in the embedded FRP loops is firstly analyzed. The Euler-Cauchy equation that governs the radial displacement is

$$r^2\frac{d^2u}{dr^2}+r\frac{du}{dr}-\frac{E_1}{E_2}\frac{u}{r}=0. \tag{5.2}$$

Hooke's law in the radial coordinate system correlates stress and strain by the following equations:

$$\begin{aligned}
\varepsilon_t &= \frac{\sigma_t}{E_1}-v_{13}\frac{\sigma_z}{E_2}-v_{12}\frac{\sigma_r}{E_2},\\
\varepsilon_r &= \frac{\sigma_r}{E_2}-v_{21}\frac{\sigma_t}{E_1}-v_{23}\frac{\sigma_z}{E_2},\\
\varepsilon_z &= \frac{\sigma_z}{E_2}-v_{32}\frac{\sigma_r}{E_2}-v_{31}\frac{\sigma_t}{E_1}.
\end{aligned} \tag{5.3}$$

Assume uniform pressure along the inner radius of the loops, which is noted by p_i. In the transverse direction, assume metal to be rigid and not allow deformation. The boundary conditions are

$$\begin{gathered}
\sigma_r\left(r_i\right)=-p_i\\
\varepsilon_z=0.
\end{gathered} \tag{5.4}$$

By solving equations (5.2) to (5.4), stresses as a function of r can be expressed by

$$\begin{gathered}
\sigma_r(r)=\frac{-p_i r_i^{1+E}}{r_i^{2E}-r_a^{2E}}r^{E-1}+\frac{-p_i r_i^{1+E}}{r_i^{-2E}-r_a^{-2E}}r^{-E-1},\\
\sigma_t(r)=E\sigma_r(r),\\
\sigma_z(r)=\sigma_r v_{23}+\frac{E_2}{E_1}\sigma_t v_{21}.
\end{gathered} \tag{5.5}$$

The radial stress is related to the inner and outer radius of the loop and the inner stress from the pillar, which is a function of the applied tensile force and the geometry of the loops, as shown in equation (5.1). Note that the stress concentration from the transition kink from the straight to the curved portions of the loop is not considered in these equations.

The geometry and material properties of the loops in CFRP-AA samples tested in Section 2.3 are listed in Table 5.1. The CFRP modulus and Poisson's ratio are obtained from the literature characterizing CFRP of T300 carbon fiber, which is the type of carbon fiber used in the experiments of this project.

Figure 5.2 plots the stresses versus the radial location calculated by equations (5.5) with $T = 100$ using parameters listed in Table 5.1. The X-axis indicates the relative radial location where X=0 is the inner circumference of the loop, and X=1 is the outer circumference. The curves are plotted with loop inner radius r_i from 2 to 5 mm, with the color of lines from lightest to thickest. σ_r and σ_z are in compression, and σ_t is in tension. It can be observed that $|\sigma_t| > |\sigma_r| > |\sigma_z|$. Also, the stresses are the highest at the inner and lowest at the outer circumferences. This result agrees with the FEA result from the literature as shown in Figure 5.3 in terms of circumferential stress.

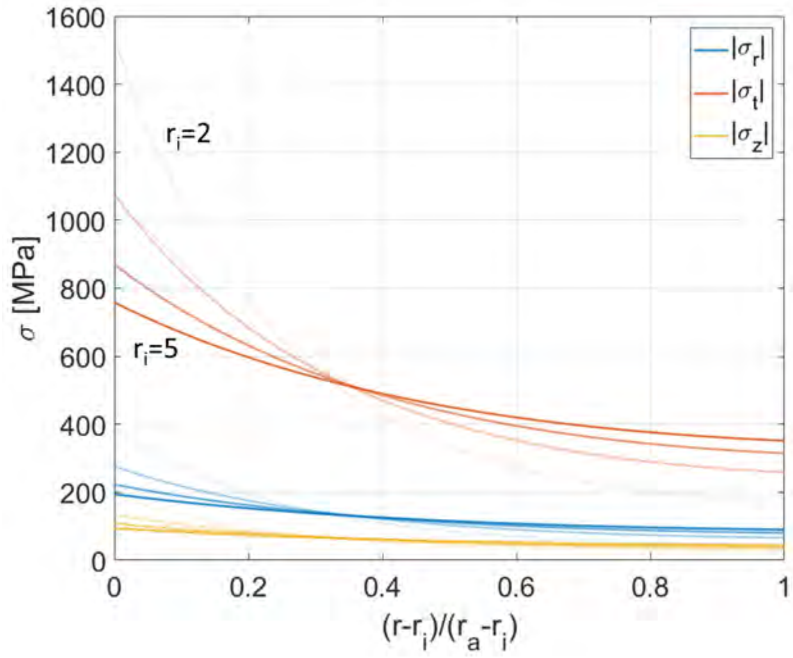

Figure 5.2: Stress distribution in the embedded FRP tow.

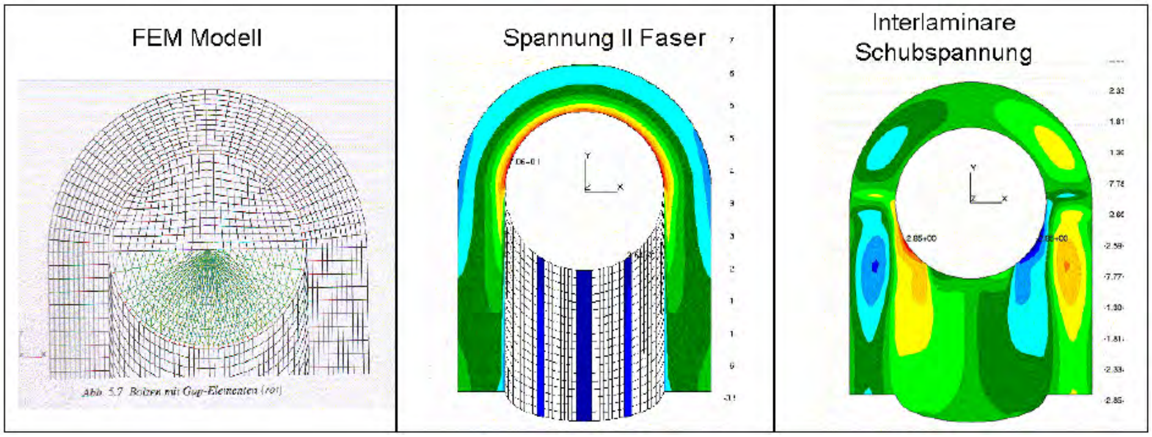
FEM Modell
Abb. 5.7 Bolzen mit Gap-Elementen (rot)
Spannung II Faser
Interlaminare Schubspannung

(a) (b) (c)

Figure 5.3: FEA result of a FRP strap wrapping around a rod[17]: (a) FEA mesh; (b) circumferential stress distribution; (c) inter-laminate shear stress distribution[17].

Based on the stress distribution analysis above, the maximum stress should locate at the inner circumference of the FRP loop and equal to p_i. Considering the stress concentration results from the kinks in the metal pillar, the failure of the FRP loop should initial from the inner point at the region where the loop transitions from straight to curved.

5.1.2 FRP-metal joint tensile strength

The Tsi-Wu failure criterion for orthotropic material is applied to characterize the fracture in the embedded FRP loop using the following equation:

$$\begin{aligned}&\left(\frac{1}{X_t}-\frac{1}{X_c}\right)\sigma_{\mathrm{t}}+\left(\frac{1}{Y_t}-\frac{1}{Y_c}\right)\sigma_r+\left(\frac{1}{Z_t}-\frac{1}{Z_c}\right)\sigma_z+\frac{\sigma_t^2}{X_tX_c}+\frac{\sigma_r^2}{Y_tY_c}+\frac{\sigma_z^2}{Z_tZ_c}+\\&\frac{\tau_{tr}^2}{\mathrm{S}_{12}^2}+\frac{\tau_{rz}^2}{\mathrm{S}_{23}^2}+\frac{\tau_{tZ}^2}{\mathrm{S}_{31}^2}+2F_{12}\sigma_t\sigma_r+2F_{23}\sigma_r\sigma_z+2F_{31}\sigma_t\sigma_z=1.\end{aligned} \tag{5.6}$$

The coefficients in equation (5.6) are determined from the strength of the FRP. For the coefficients that characterize material strength in bi-axial load cases (F_{12}, F_{23}, and F_{31}), it is not feasible to obtain it experimentally due to a lack of standard experimental methods. Therefore, an empirical expression is applied to calculate the coefficients based on the unidirectional strengths[26].

Based on the stress analysis described previously, fracture in the FRP is predicted to initial from the inner corner of the loop, where the stresses can be expressed as:

$$\begin{aligned}\sigma_r=p_i=\frac{\sqrt{2}T_0\cos^2\theta}{dr_i},\\ \sigma_t=Ep_i,\\ \sigma_z=p_iv_{23}+\sqrt{\frac{E_2}{E_1}}p_iv_{21}.\end{aligned} \tag{5.7}$$

The function to calculate the fracture load per FRP tow T_o can be obtained by substituting (5.7) into (5.6). To characterize the stress concentration effect due to the corner of the metal pillar, a factor k is proposed, and the actual fracture load per FRP tow is calculated by $T = kT_o$. The coefficient k should be calibrated using the experimental data.

Figure 5.4 plots the fracture load per tow versus the loop spacing using the parameters listed in Table 5.1. The plot shows a linear correlation between the fracture load and the loop spacing, which is also a linear function of r_i. The tensile tests reported in Section 2.3 were performed on samples with a 4.23 mm loop spacing. From the model, the expected fracture load is 187 N.

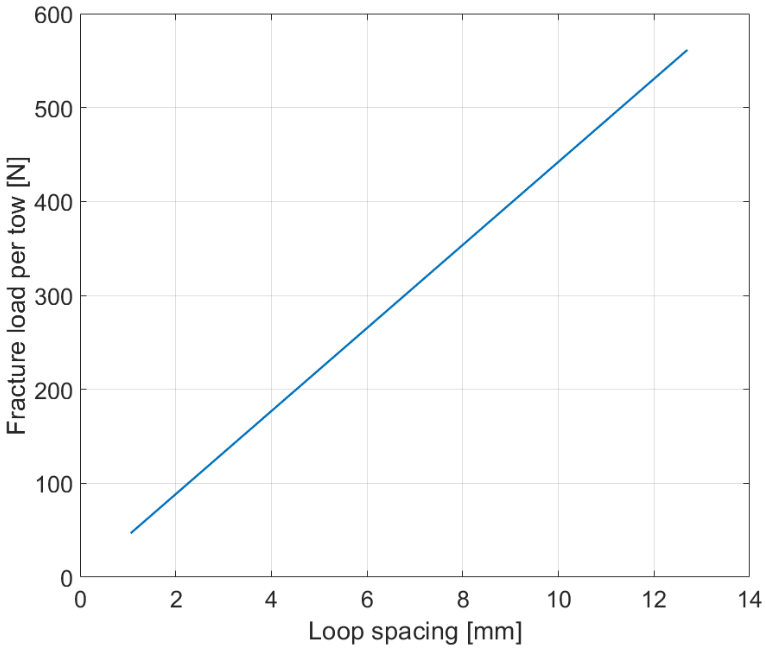

Figure 5.4: Peak load per tow.

In a tensile test on an FRP-metal joint, failure can occur in either FRP or metal. The strengths of FRP (F_F) and matrix (F_M) components are calculated. The joint tensile strength is dominated by the weaker component, which can be expressed by

$$F_J = min(F_F, F_M). \tag{5.8}$$

The fracture load of FRP (F_F) is obtained by multiplying fracture load per loop by the number of loops in the joint (N), which is a function of the number of layers of FRP (L_f) and the loop spacing (D_f). It should be noted that L_f is limited by the total thickness of the joint. The equation to calculate F_F is

$$F_F = TN(L_f, D_f). \tag{5.9}$$

The matrix failure mode is from the fracture in the metal and the FRP-metal bonding at the top of the loops. Using the cross-section projection schematic shown in Figure 2.15, the area of epoxy and metal can be calculated based on the joint geometry. Therefore, the matrix fracture load (F_M) is calculated from the bearing area and tensile strength of metal and epoxy using the equation:

$$F_M = \sigma_m A_m + \sigma_e A_e. \tag{5.10}$$

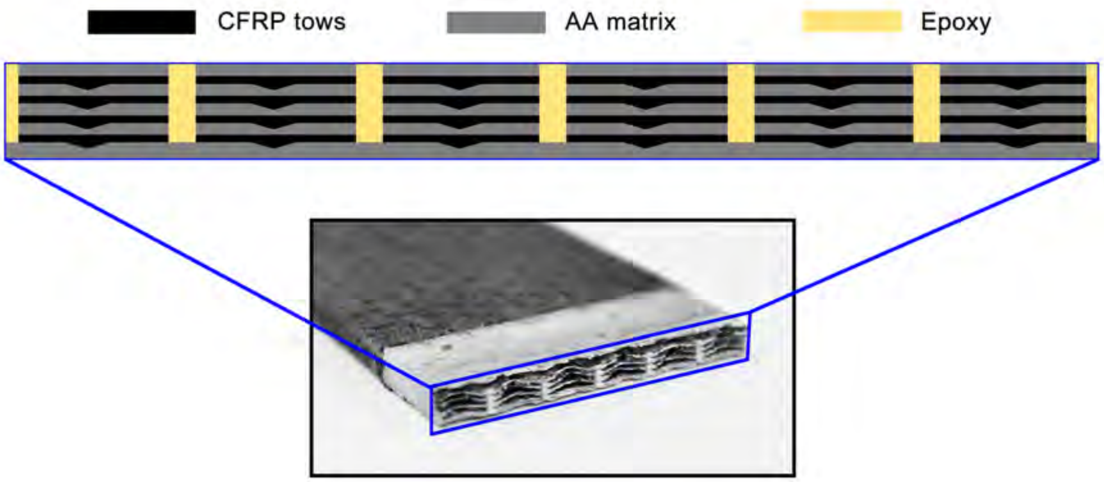

Figure 5.5: Projection of the cross-section along the fracture line.

Using the parameters listed in Table 5.1, the fracture load of a one-inch wide joint is plotted against joint thickness while varying L_f and D_f, as shown in Figure 5.6. Each curve in the plot has a slopped section and a horizontal section, which correspond to metal failure and FRP failure, respectively. When the joint is failing in the matrix, increasing the sample thickness may improve the joint strength. But when the thickness is increased until the weaker component shifts from the matrix to the fiber, failure would occur in the FRP and additional increment of the thickness can not lead to gain in joint strength.

From the plot, when the loop spacing (D_f) increases or the number of FRP layers (L_f) decreases, the total number of embedded FRP loops will decrease, which results in the peak load of FRP failure mode to drop. Also, the FRP component strength decreases with larger loop spacing or more FRP layers and makes the required sample thickness to create FRP failure decrease.

The thickest lines in the plots use the loop spacing of the tensile samples described in Section 2.3. It is predicted by the model that the 1.8 mm thick samples with 3 CF layers would fail in FRP at 5616 N, and the 2.2 mm thick samples with 4 CF layers would fail in the matrix at 7370 N. The comparison between model and experiments will be analyzed in Section 5.1.3.

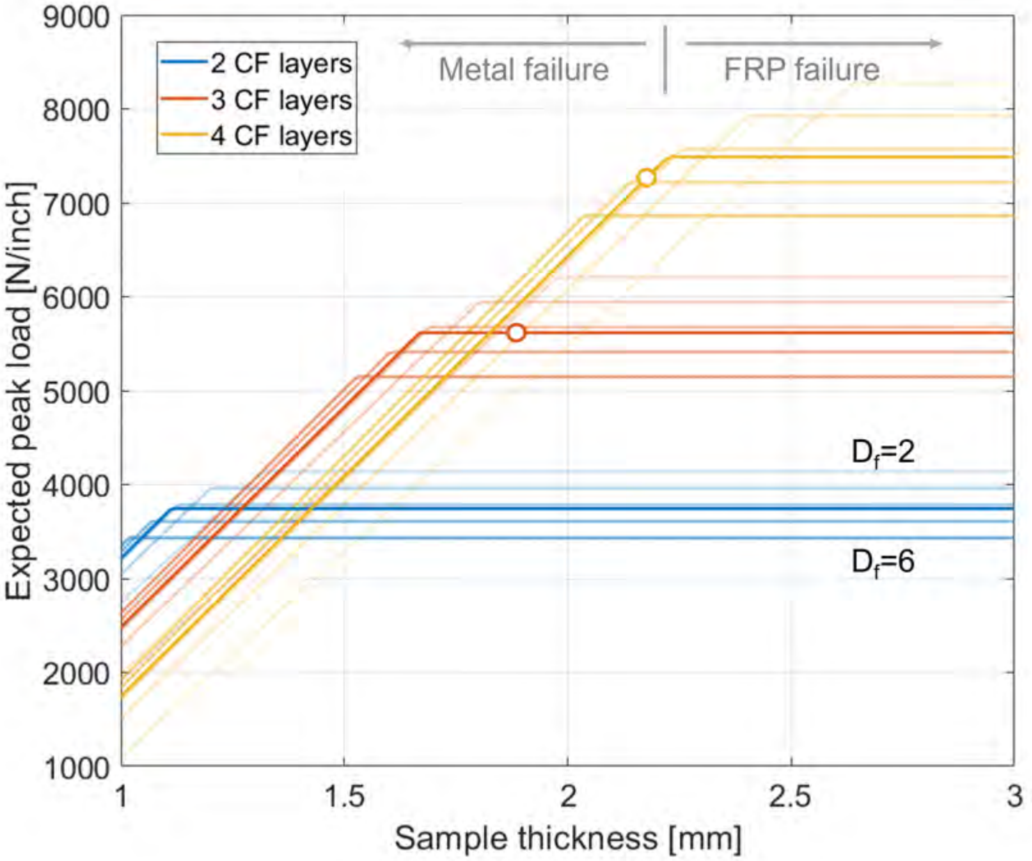

Figure 5.6: Peak load vs sample thickness.

Figure 5.7 plots the peak load vs. loop spacing from the model. For each curve, the left-hand-side curved section corresponds to matrix failure, and the right-hand-side linear section indicates failure in FRP. With a constant joint thickness and number of embedded FRP layers, the peak load and failure mode can be designed by tuning the loop spacing. If maximum peak load is desired, the load spacing should be determined as the value that correspond to the peak of the curve. However, when the design falls on the peak of the curve, the failure mode is at the threshold region, which indicates the failure mode may not be controlled precisely. If the preference is to obtain the desired failure mode, then the loop spacing should be chosen away from the threshold region while compromising the joint strength.

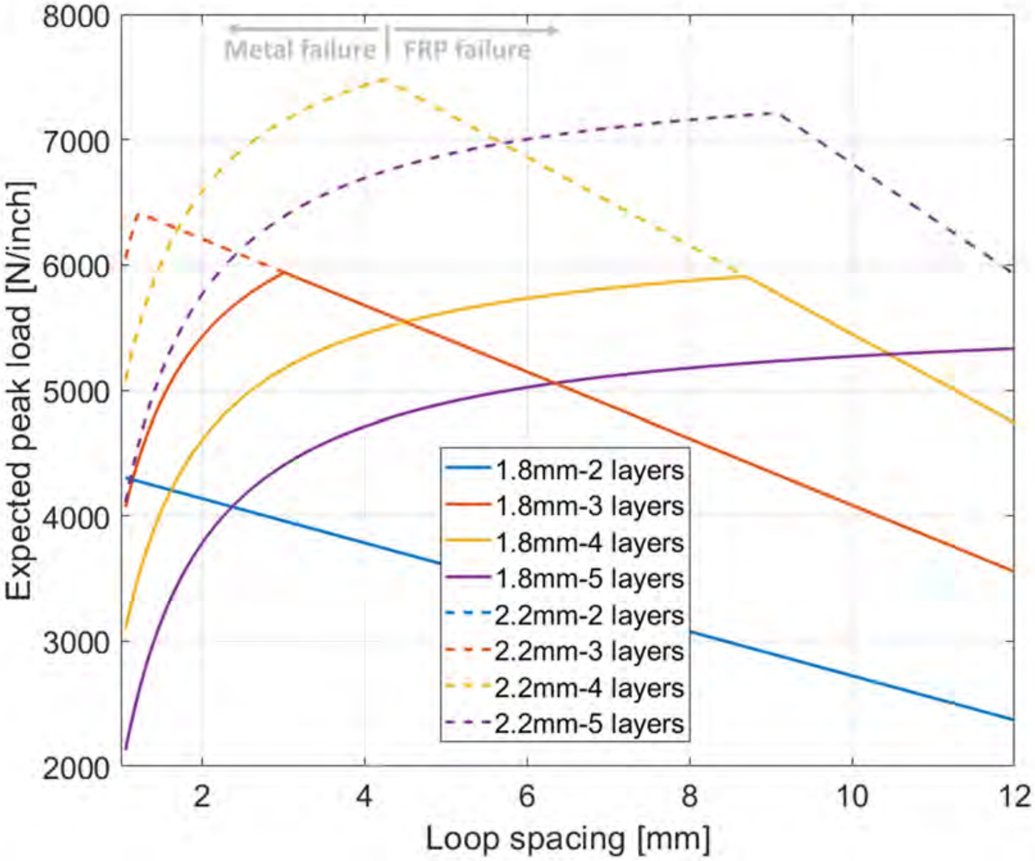

Figure 5.7: Peak load vs loop spacing.

5.1.3 Comparing CFRP-AA joint strength from experiments and the analytical model

The samples tested in Section 2 have a loop spacing of 4.23 mm. The experimental and predicted performance are plotted in Figure 5.8 and listed in Table 5.2. In addition to the tests reported in Section 2.3, additional tests have been performed on 1.8 mm thick samples with three embedded CFRP layers. The additional samples were created with techniques to ensure concurrent failure among the embedded CFRP loops by fully wetting the fibers using epoxy and applying tension on the fibers during curing. Details of the additional tests are included in Appendix C.

The analytical model is able to predict the failure mode for both sample configurations. For the 3-CF-layer joints, the experimental peak loads of #2 and #3 are higher than #1, indicating that concurrent fiber fracture is an essential factor in obtaining joint higher strength. The model prediction errors are 3.3% and 5.3% compared to experiments #2 and #3. In terms of the samples with 2.2 mm thickness, the analytical model can predict the peak load within 1.8%. The comparison proves that the analytical model can precisely predict the failure mode and peak load of the joints based on the material properties and joint design.

Table 5.2: Analytical and experimental results of tensile tests on CFRP-AA joints

Thickness	CFRP layers		Peak load	Failure mode
1.8 mm	3	Experiment #1 (Section 2.3)	4677 N	CFRP fracture
		Experiment #2 (Appendix C)	5804 N	
		Experiment #3 (Appendix C)	5320 N	
		Analytical model	5616 N	
2.2 mm	4	Experiment (Section 2.3)	7238 N	AA fracture
		Analytical model	7370 N	

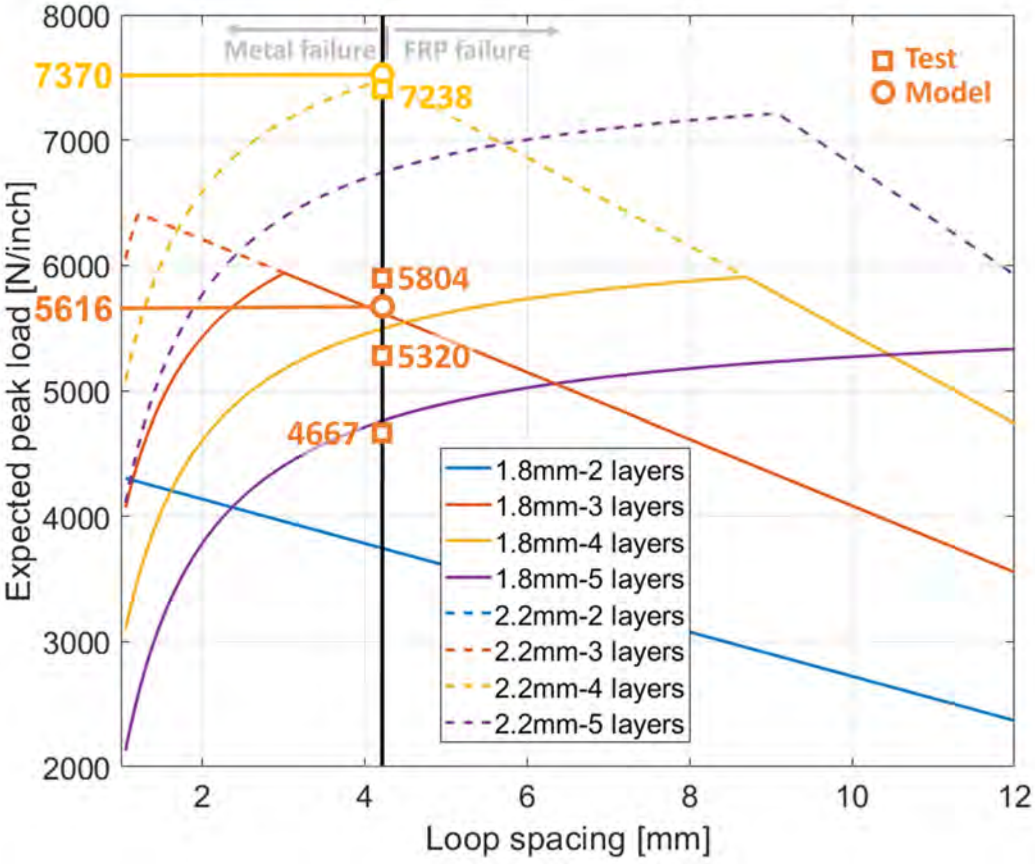

Figure 5.8: Peak load vs loop spacing with experimental results.

5.2 Finite element model

This study aims to explore a joining method to connect FRP to metal structures in the body-in-white (BIW) of vehicles. In the vehicle design process, FEA is a critical aspect of evaluating the performance of the BIW design. To promote the integration of the FRP-metal joint studied in this project into an industrial vehicle design, a feasible and effective method to characterize the joint using FEA is needed. This study uses LS-DYNA to perform the FEA analysis. Although LS-DYNA is well-known for its strong capability to perform dynamic simulation while most of the experimental tests performed in this project are quasi-static, it is used here to follow the industrial body analysis convention. Different popular tools are being used in the industry to analyze different aspects of the body structure, but the crash safety performance is of most interest in the joint characterization, which is commonly analyzed using LS-DYNA. The dynamic effect is minimized by tuning the step size and loading rate in the FEA model.

An initial attempt is to characterize the joint using solid elements. However, a mesh size of less than 0.5 mm is required to capture the embedded FRP tows in the joint, making applying this joint model to a vehicle-level model (typically using 2-5 mm mesh) impossible. Also, most of the panels and beams in the vehicle body are represented by shell elements, a solid model for the joint will raise challenges to create connections between the joint and the structures. Therefore, a shell mesh of the joint is proposed by homogenizing the hybrid portion of the joint, as shown in Figure 5.9. The shell mesh size is 2.5 mm, and the hybrid region is represented by four rows of elements.

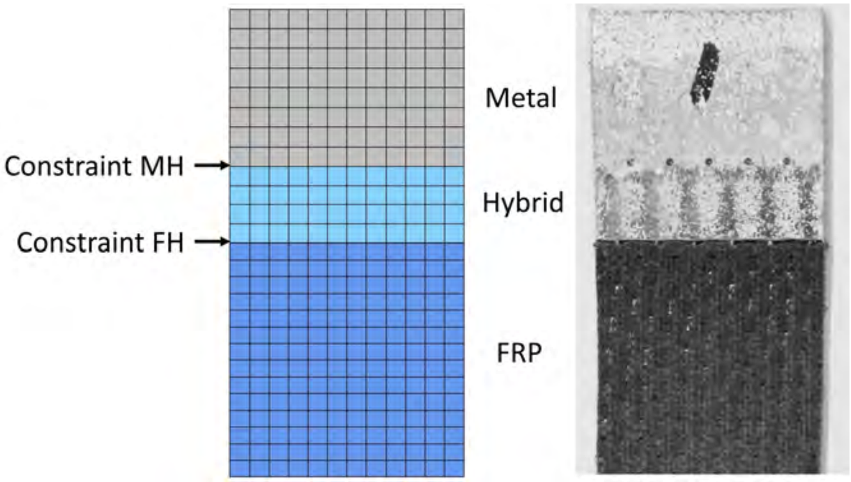

Figure 5.9: Shell mesh of a tensile joint with a 2.5 mm mesh size.

The CFRP-AA joints studied in Section 2.3 are modeled using the homogenized method. The AA material card is MAT24 calibrated from the 6061-T6 sheet to match the 195 MPa tensile strength of the UAM 6061-H18. The CFRP component uses MAT54 with parameters from the literature [6]. The hybrid part is modeled using MAT24 with parameters obtained from the rule of mixture based on the volume fraction of AA and CFRP. The connections at metal-hybrid (MH) and FRP-hybrid (FH) interfaces are modeled by CONSTRAINED_GENERALIZED_WELD with the butt weld option. This is a constraint originally developed to characterize butt welds. The parameters of this card are listed in Table 5.3. Constraint MH is modeled to capture the matrix failure model, and constraint FH characterizes the FRP failure mode. Therefore, the SIGY values are calculated based on the fracture forces of matrix and FRP components, using equations (5.9) and (5.10) in Section 5.1. The parameter L equals the width of the joint divided by the number of elements per row. The parameter D equals the thickness of the joint. The failure parameter BETA governs the fracture loads of the constraint, which has been calibrated based on the experimental result.

Table 5.3: CONSTRAINED_GENERALIZED_WELD parameters

Param.	Meaning	Unit	1.8 mm		2.2 mm	
			MH	FH	MH	FH
TFAIL	failure time	s	0			
EPSF	effective plastic strain at ductile failure	N/A	0.1			
SIGY	stress at failure for brittle failure	MPa	136.26	122.83	131.89	134
BETA	failure parameter for brittle failure	N/A	0.6	0.58	0.6	0.58
L	length of butt weld	mm	2.1167			
D	thickness of butt weld	mm	1.8		1.8	

The failure modes of the joints match the experimental results, as shown in Figure 5.10. The stress map shown in Figure 5.11 shows similar distribution when compared to the DIC strain map in Section 2.3. For the sample that failed at the hybrid/CFRP interface, the stress concentrates at the interface while the stress in the AA part is low. For the sample that failed in the hybrid/AA interface, the hybrid/AA interface has the highest stress, and there is still substantial stress at the hybrid/CFRP interface. From the fringe bar, the stress at the fracture region of the sample that failed in the CFRP is significantly higher than that in the sample that failed in AA. This also agrees with the DIC strain map.

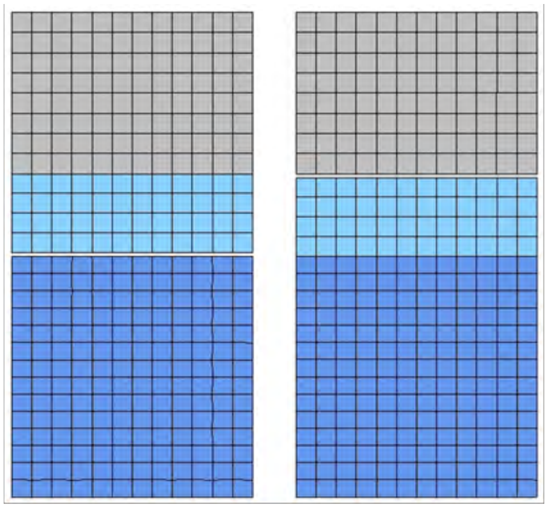

1.8 mm 3 CFRP layer 2.2 mm 4 CFRP layer

Figure 5.10: Tensile failure modes of CFRP-AA joints in FEA simulation.

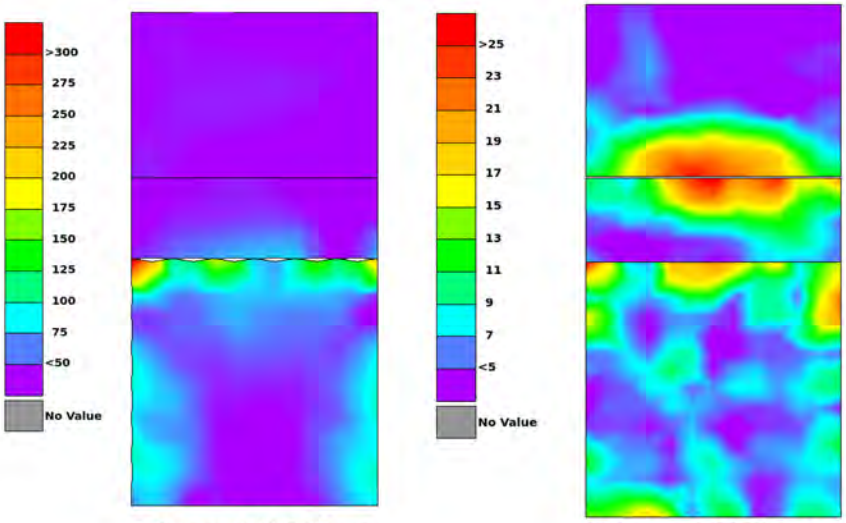

1.8 mm 3 CFRP layer 2.2 mm 4 CFRP layer

Figure 5.11: Stress distribution of CFRP-AA joints in FEA simulation.

Figure 5.12 plots the simulation and experiment results of the two joints. The experimental results are from the curves in Figure 2.9. For the 1.8 mm thick samples, the simulation predicts a failure in the CFRP at a 0.65 mm displacement and 5600 N force. Comparing the simulation to the experimental result, the displacement at failure matches very well, but there is a discrepancy in the peak force. However, as mentioned in Section 5.1, additional tensile tests have been performed on 1.8 mm thick samples with techniques to promote concurrent failure in the embedded FRP loops. As listed in Table 5.4, the peak forces of the additional experiments agree well with the FEA model. Unfortunately, the additional tests were not performed with the DIC system to record load displacement. Therefore, we do not have the displacement data that can be applied to compare to experiments #1 and the FEA model. Also, because the simulation cannot capture the fiber tow pullout process after the peak, the simulation exhibits an abrupt load drop instead of holding the load after the peak. This is expected because the interface is modeled by butt welds, which do not have this feature.

For the 2.2 mm thick samples, the simulation agrees very well with the experimental results in terms of both peak force and displacement at fracture with an error of less than 3%.

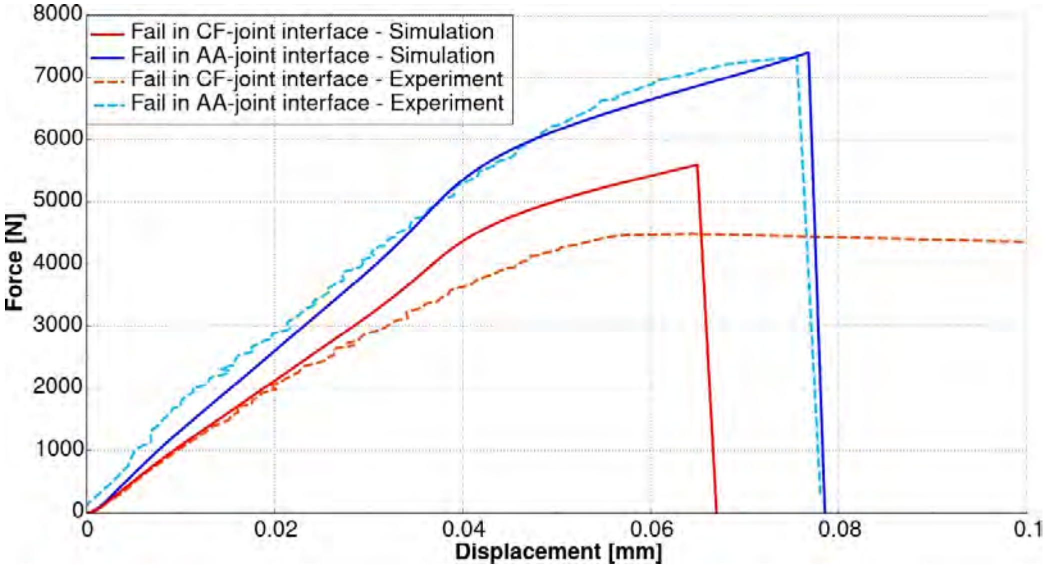

Figure 5.12: Load vs displacement curves of FEA and experiment results.

Table 5.4: Model and experimental results of tensile tests on CFRP-AA joints

Thickness	CFRP layers		Peak load	Failure Disp.	Failure mode
1.8 mm	3	Experiment #1 (Section 2.3)	4677 N	0.64 mm	CFRP fracture
		Experiment #2 (Appendix C)	5804 N	-	
		Experiment #3 (Appendix C)	5320 N	-	
		Analytical model	5616 N	-	
		FEA model	5600 N	0.65 mm	
2.2 mm	4	Experiment (Section 2.3)	7238 N	0.76 mm	AA fracture
		Analytical model	7370 N	-	
		FEA model	7403 N	0.77 mm	

5.3 Summary

An analytical model has been generated based on thick-wall pressure vessel theory to characterize the stress distribution in the embedded FRP loop and the FRP-metal join strength under tensile load. The model suggests that the fracture in the FRP should initiate from the inner corner of the loop due to maximum stress. With a narrower loop, the stress distribution in the FRP loop gets more uneven. The FRP-metal joint strength is dominated by the weaker component between FRP and matrix. Comparing the analytical model and experiment results, the model is able to predict the failure mode and peak load based on the material properties and joint geometry.

Based on the analytical model, an LS-DYNA FEA model has been developed with shell elements to simulate tensile tests on FRP-metal joints. The FEA model employs a constraint card that is commonly used to model butt welds. The parameters of the constraint are calculated from the analytical model. The simulation result agrees well with the experimental results regarding failure mode, peak load, and displacement at fracture.

Chapter 6: Corrosion Mitigation of CFRP-AA UAM Joints

6.1 Investigate the effect of galvanic corrosion on CFRP-AA joints

Galvanic corrosion occurs when two dissimilar conductive materials are in electrical contact and in the presence of an ionic connection. AA and CFRP are both conductive materials and have a large open circuit potential difference; therefore, constructing a direct joint between these two materials will lead to severe galvanic corrosion. The galvanic series lists that the corrosion potential measured in seawater of aluminum alloys is -1 to -0.75 V_{SCE} and that of graphite is 0.2 to 0.3 V_{SCE}. For the AA-CFRP joints, looped CFRP tows are embedded in the Al matrix for mechanical interlocking. This method increases the contact area between AA and CFRP and makes this combination more susceptible to galvanic corrosion.

6.1.1 Construct corrosion samples

Cyclic corrosion tests (CCT) were performed on CFRP-AA joints to investigate the galvanic corrosion effect. Six 254 mm wide CF/AA transition flanges were welded and cured, then labeled from A to E. All the flanges were made by welding nine layers of AA tape and three layers of AA sheet. After curing, nine 25.4 mm wide coupons were cut from each flange, and the samples were labeled from 1 to 9 for each flange. The picture of 54 coupon transitions is shown in Figure 6.1.

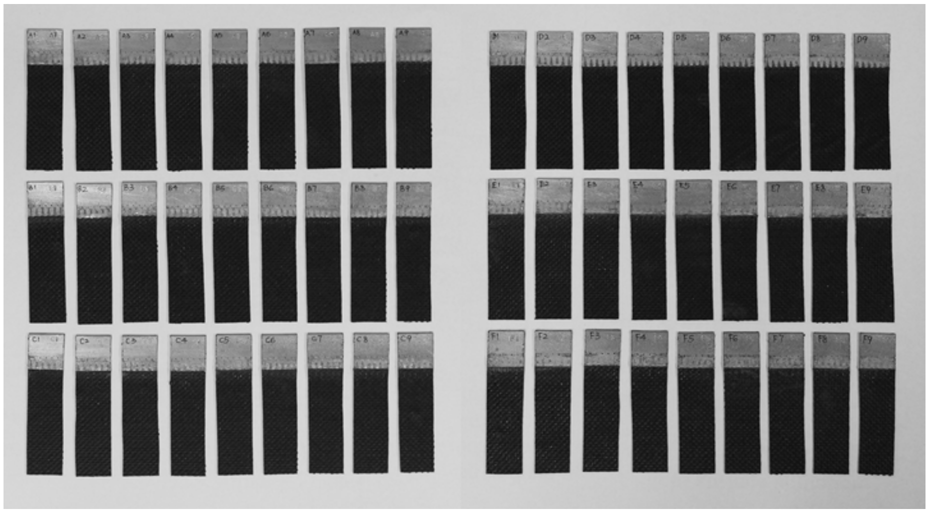

Figure 6.1: 25.4 mm wide samples for corrosion tests.

All 54 samples were sorted into 11 groups as listed in Table 6.1. 10 groups, with five samples for each, were randomly assigned with ten corrosion cycle intervals. Each group ran through a certain number of days of corrosion cycles. Every ten days of the cycling process is equivalent to one year of natural weathering. Another group, including four samples, was e-coated and went through 120 cycles to evaluate the anti-corrosion effectiveness of the e-coat. Within each group, the samples are cut from different locations of different flanges to reduce the effect of sample variability.

Table 6.1: Grouping for corrosion samples

Intervals	Pull-out date	SamplesSamples				
E-coat	N/A	B8	C6	E4	F2	
0	8/7/2017	C2	D4	E6	A7	B9
25	9/1/2017	E1	A2	B4	F6	D8
40	9/16/2017	C1	D3	E5	A6	F8
45	9/21/2017	D1	F3	A4	B6	C8
50	9/26/2017	B1	C3	F5	E7	A8
55	10/1/2017	A1	B3	C5	D7	E9
60	10/6/2017	B2	C4	D6	E8	F9
65	10/11/2017	E2	A3	B5	F7	D9
70	10/16/2017	D2	F4	A5	B7	C9
75	10/21/2017	F1	E3	D5	C7	A9

6.1.2 Perform corrosion cycling

The corrosion cycles are performed by Auto Technology Company. The process details of each cycle are listed in Table 6.2. For the salt spray process, the samples are sprayed with 5% sodium chloride solution. One cycle takes one day to complete, and every ten days are one-year equivalent corrosion for steel. The cyclic corrosion test is complete after 120 days.

Table 6.2: Corrosion cycle process

Testing order	Test item	Test temperature (^oC)	Test duration (hour)
1	Humidity	40	2
2	Salt spray	35	2
3	Dry	60	1
4	Humidity	50	6
5	Dry	60	2
6	Humidity	50	6
7	Dry	60	2
8	Freezing	-20	3

6.1.3 Perform post corrosion testing and sample evaluation

Pictures of samples after 25 and 40 days are shown in Figure 6.2 and Figure 6.3, the aluminum part was severely corroded. The samples pulled out with longer corrosion time were corroded even more seriously. The aluminum is the anode in this galvanic system. In the moist atmosphere with sodium chloride, the aluminum corrodes with the cathodic reaction as oxygen reduction[43]:

$$\mathrm{Al} \longrightarrow \mathrm{Al}_3^+ + 3\,\mathrm{e}^-$$

$$\mathrm{O}_2 + 2\,\mathrm{H}_2\mathrm{O} + 4\,\mathrm{e}^- \longrightarrow 4\,\mathrm{OH}^-$$

The coupling between CFRP and aluminum accelerates the corrosion on the anode. Delamination is observed in the samples, especially in the joint regions. The pitting corrosion in the voids at the interfaces between AA foils results in the delamination. The increased area overlapping between CF tows and the AA matrix in the joint region makes the corrosion more severe. The white powder shown in the post-testing samples is the resultant salt due to the corrosion reactions.

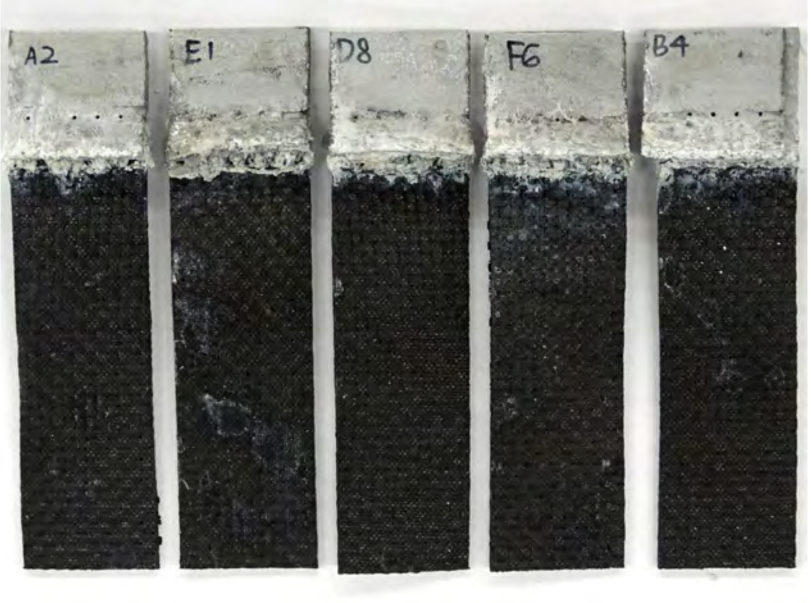

Figure 6.2: Corrosion samples pulled out after 25 cycles.

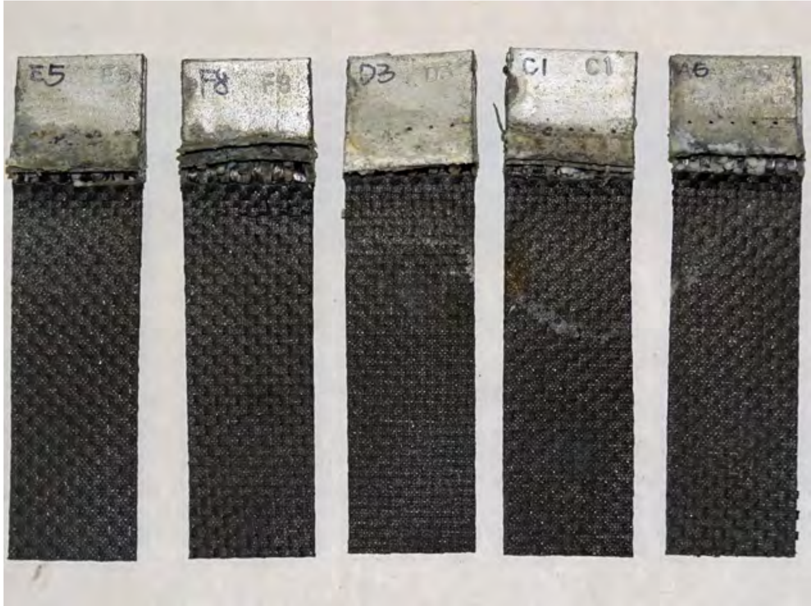

Figure 6.3: Corrosion samples pulled out after 40 cycles.

The e-coated samples were pulled out after 120 cycles. However, the e-coat on the surface cannot prevent galvanic corrosion. The large electrode potential difference and contact area between CF and AA result in a very high galvanic corrosion rate.

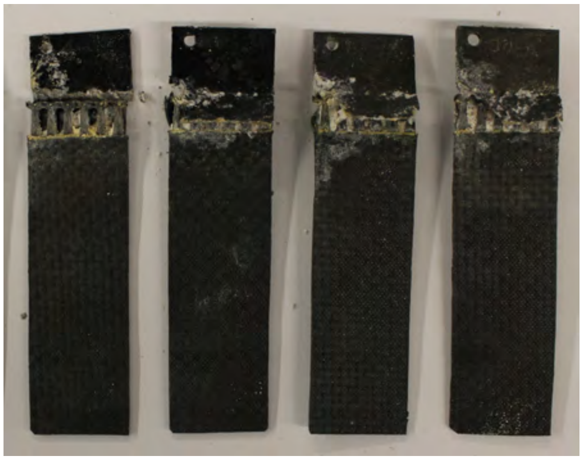

Figure 6.4: E-coated CFRP-AA samples after 120 cycle.

Because all the samples are severely corroded, post corrosion testing cannot be performed on these samples. The aluminum and CFRP combination is a typical galvanic pair expected to result in extensive corrosion damage. To make the sample more resistant to corrosion, non-conductive materials can be used for joining to isolate the CF from the AA. Examples of insulating buffers include materials such as glass and aramid fibers. Designing, building, and testing CFRP-AA joints with anti-corrosion features will be introduced in the following section.

6.2 Mechanical performance of CFRP-KFRP-AA Joint

Various methods have been explored to obtain electrical insulation between the AA and CFRP, including non-conductive fibers and in-channel coatings. The finalized joint design is to embed three layers of Kevlar into 14 layers of AA and cure the joint using West System epoxy. The channel geometries and stacking sequence of the KFRP-AA joint are listed in Table 6.3 and Table 6.4, respectively. The total thickness of the samples is 2 mm. The UAM welding procedure and parameters were the same as those for embedding CF.

Table 6.3: Channel geometries of the final KFRP-AA joint design (unit:mm)

Channel width	Arc radius	Channel spacing	Entry width	Channel depth
1.27	3.05	4.23	2.86	0.23-0.43

Table 6.4: Stacking sequence of the final KFRP-AA joint design.

Description	Total AA layers
Four base AA foil layers are welded	4
Channels are cut and 1st layer of Kevlar tow loops are placed	4
One AA sheet layer is welded over 1st Kevlar layer	5
Three AA foil layers are welded	8
Channels are cut and 2nd layer of Kevlar tow loops are placed	8
One AA sheet layer is welded over 2nd Kevlar layer	9
Three AA foil layers are welded	12
Channels are cut and 3rd layer of Kevlar tow loops are placed	12
One AA sheet layer is welded over 3rd Kevlar layer	13
One AA foil layer is welded	14
Epoxy hole are drilled	14

Table 6.5: Welding parameters of the final KFRP-AA joint design.

	Force (N)	Amplitude (μm)	Speed (in/min)	Dwell time (ms)
Tape	5000	32	200 (85 mm/s)	300 ms
Sheet	4000	30	80 (34 mm/s)	150 ms

Tensile tests

Five KFRP-AA joint samples are welded on one flange and cured using West System epoxy. The samples were then cut from the flange with a width of 32 mm for each sample to prevent damage to the embedded fibers from cutting. Figure 6.5 shows the front and back of samples before tensile tests. The labels correspond to the sample location on the flange from left to right.

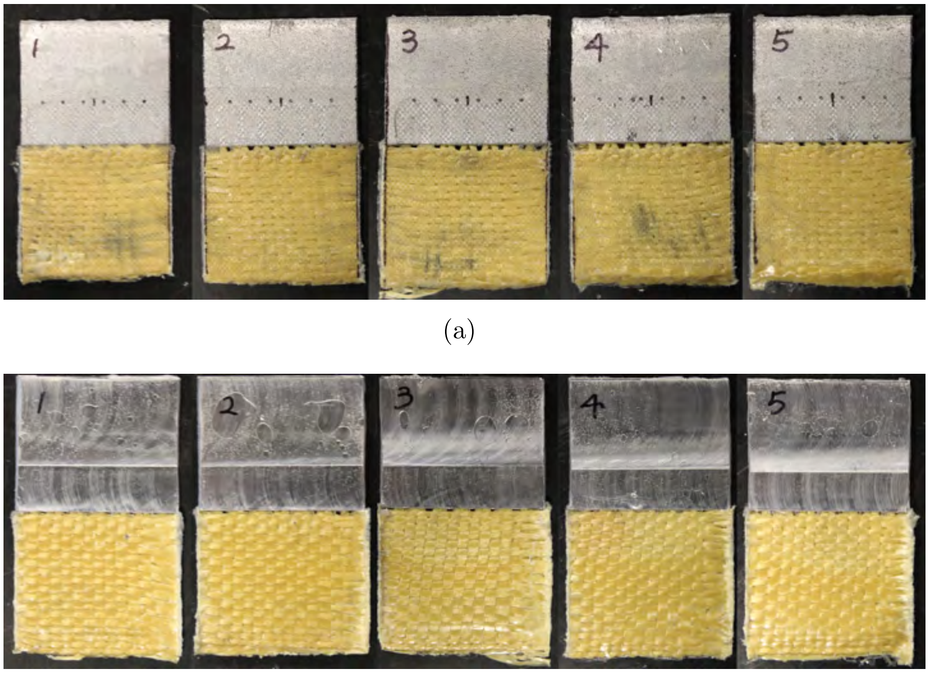

(a)

(b)

Figure 6.5: Pictures of tensile samples before testing. (a) front, (b) back.

All five samples were tested with a strain rate of 1.27 mm/min using the MTS load frame in the SMSL lab. The load vs. displacement curves are plotted in Figure 6.6. Table 6.6 lists the peak loads, energy absorptions, and failure modes of all the samples. From the load vs. displacement plot, a stiffness change is observed when the load is about 800 N, indicating that the epoxy at the KFRP and AA interface is broken, and the embedded KFRP tow loops start to be loaded at that point. All the samples except for sample 3 failed by AA breaking at an average peak load of 4895 N.

Sample 3 is considered defective because tape tearing occurred when welding over the 3rd layer of Kevlar, resulting in a visible crack on the left part of the sample surface. The welding quality is also compromised due to tape tearing, leading to AA delamination of sample 3 during the tensile test. Although the energy absorption of sample 3 is higher than other samples due to fiber pullout after failure, the peak load is the lowest among all the samples.

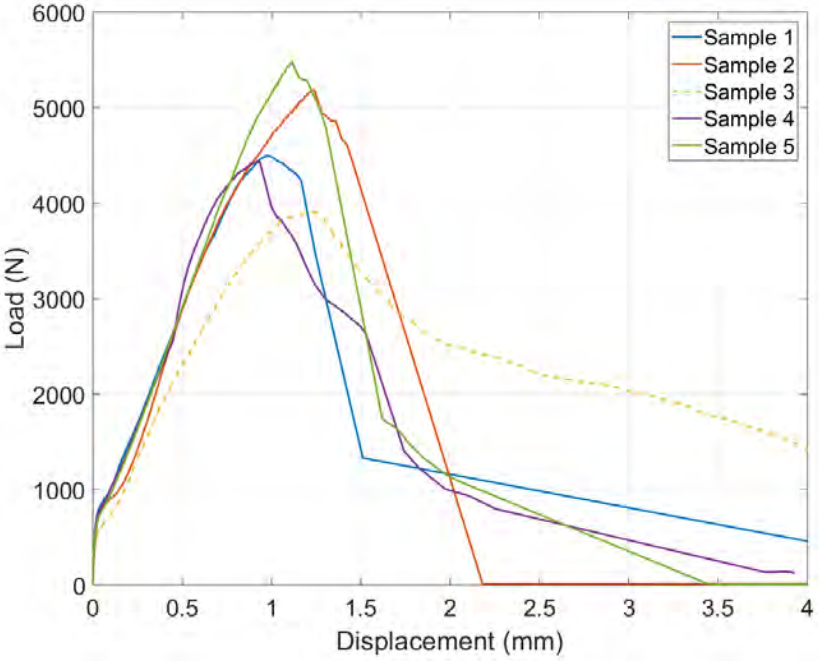

Figure 6.6: Load vs. displacement curves of joint samples during tensile tests.

Table 6.6: Peak loads and energy absorptions of tensile samples

	Peak load (N)	Energy absorption (J)	Failure mode
Sample 1	4488	7.00	AA breaking
Sample 2	5186	6.62	AA delamination and breaking
Sample 3	3897	12.24	AA delamination and KFRP tow breaking
Sample 4	4436	6.23	AA delamination and breaking
Sample 5	5469	6.91	AA breaking
Average (3 excluded)	4895	6.69	N/A

The strain maps shown in Figure 6.7 are obtained using DIC during the tensile test of sample 1. Figure 6.7 (a) shows the strain concentrated at the joint region. With the increasing displacement, the embedded KFRP tows elongate, and the crack between AA and KFRP grows wider. Figure 6.7 (c) shows the AA starting to deform at the top of the channels. The sample failed in the AA at the end of the test. Figure 6.8 is a picture of all samples after testing. Samples 1 and 5 failed by clean AA breaking at the top of channels. Sample 2 failed by delamination at the 3rd layer of Kevlar and AA failure at the top of the channel for the remained 12 layers of AA. Sample 4 failed by delamination at the left part and AA breaking at the right-hand side. The defective sample 3 failed by AA delamination and KFRP tow loops pulling out from the AA matrix. The KFRP tow to the right of sample 3 is pulled from the KFRP part.

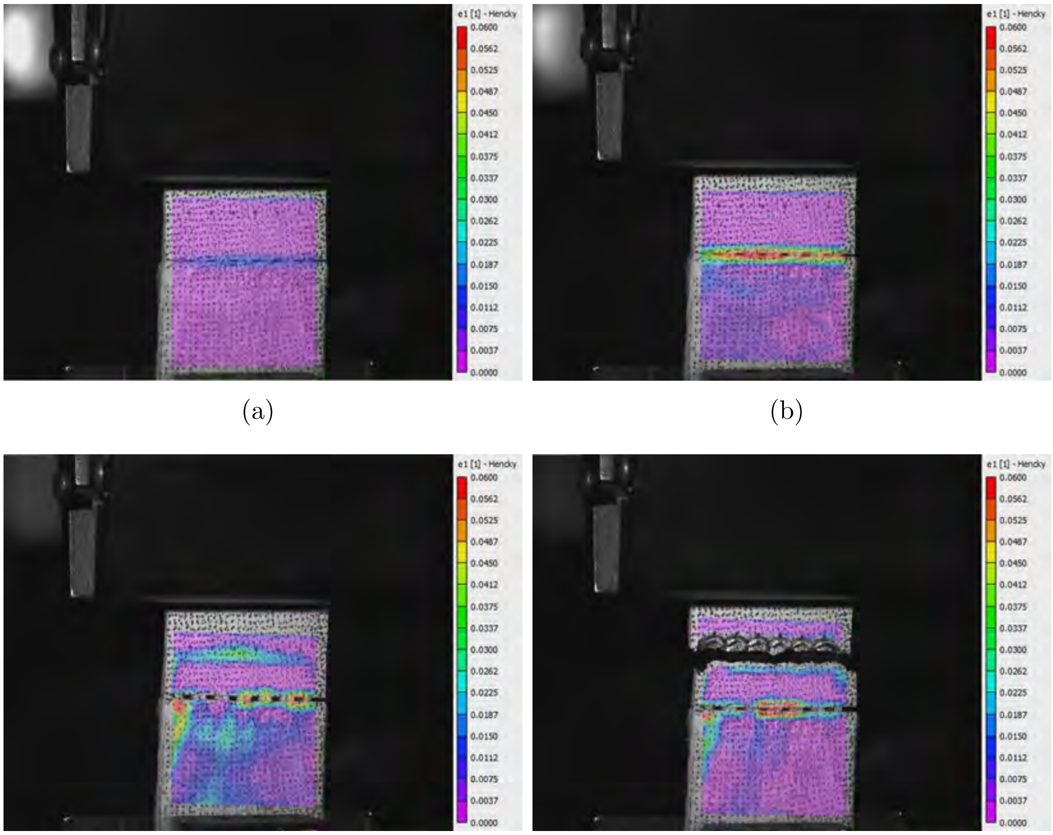

(a) (b)

(c) (d)

Figure 6.7: DIC strain maps of tensile sample 1 during testing.

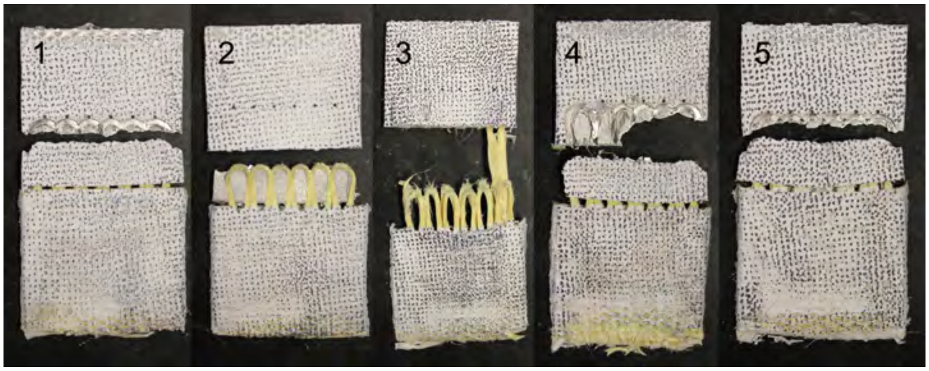

Figure 6.8: Pictures of TSS samples after testing.

Cross-tensile tests

Five cross-tensile samples have been made following the JIS Z 3137 standard, as shown in Figure 6.9. There are ten embedded KFRP loops on each side of the samples for each layer, and they are cured using West System epoxy. The black marks on the KFRPs are caused by the high temperature from laser cutting mounting holes through the samples. However, the strength of the joints is not compromised because the laser cut region is far from the joint. Also, the KFRP is clamped in the fixture and is not loaded during the tests. The samples are tested using the CTS fixture shown in Figure 6.10. The loading rate is 5 mm/min. The DIC system is not used for these tests because the samples are in the fixture, and their deformation cannot be captured by DIC.

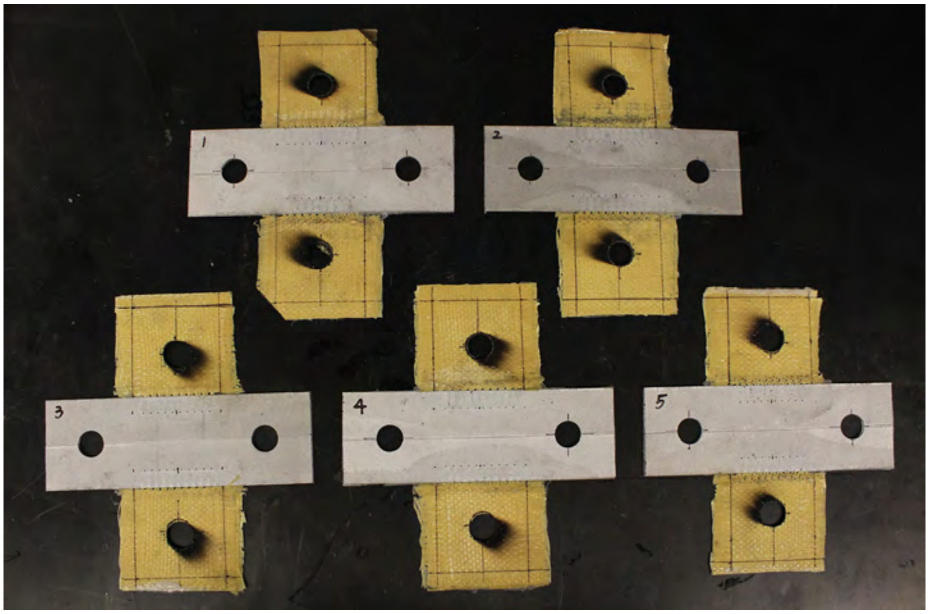

Figure 6.9: Pictures of cross-tensile samples before testing.

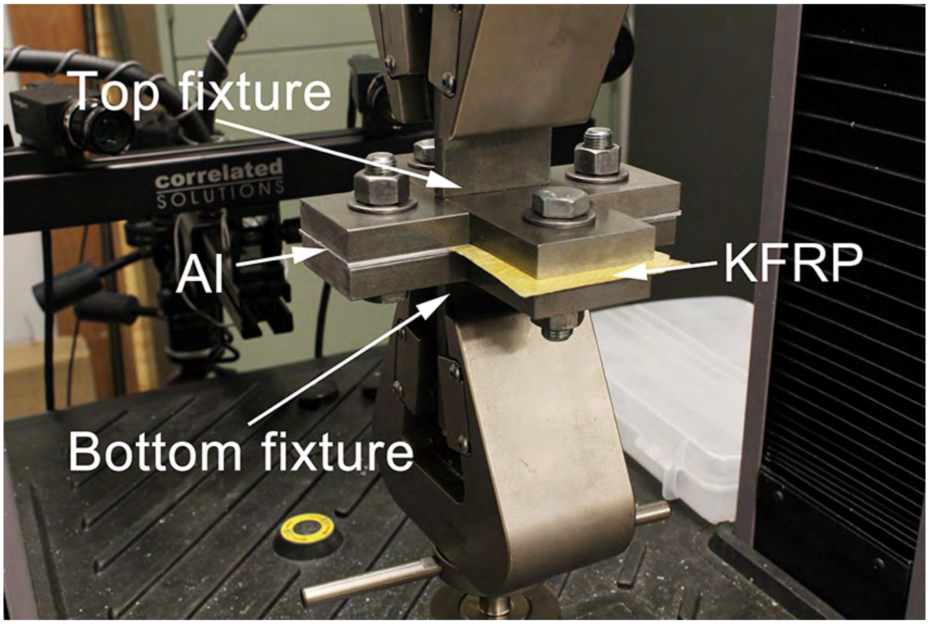

Figure 6.10: Picture of a cross-tensile sample mounted in the fixture that is gripped by two MTS wedge grips in the load frame.

Table 6.7 lists the peak loads of the cross-tensile samples. The average peak load is 3082 N. From the load vs. displacement curves in Figure 6.11, the peak loads correspond to bending along the KFRP-AA interface. After the first peak, there are several subsequent reload and drop processes. The gradual drop indicates that the AA tore along the starting and ending channels. Then, there are two abrupt load drops in each curve, which indicates the AA broke along the top of the channels on two sides of the sample.

Table 6.7: Peak loads of cross-tensile samples

	Peak load (N)
Sample 1	2899
Sample 2	3051
Sample 3	3402
Sample 4	3028
Sample 5	3032
Average	3082

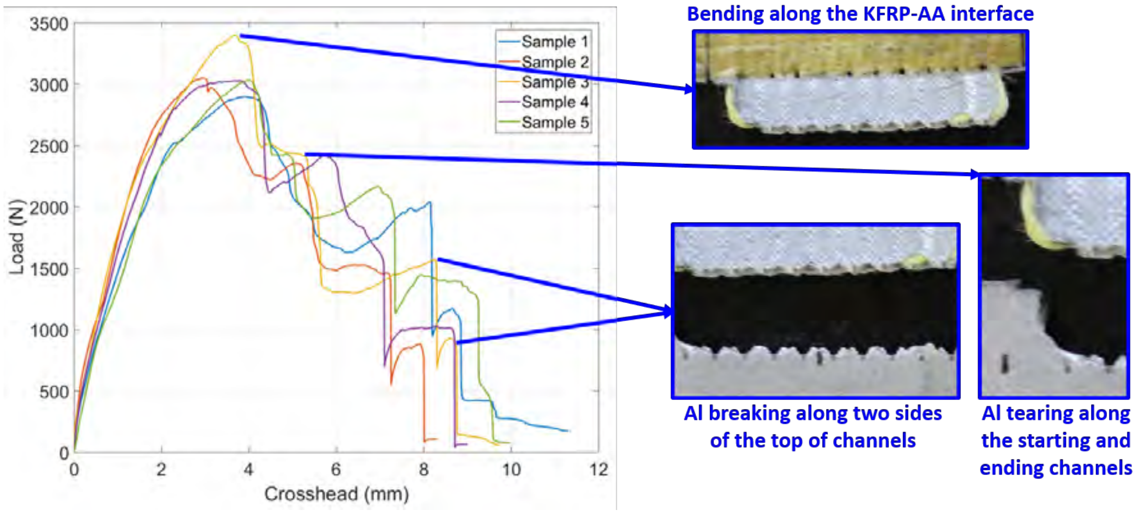

Figure 6.11: Load vs. displacement curves for cross-tensile samples.

Figure 6.12 shows the samples after testing. All the samples failed by aluminum breaking along the loops. AA delaminates only in one loop in sample 1 and one loop in sample 5. No KFRP tow breaking occurred during the tests.

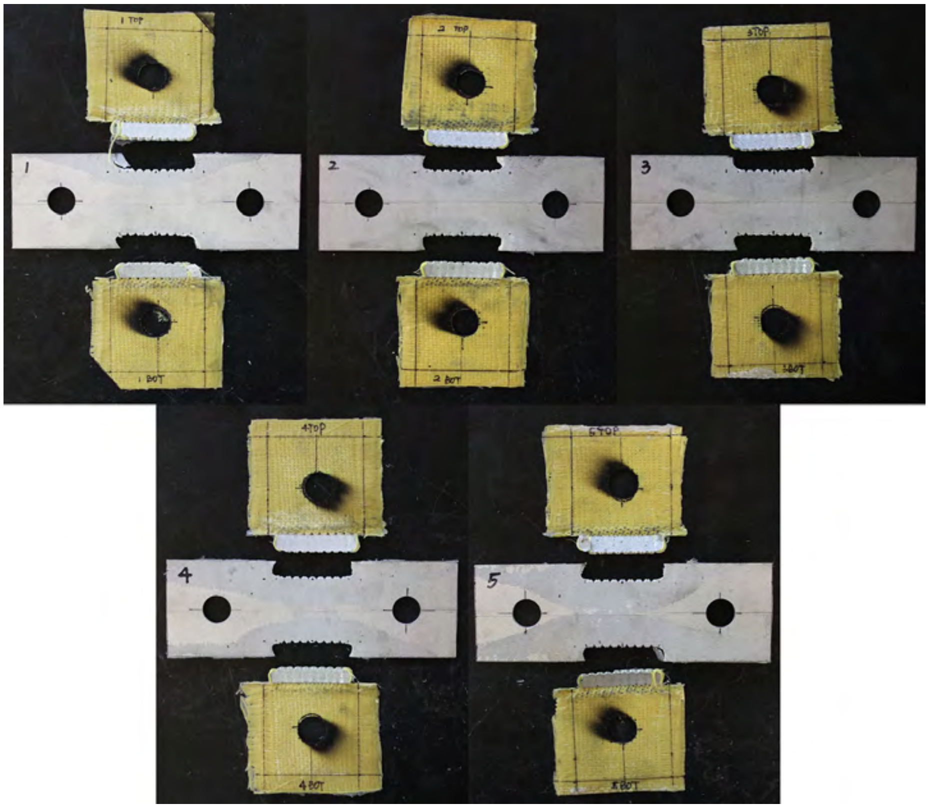

Figure 6.12: Pictures of cross-tensile samples after testing.

Summary

Five KFRP-AA joint samples were made from one flange by embedding three layers of Kevlar into 14 layers of AA. Four of five samples failed in the AA matrix at an average peak load of 4895 N. The average energy absorption is 6.69 J. Due to the difference of mechanical properties and tow thicknesses between Kevlar and CF, the AA:Kevlar ratio needs to be adjusted to obtain failure of the fiber and maximize the energy absorption.

KFRP-AA joint cross-tensile samples have the same stacking sequence as the tensile samples but with Kevlar embedded on both sides of the 50 mm wide AA tab.

Each layer of embedded Kevlar has ten loops on each side. During the cross-tensile tests, all samples failed in the AA matrix at an average peak load of 3082 N.

Thie study proves that Kevlar can be successfully embedded into AA to generate high-strength joints. However, the stacking sequence will be tuned to achieve failure in fiber, instead of AA, in favor of higher energy absorption.

6.3 Galvanic corrosion mitigation of CFRP-KFRP-AA joints

6.3.1 Construct corrosion samples

As investigated in the previous section, Kevlar used as electrical insulation features are able to achieve high mechanical strength. Therefore, this feature is employed in this corrosion cyclic study. Six 356 mm long flanges are manufactured using UAM by embedding two layers of Kevlar in 12 layers of AA to achieve fiber failure in tensile tests. Since the embedded Kevlar loops are made by folding the fabric, there are already four layers of Kevlar fabrics in the joint after embedding two layers of loops. All the flanges are laid up by adding two more fabric layers and curing using West System epoxy to match the thickness of the composite with AA. Each flange is then cut into 12 samples with a 25.4 mm width. Three layup configurations are used. The first one is the finalized design to insulate AA and CF. The hybrid fabric layer added to both sides of the embedded fabrics is made by stitching CF and Kevlar together using Kevlar threads. A picture and schematic of this design are shown in Figure 6.13. The sample has a insulation buffer between AA and CFRP with an exposed width of 1 cm. These samples will be referred to as a “buffer” sample. Samples with two other configurations do not have an insulation buffer. They are made for comparison to investigate the impact of the insulation buffer. Figure 6.14 includes pictures and schematics of samples with these other two configurations. These two samples are referred to as a “CF-outside” sample and a “CF-inside” sample.

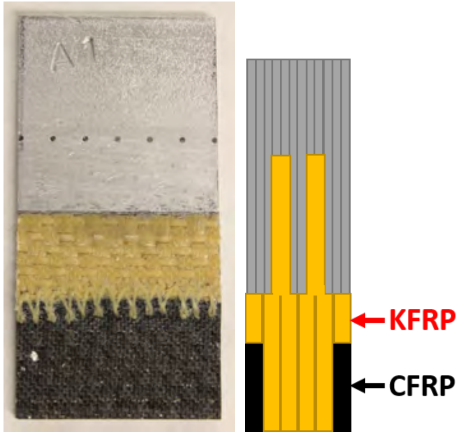

(a) (b)

Figure 6.13: Picture and schematic of a buffer sample. (Schematic not drawn to scale)

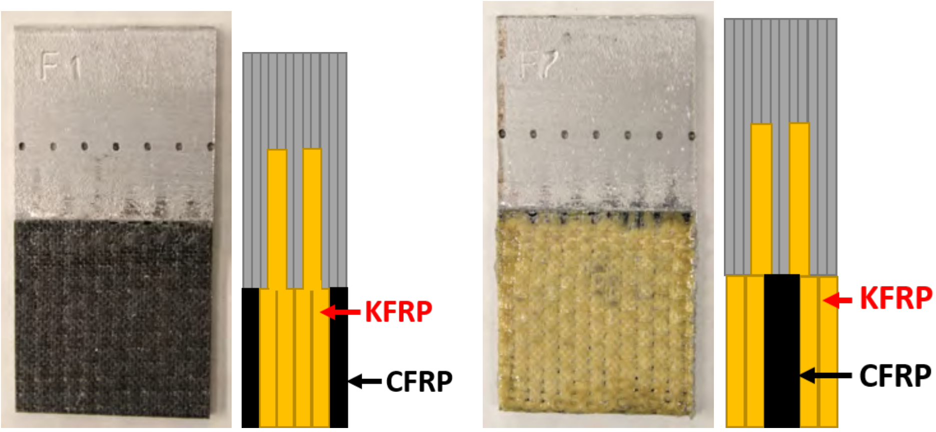

(a) (b) (c) (d)

Figure 6.14: Pictures and schematics of a CF-outside sample and a CF-inside sample. (Schematics not drawn to scale)

Figure 6.15 shows all 72 samples for corrosion cycling tests. Among all the samples, 60 are buffer samples, 6 are CF-inside samples, and 6 are CF-outside samples. The samples are divided into 14 groups according to the tables in Figure 6.16. The assignment follows a pattern such that each group includes one sample from each flange and each welding location. For the 12 groups of buffer samples, each group has five samples. Ten groups are randomly assigned to different numbers of corrosion cycles. The other two groups are e-coated and go through 0 and 120 corrosion cycles. For the CF-outside and CF-inside samples, they all go through the whole 120 cycles.

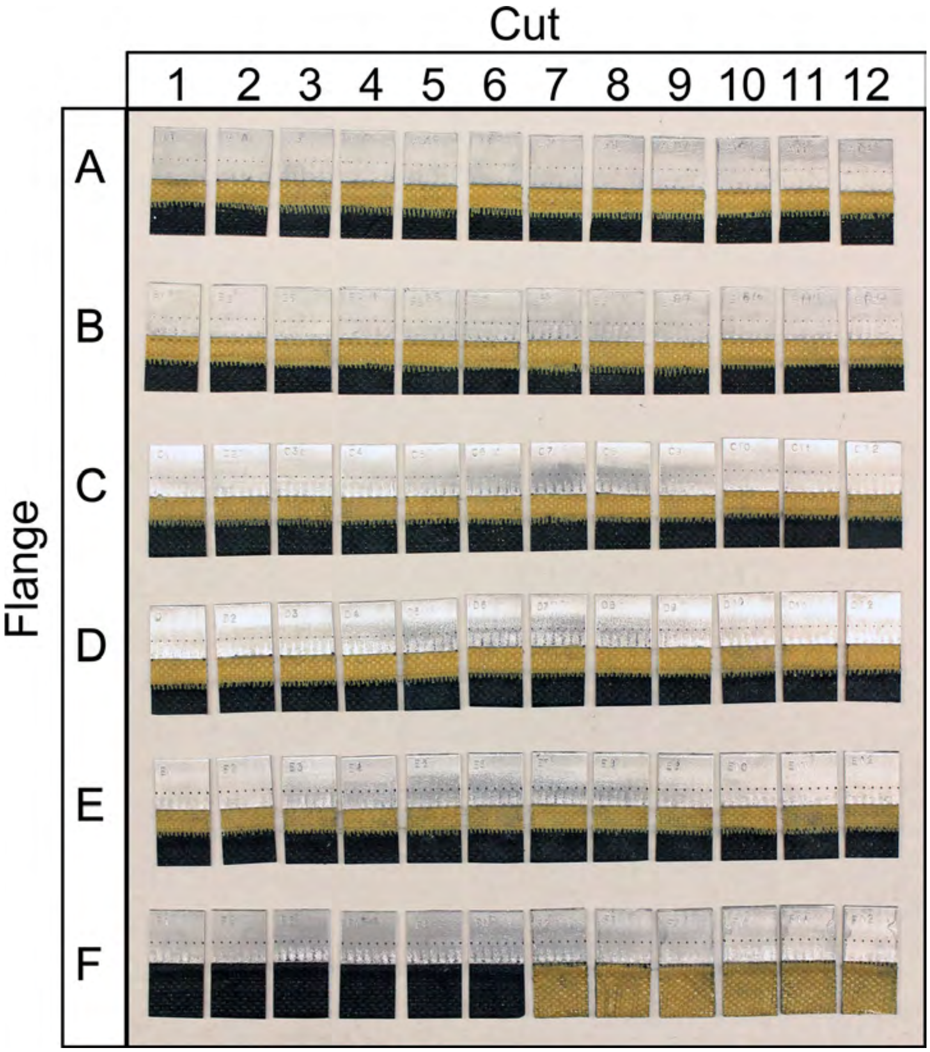
Cut
1
2
3
4
5
6
7
8
9
10
11
12
Flange
A
B
C
D
E
F

Figure 6.15: Picture of all CCT samples.

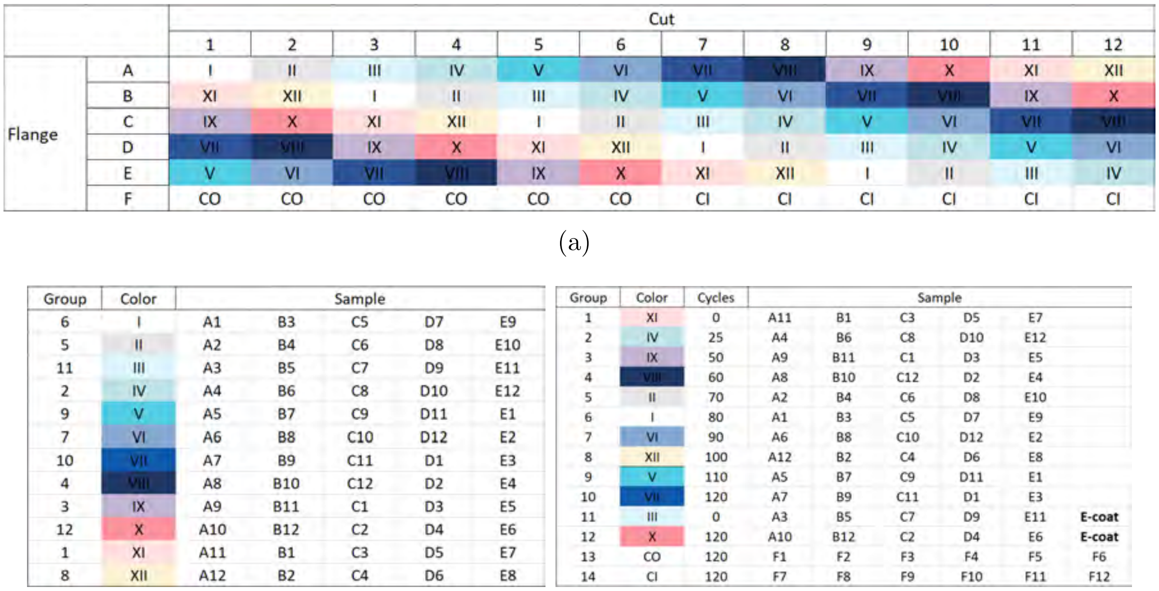

		Cut											
		1	2	3	4	5	6	7	8	9	10	11	12
Flange	A	I	II	III	IV	V	VI	VII	VIII	IX	X	XI	XII
	B	XI	XII	I	II	III	IV	V	VI	VII	VIII	IX	X
	C	IX	X	XI	XII	I	II	III	IV	V	VI	VII	VIII
	D	VII	VIII	IX	X	XI	XII	I	II	III	IV	V	VI
	E	V	VI	VII	VIII	IX	X	XI	XII	I	II	III	IV
	F	CO	CO	CO	CO	CO	CO	CI	CI	CI	CI	CI	CI

(a)

Group	Color	Sample				
6	I	A1	B3	C5	D7	E9
5	II	A2	B4	C6	D8	E10
11	III	A3	B5	C7	D9	E11
2	IV	A4	B6	C8	D10	E12
9	V	A5	B7	C9	D11	E1
7	VI	A6	B8	C10	D12	E2
10	VII	A7	B9	C11	D1	E3
4	VIII	A8	B10	C12	D2	E4
3	IX	A9	B11	C1	D3	E5
12	X	A10	B12	C2	D4	E6
1	XI	A11	B1	C3	D5	E7
8	XII	A12	B2	C4	D6	E8

(b)

Group	Color	Cycles	Sample					
1	XI	0	A11	B1	C3	D5	E7	
2	IV	25	A4	B6	C8	D10	E12	
3	IX	50	A9	B11	C1	D3	E5	
4	VIII	60	A8	B10	C12	D2	E4	
5	II	70	A2	B4	C6	D8	E10	
6	I	80	A1	B3	C5	D7	E9	
7	VI	90	A6	B8	C10	D12	E2	
8	XII	100	A12	B2	C4	D6	E8	
9	V	110	A5	B7	C9	D11	E1	
10	VII	120	A7	B9	C11	D1	E3	
11	III	0	A3	B5	C7	D9	E11	**E-coat**
12	X	120	A10	B12	C2	D4	E6	**E-coat**
13	CO	120	F1	F2	F3	F4	F5	F6
14	CI	120	F7	F8	F9	F10	F11	F12

(c)

Figure 6.16: Grouping of CCT samples. I-XII are groups for buffer samples. CI and CO indicates CF-inside and CF-outside samples, respectively. (a) 60 buffer samples from flanges A-E are assigned to 12 colors, 6 CF-inside and 6 CF-outside samples are made from flange F; (b) 12 colors for buffer samples are randomly assigned to 12 groups; (c) group numbers with the corresponding color, number of corrosion cycles and sample labels.

6.3.2 Resistance measurements

The resistance of the joint is considered as a measure of galvanic corrosion risk. The resistivity target that should mitigate galvanic corrosion is 10^8 $\Omega \cdot$ m. The resistance of the joint can be calculated based on the resistivity and dimensions using the equation R=ρ·L/A , where ρ is resistivity, L is the length, and A is the cross-sectional area. Assuming the joint dimensions are 5.08×2.54×0.18 mm, then the target resistance of the joint is 55.6 GΩ.

For the CF-outside and CF-inside samples, the resistance is measured using a FLUKE multimeter, and the results are listed in Table 6.8. The values vary because the amount of epoxy between the CFRP and AA is different for the samples. However, the values do not pass the spec discussed above.

Table 6.8: Resistances of CF-outside and CF-inside samples (unit:Ω)

	F1	F2	F3	F4	F5	F6
CF-outside	132	112	217	789	633	324
	F7	F8	F9	F10	F11	F12
CF-inside	342	75	958	112	187	188

For the buffer samples, the resistances are measured as overload using a 200 GΩ range device. Therefore, the resistance of buffer samples passes the 55.6 GΩ targets. Since the equipment on hand or that can be purchased at a reasonable price does not have a higher resistance measure range, the resistance of the buffer samples is difficult to measure. To get an estimate of the value, a simplified circuit diagram is drawn in Figure 6.17. The volume resistivity of KFRP and CFRP are $5\times 10^{15}\ \Omega \cdot$ cm and $2\times 10^{2}\ \Omega \cdot$ cm [25]. The resistance of each resistor is calculated based on the corresponding resistivity and material dimensions. The resistance of the whole system is dominated by the KFRP resistor, which is 1.17×10^{9} GΩ. Therefore, the estimated resistance is eight orders of magnitude higher than the spec. Theoretically, the buffer samples should be able to avoid galvanic corrosion and pass the CCT spec.

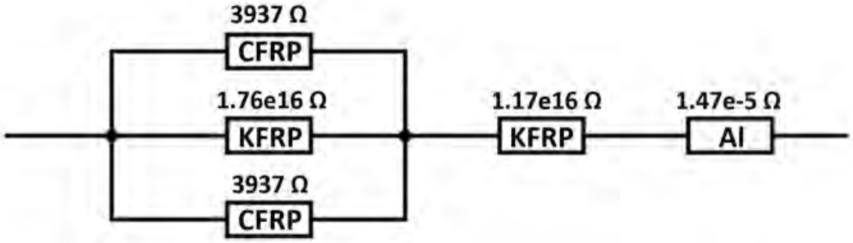

Figure 6.17: Circuit diagram of a buffer sample.

6.3.3 Perform post corrosion testing and sample evaluation

Appearance

The corrosion cycles of this study are the same as Section 6.1.2. After the corrosion cycling process, all samples were evaluated in terms of the corrosion product on the surface. For the uncoated buffer samples, groups 6 to 10 (80, 90, 100, 110, and 120 cycles) show evidence of slight galvanic corrosion at the buffer-AA interface. No severe corrosion or AA delamination occurred in these samples, although some pitting corrosion was observed in the AA. For the e-coated buffer samples, there was no corrosion product on the samples of group 12 after 120 cycles. On the contrary, there was a large amount of corrosion product on the samples of groups 13 (uncoated CF-outside) and 14 (uncoated CF-inside). The connection between AA and CF leads to severe galvanic corrosion, producing the corrosion product and resulting in AA delamination. Therefore, the KFRP insulation buffer is critical to prevent galvanic corrosion.

Based on the appearance evaluation, the buffer design can effectively insulate the CF from AA. With the e-coat, the galvanic corrosion and pitting corrosion in AA are successfully avoided after 120 corrosion cycles.

Group 1 - 0 cycle buffer samples

Figure 6.18 shows the uncoated buffer samples with no corrosion cycle (0 cycles).

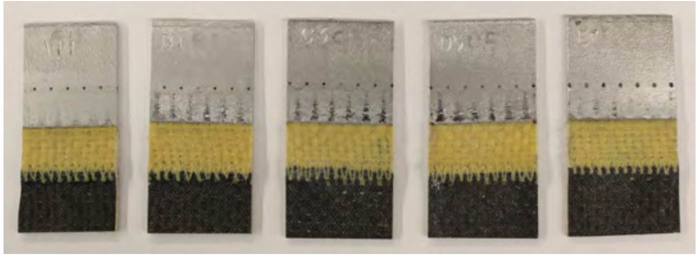

Figure 6.18: Group 1: uncoated buffer samples after 0 cycles. Sample sequence: A11, B1, C3, D5, E7.

Group 2 - 25 cycles uncoated buffer samples

For the samples after 25 corrosion cycles, shown in Figure 6.19, the AA surface is not as shiny as that of group 1 samples. However, there is no evidence of corrosion.

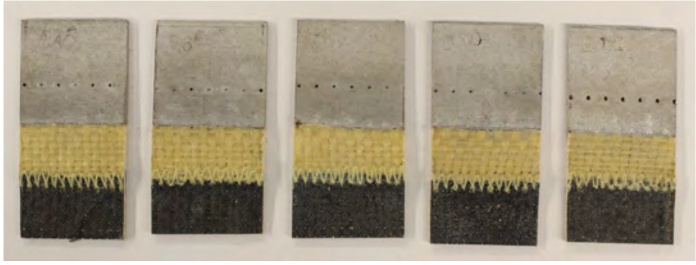

Figure 6.19: Group 2: uncoated buffer samples after 25 cycles. Sample sequence: A4, B6, C8, D10, E12.

Group 3 - 50 cycles uncoated buffer samples

After 50 cycles, there is no visual evidence of corrosion of the samples.

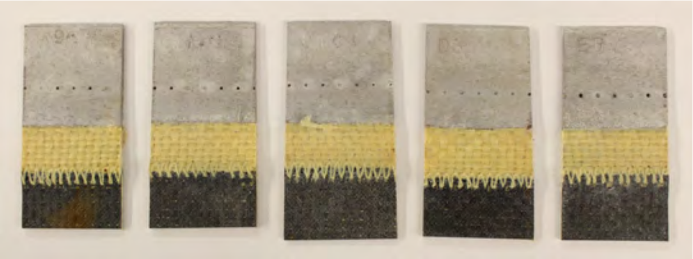

Figure 6.20: Group 3: uncoated buffer samples after 50 cycles. Sample sequence: A9, B11, C1, D3, E5.

Group 4 - 60 cycles uncoated buffer samples

After 60 cycles, there is still no visual evidence of corrosion of the samples.

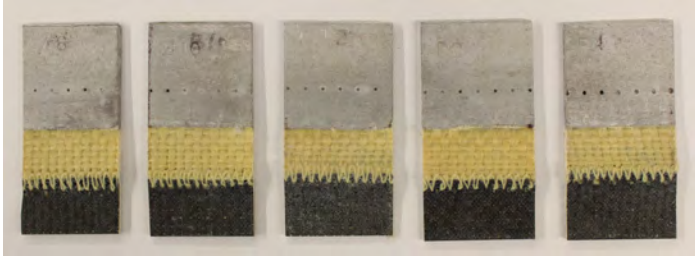

Figure 6.21: Group 4: uncoated buffer samples after 60 cycles. Sample sequence: A8, B10, C12, D2, E4.

Group 5 - 70 cycles uncoated buffer samples

Figure 6.22 shows the group 5 samples after 70 corrosion cycles. The discoloration indicates that very slight galvanic corrosion occurred to sample A2. The other 4 samples do not show any visual evidence of corrosion.

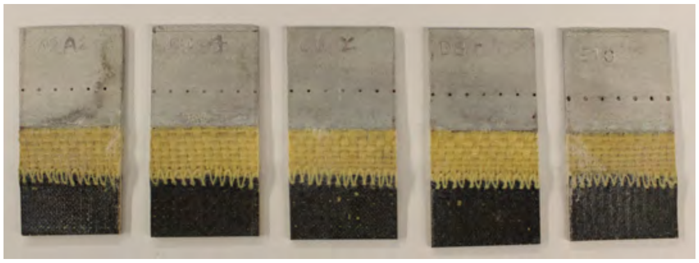

Figure 6.22: Group 5: uncoated buffer samples after 70 cycles. Sample sequence: A2, B4, C6, D8, E10.

Group 6 - 80 cycles uncoated buffer samples

For the samples of group 6, as shown in Figure 6.23, some discoloration is observed on all of the samples, which is evidence of very slight galvanic corrosion. Sample C5 is only corroded on the left edge of the AA-KFRP interface. The other 4 samples have more corrosion, but it only occurs on the surface. No delamination is observed.

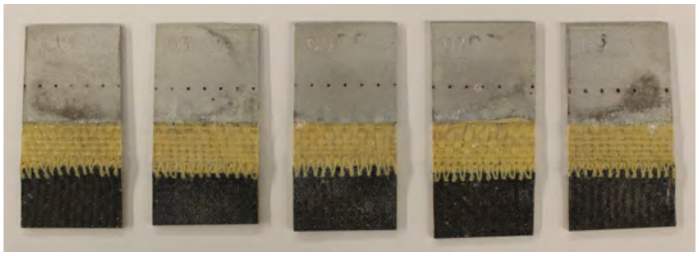

Figure 6.23: Group 6: uncoated buffer samples after 80 cycles. Sample sequence: A1, B3, C5, D7, E9.

Group 7 - 90 cycles uncoated buffer samples

As shown in Figure 6.24, some corrosion product is observed on samples A3, B8, C10, and D12. The corrosion occurred at the joint region and produced some salt on the samples. For samples C10 and D12, there was initially a small crack on the surface due to tape tearing when welding the last layer for each sample. During the corrosion cycles, the sodium chloride solution is trapped in the cracks and accelerates the local corrosion. As for sample E2, there is no corrosion after 90 cycles.

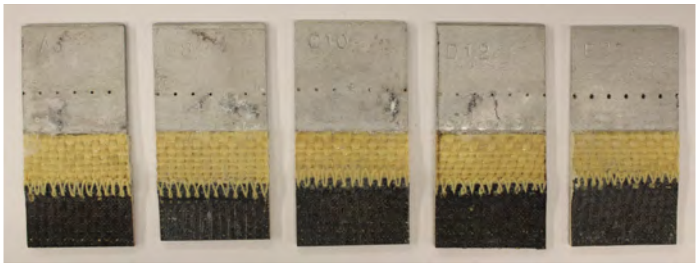

Figure 6.24: Group 7: uncoated buffer samples after 90 cycles. Sample sequence: A6, B8, C10, D12, E2.

Group 8 - 100 cycles uncoated buffer samples

For the samples of group 8 that went through 100 cycles, shown in Figure 6.25, there is no visual evidence of corrosion of the samples.

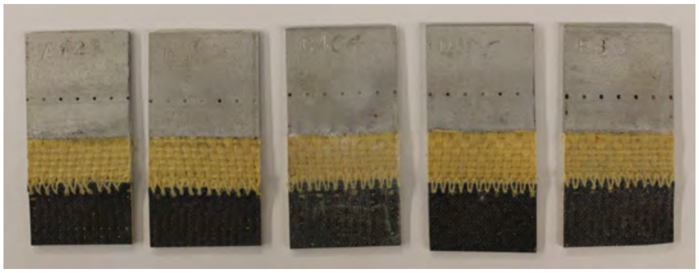

Figure 6.25: Group 8: uncoated buffer samples after 100 cycles. Sample sequence: A12, B2, C4, D6, E8.

Group 9 - 110 cycles uncoated buffer samples

After 110 cycles, sample B7, D11, and E1 have some discoloration on their surfaces, as shown in Figure 6.26. However, no corrosion salt is observed. No corrosion is visible on samples A5 and C9.

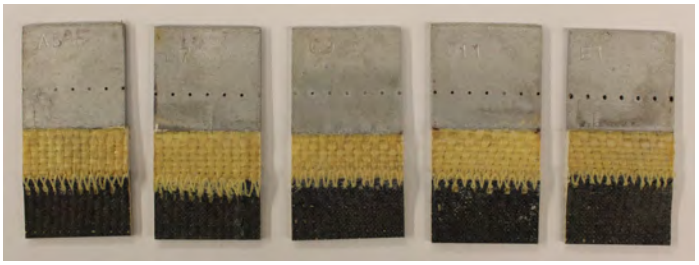

Figure 6.26: Group 9: uncoated buffer samples after 110 cycles. Sample sequence: A5, B7, C9, D11, E1.

Group 10 - 120 cycles uncoated buffer samples

For the samples of group 10 after 120 cycles, only sample B9 has some discoloration and salt on its surface. The other samples do not show any visible evidence of corrosion.

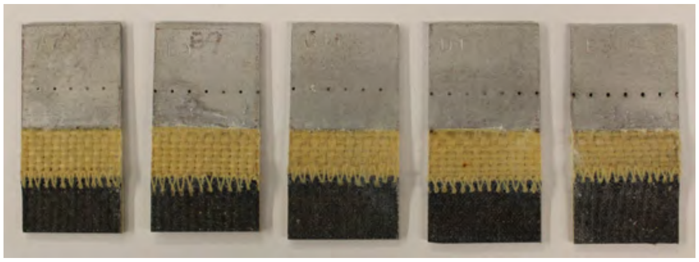

Figure 6.27: Group 10: uncoated buffer samples after 120 cycles. Sample sequence: A7, B9, C11, D1, E3.

Group 11 - 0 cycle e-coated buffer samples

Figure 6.28 shows e-coated buffer samples without any corrosion cycles. The light spots on the AA tab close to the KFRP was some epoxy residual from the KFRP-CFRP layup process. The non-conductive epoxy cannot be e-coated, and results in the light spots.

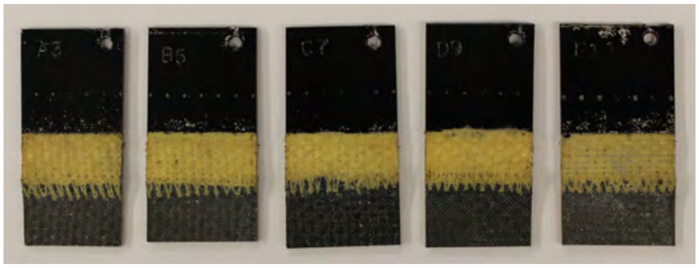

Figure 6.28: Group 11: e-coated buffer samples after 0 cycles. Sample sequence: A3, B5, C7, D9, E11.

Group 12 - 120 cycles e-coated buffer samples

Figure 6.29 shows e-coated buffer samples after 120 corrosion cycles. There is no visible evidence of corrosion on any of the samples.

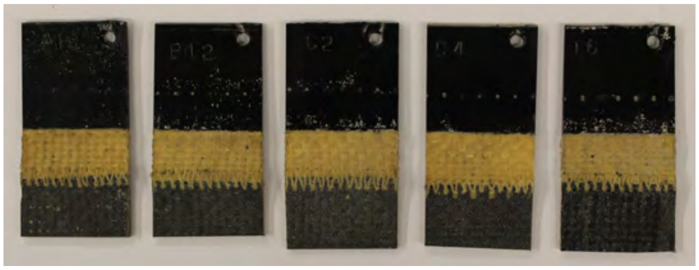

Figure 6.29: Group 12: e-coated buffer samples after 120 cycles. Sample sequence: A10, B12, C2, D4, E6.

Group 13 - 120 cycles uncoated CF-outside samples

For all the samples of group 13, severe galvanic corrosion occurred which produced salts on the surfaces, as shown in Figure 6.30. Also, the AA delaminates due to corrosion. Comparing to the buffer samples of group 10, the CF-outside samples have no KFRP buffer and the CFRP is in contact with the AA. Therefore, the large electrode potential difference between AA and CF results in significant galvanic corrosion.

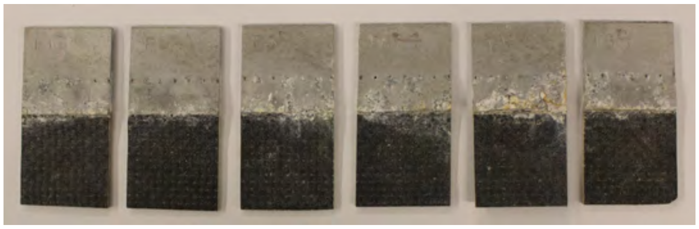

Figure 6.30: Group 13: uncoated CF-outside samples after 120 cycles.

Group 14 - 120 cycles uncoated CF-inside samples

For the CF-inside samples shown in Figure 6.31, the scenario is similar to the CF-outside samples, but not as severe. There is salt on the surfaces of all the samples. The AA delamination that occurred in CF-inside samples is not as bad as for the CF-outside samples. When the CF layers are inserted between the Kevlar layers, the direct ionic connection between CF and AA through the salt solution on the outside is largely reduced. However, this cannot completely prevent galvanic corrosion because any slight crack on the outside Kevlar or the epoxy will result in CF-AA connection.

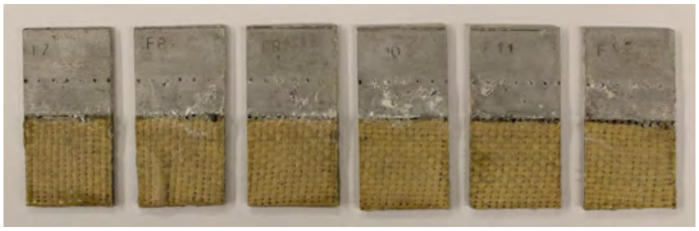

Figure 6.31: Group 14: uncoated CF-inside samples after 120 cycles.

Mass loss

After the corrosion cycles, the surfaces of all the KFRP-AA samples (including buffer, CF-outside, and CF-inside samples) were scraped using a razor blade to remove the corrosion product. Next, a chemical cleaning method was applied to the samples following the procedure in ASTM G1-03. The steps are described as follows:

1. Use 50 ml phosphoric acid and 20 g chromium trioxide, add reagent water to make 1000 ml of solution. Heat the solution to 90^oC. Immerse the samples in the solution for 10 minutes.

2. Immerse the samples to nitric acid for 5 minutes at room temperature.

After cleaning the samples, they were weighed, and the masses were recorded in Table A.2 and Table A.3 in the appendix. The average masses and mass losses were listed in Table 6.9. The mass loss percentages were also plotted in Figure 6.32. The average mass loss of uncoated buffer samples after 120 cycles is only 0.5%. When the buffer samples are e-coated, the mass remains unchanged after 120 corrosion cycles. For the uncoated CF-outside samples, the average mass loss is 3.2%, more than seven times that of the uncoated buffer samples. As for the uncoated CF-inside samples, the mass losses are not as high as CF-outside samples, but the CF-inside samples still lose mass at 1.7%.

From the mass loss evaluation, the uncoated CF-outside and CF-inside designs are not usable for corrosion mitigation. The uncoated buffer samples mitigate galvanic corrosion. With e-coat, the buffer design can completely avoid galvanic corrosion after 120 cycles.

Table 6.9: Average masses and mass losses of samples before and after the CCT process (unit:g)

($\overline{m_1}$: mass before CCT; $\overline{m_2}$: mass after CCT; $\overline{\Delta m}$: $\overline{m_1}$-$\overline{m_2}$)

Group	Cycles	Design	$\overline{m_1}$	$\overline{m_2}$	$\overline{\Delta m}$	$\overline{\Delta m/m_1}(\%)$
1	0	Uncoated buffer	4.618	4.614	0.004	0.083
2	25	Uncoated buffer	4.644	4.642	0.002	0.043
3	50	Uncoated buffer	4.670	4.652	0.018	0.384
4	60	Uncoated buffer	4.604	4.596	0.008	0.172
5	70	Uncoated buffer	4.718	4.694	0.024	0.504
6	80	Uncoated buffer	4.702	4.686	0.016	0.334
7	90	Uncoated buffer	4.634	4.630	0.004	0.087
8	100	Uncoated buffer	4.716	4.704	0.012	0.259
9	110	Uncoated buffer	4.642	4.630	0.012	0.260
10	120	Uncoated buffer	4.648	4.626	0.022	0.468
11	0	E-coated buffer	4.642	4.642	0	0
12	120	E-coated buffer	4.686	4.686	0	0
13	120	Uncoated CF-outside	4.533	4.388	0.145	3.199
14	120	Uncoated CF-inside	4.632	4.555	0.077	1.657

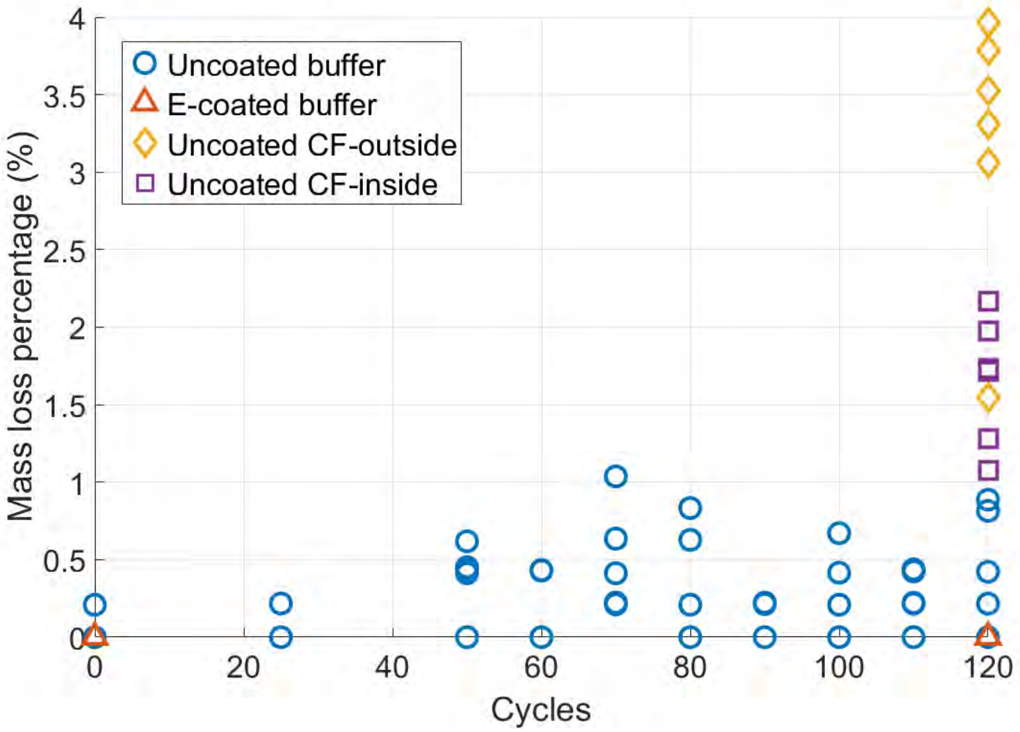

Figure 6.32: Masses of CCT samples before and after corrosion cycles.

Tensile strength

Tensile tests are performed on the CCT samples, and the peak loads of each sample are listed in the appendix and plotted in Figure 6.33. The average peak loads and the standard deviations are listed in Table 6.10. For the uncoated buffer samples, the peak load maintained 97% of the original load after 120 corrosion cycles. For the e-coated buffer samples, they also maintained 95% of the strength. The red dashed line represents the HES spec, a target provided by Honda based on the industry requirement for RSW between materials with strength and dimensions equivalent to those in this study. The blue horizontal line represents a commonly used CCT spec, which is to maintain 90% strength after 120 cycles. The average peak loads of all the buffer groups exceed both the HES spec and CCT spec.

For the uncoated CF-outside and CF-inside samples, they can also compare to the 0 cycle uncoated buffer samples because the joints are the same. After 120 cycles, the strengths of uncoated CF-outside samples and uncoated CF-inside samples dropped by 34% and 22%, respectively. This indicates that these two designs do not effectively mitigate galvanic corrosion.

Table 6.10: Average and standard deviation of peak loads of samples after CCT process (unit:N)

Group	Cycles	Design	Average	Standard deviation
1	0	Uncoated buffer	3664	53.6
2	25	Uncoated buffer	3770	244.7
3	50	Uncoated buffer	3721	132.9
4	60	Uncoated buffer	3507	260.4
5	70	Uncoated buffer	3849	500.2
6	80	Uncoated buffer	3746	403.1
7	90	Uncoated buffer	3487	489.0
8	100	Uncoated buffer	3756	411.2
9	110	Uncoated buffer	3545	411.9
10	120	Uncoated buffer	3538	356.2
11	0	E-coated buffer	3863	209.5
12	120	E-coated buffer	3688	394.1
13	120	Uncoated CF-outside	2416	685.2
14	120	Uncoated CF-inside	2865	410.5

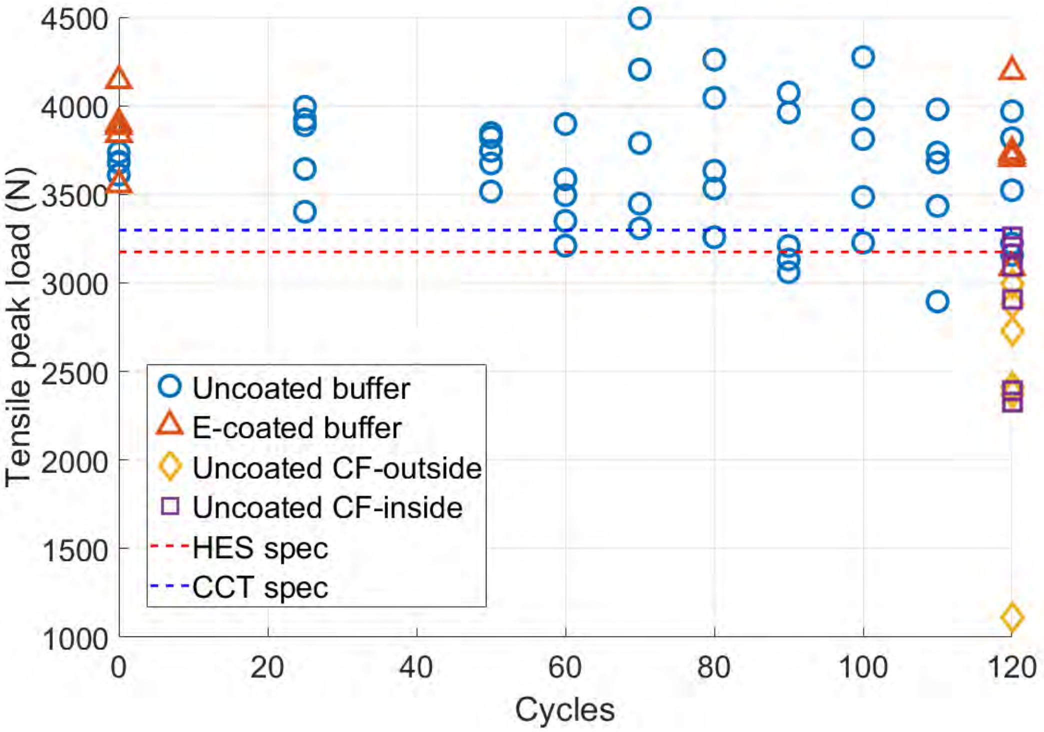

Figure 6.33: Tensile peak loads vs. number of corrosion cycles.

For the uncoated CF-outside samples, they are severely corroded after 120 cycles. A large amount of AA is corroded, and the strength of the AA decreased compared to the 0 cycles strength. The joint structure is damaged, and the failure mode is a mixture of KFRP breaking, AA delamination, and AA breaking. The uncoated CF-inside samples are not damaged as severely, with the failure mode mainly being KFRP tow breaking. In addition to KFRP failure, the AA also delaminates, and there are several AA columns pulled out from the AA tab by the KFRP tows. These two designs do not exhibit an ideal failure mode, and the strength is primarily reduced by corrosion.

Figure 6.34 shows the samples after tensile tests. For buffer samples with and without e-coat, only sample C4 after 100 cycles failed by AA breaking. All the other buffer samples failed by KFRP tow breaking with no AA failure. These samples have only two layers of Kevlar embedded, which is different from the 3-layer samples tested in Section 6.2. Therefore, KFRP tow breaking is the ideal and expected failure mode. The failure mode is not affected by corrosion.

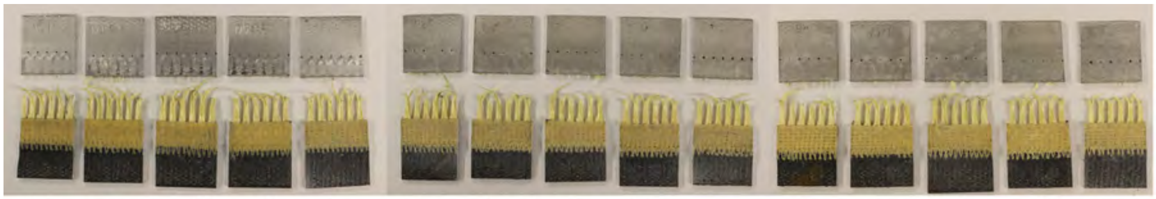

Uncoated buffer - 0 cycle Uncoated buffer - 25 cycles Uncoated buffer - 50 cycles

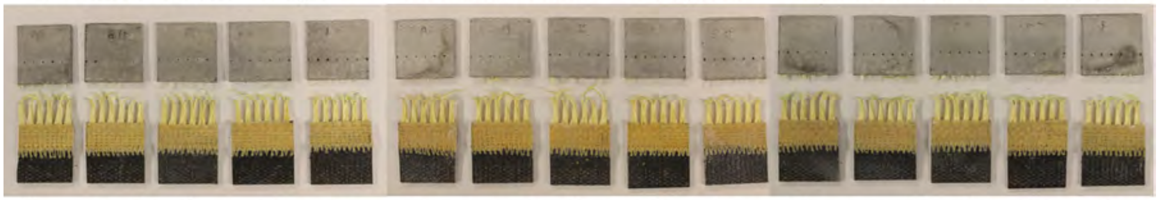

Uncoated buffer - 60 cycles Uncoated buffer - 70 cycles Uncoated buffer - 80 cycles

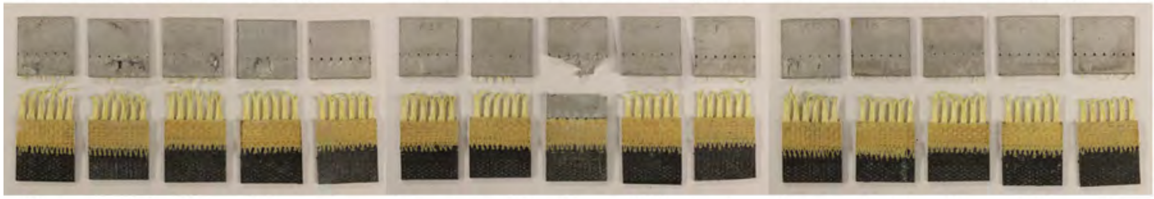

Uncoated buffer - 90 cycles Uncoated buffer - 100 cycles Uncoated buffer - 110 cycles

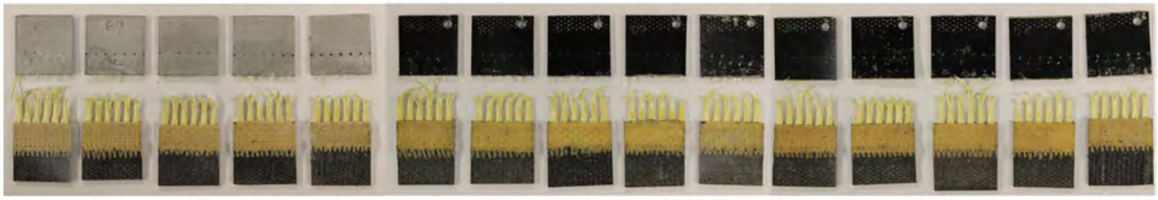

Uncoated buffer - 120 cycles E-coated buffer - 0 cycle E-coated buffer - 120 cycles

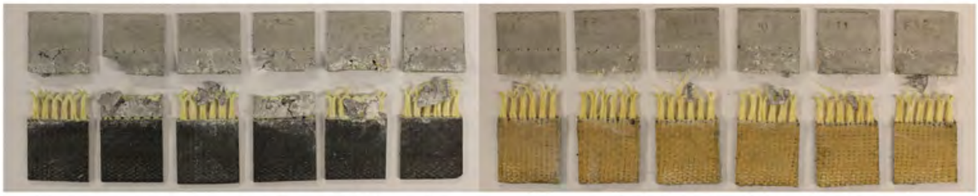

Uncoated CF-outside - 120 cycle Uncoated CF-inside - 120 cycle

Figure 6.34: CCT samples after tensile tests.

6.4 Summary

To investigate the effect of galvanic corrosion on the CFRP-AA UAM joint, initial CCT tests were performed on CFRP-AA joints, with and without E-coat. The samples were all severely corroded after 25 cycles. The E-coated samples did not survive 120 cycles either. This result shows that a countermeasure is required for the CFRP-AA joints to prevent catastrophic galvanic corrosion.

The countermeasure applied in this study is to use Kevlar as the insulation buffer between the CFRP and AA. Kevlar fibers were embedded in the metal matrix instead of CF. The tensile and cross-tensile testing results elucidate that this approach can generate high joint strength. CCT tests were performed on samples with the buffer, CF-inside, and CF-outside designs. The samples with buffer design were able to maintain 99.5% mass and 95% tensile strength. The KFRP buffer successfully avoided galvanic corrosion in the samples during the 120-day CCT process.

Chapter 7: CFRP-1010 Steel Joints by UAM

7.1 UAM process for 1010 steel

7.1.1 UAM parameter for annealed 1010 steel

To expand the application of the FRP-metal joint from AA to steel, a reliable method to create steel builds with UAM is critical. The UAM team has experience making 4130, and 410 steel builds with a baseplate preheated to 400^oF. However, this temperature is not suitable for making fiber-metal joints due to difficulty in placing the fibers in the channels by hand. 1010 steel is softer and easier to weld at room temperature. Therefore, 0.127 mm thick, 20.32 mm wide 1010 steel foil has been chosen as the feedstock for the Kevlar-steel joints. The foil is thinner than typical steel foil, requiring less power to create a robust metallic bond using UAM. Also, the sonotrode used to weld 1010 is coated with Stellite 6 to avoid bonding between the feedstock and steel horn, which is a typical issue when welding steel using UAM. Stellite is a cobalt-chromium alloy that has high wear resistivity. Also, its thermal conductivity is lower than steel, which is favorable in generating high-strength UAM bonding.

To increase the weldability of the as-received 1010 steel foil, the material was annealed before the UAM process. The roll of 1010 foil tape was placed in a stainless steel tool bag to prevent any oxidation during the heat treatment. The material was heated to 926°C and held for at least 30 minutes, based on the actual volume of the foil. Then the foil was cooled down to 26°C in the furnace with a cooling rate of 37.5°C/hour. Tensile tests were performed on as-received and annealed 1010 steel foils, and the result is plotted in Figure 7.1. By annealing the foil, the UTS reduced from 730 MPa to 321 MPa, which the elongation at break increased from 2.3% to 18.5%. This significant increase in ductility elucidates that the annealed tape is more favorable in creating voidless bonding via UAM.

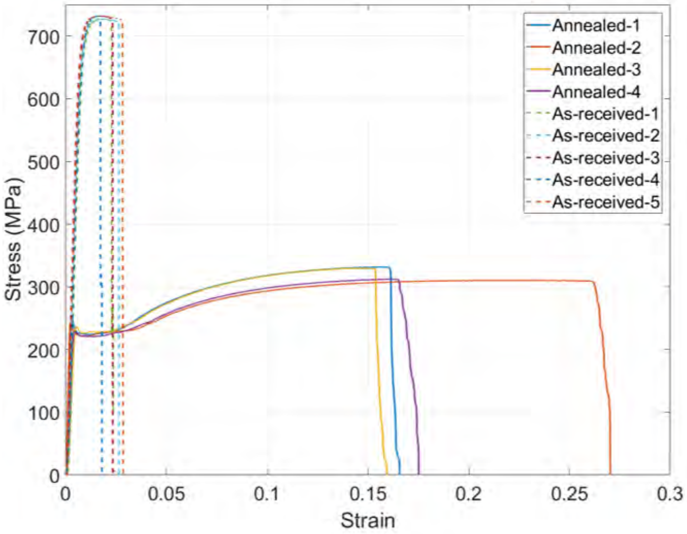

Figure 7.1: Stress vs strain curves of as-received and annealed 1010 steel foil tapes.

An issue that may occur when welding steel using UAM is that the power required to generate the weld exceeds the power that the machine is able to supply. To eliminate this problem and decrease power consumption, two 0.2 mm deep grooves are machined on the baseplate to reduce the contact width between the foil and the baseplate. As shown in Figure 7.2, the weld width is 17.78 mm, which is smaller than the 25.4 mm horn width.

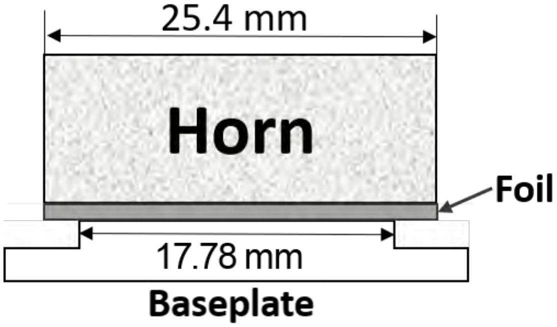

Figure 7.2: Head-on view of the horn in contact with the baseplate, creating a 20.3 mm wide weld.

A 12.7 mm thick A36 baseplate was securely placed on the vacuum chuck, machining channels to create the 17.78 mm wide weld area, and pretexturing the weld area using the parameters listed in Table 7.1. A series of weld trials were conducted to develop parameters for welding 1010 steel foil to the baseplate and for welding 1010 steel foils on top of previously welded foils. The resulting parameters are listed in Table 7.1. There are three amplitude values listed in the table for different weld layers. The increase in amplitude as the samples built higher is to ensure consistent UAM power as the build becomes more compliance[19]. A 2 mm thick (16-layer) build was successfully created using these parameters, as shown in Figure 7.3. The shear samples tested in Section 7.1.2 were cut from this build. Also, a cross-section was cut from the 1010 build. From the optical image of the cross-section shown in Figure 7.4, a voidless bond has been achieved in both foil-foil and foil-base interface.

Table 7.1: UAM parameters for welding 1010 steel at room temperature.

	Force (N)	Speed (cm/s)	Amplitude (μm)
Texture	4500	6.4	25.5
Weld layer 1 to 7	6500	3.0	29.6
Weld layers 8 to 15	6500	3.0	30.0
Weld layer 16	6500	3.0	30.5

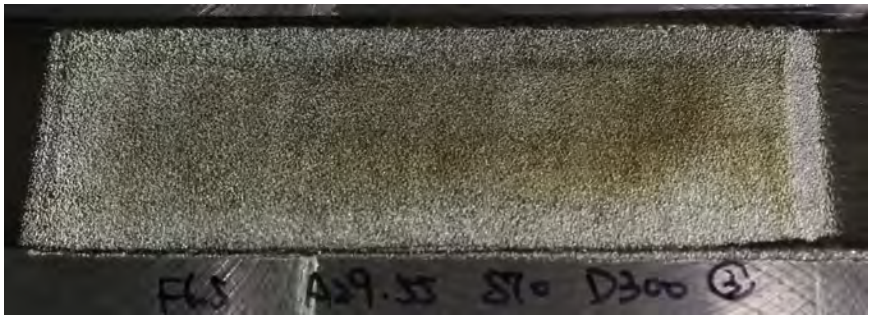

Figure 7.3: A 2 mm thick 16-layer 1010 steel build.

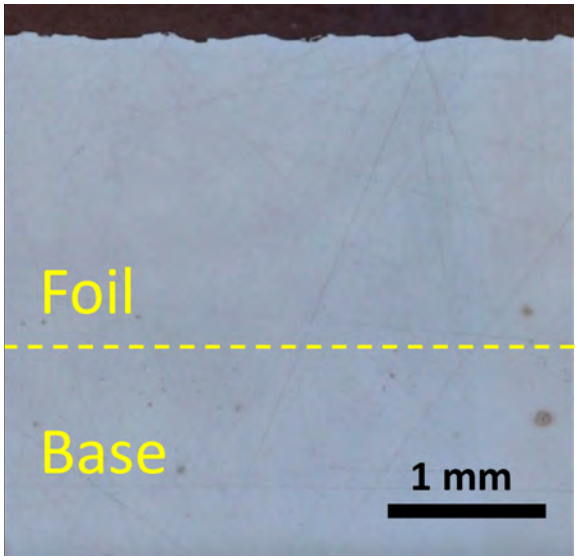

Figure 7.4: Cross-section image of the UAM 1010 build.

7.1.2 Shear tests of 1010 steel UAM welds

Shear samples were cut from the 16-layer build shown in Figure 7.3. The samples were 4.95 mm in length and width. The side-views of the shear samples are illustrated in Figure 7.5 (a) and (b). The transverse shear tests are shearing the samples through the foil layers to characterize the bulk shear strength of post-UAM 1010 foil. The interface shear samples were tested by shearing at the interface between the 2nd and 3rd 1010 layers to evaluate the UAM bonding strength. The shear samples were machines to a stepped shape to ensure that the sample shears at the desired interface. Using the fixture shown in Figure 7.6, the samples are tested using an MTS C43-504 load frame.

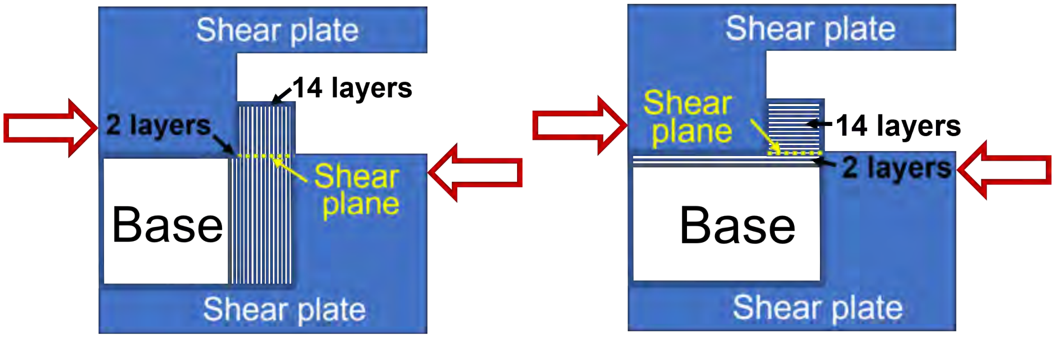
Shear plate
14 layers
2 layers
Shear plane
Base
Shear plate
Shear plate
Shear plane
14 layers
2 layers
Base
Shear plate

(a) (b)

Figure 7.5: (a) Schematic of a transverse shear sample in the fixture; (b) schematic of a interface shear sample in the fixture.

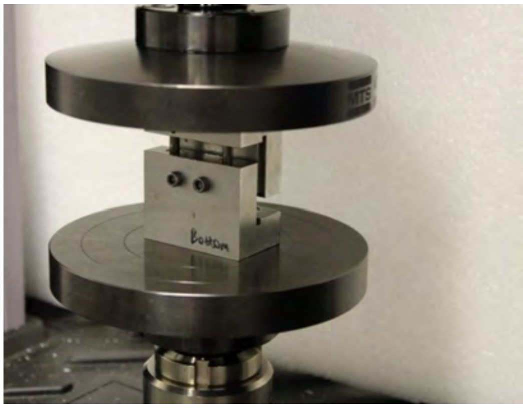

Figure 7.6: Shear fixture between two compression platens in the load frame.

Transverse shear strength of 1010 steel UAM build

Four transverse shear tests were performed, and Figure 7.7 shows the stress vs. strain curves of the transverse shear samples. The ultimate shear strengths are listed in Table 7.2. The average transverse shear strength is 397 MPa, which is higher than the tensile strength of the annealed 1010 steel (321 MPa). Because the shear strength of steel is commonly estimated to be 75% of the tensile strength, the 397 MPa shear strength indicates that the post-UAM 1010 build has a higher tensile strength than the pre-UAM annealed 1010 feedstock. This strengthening comes from the extensive work hardening during UAM.

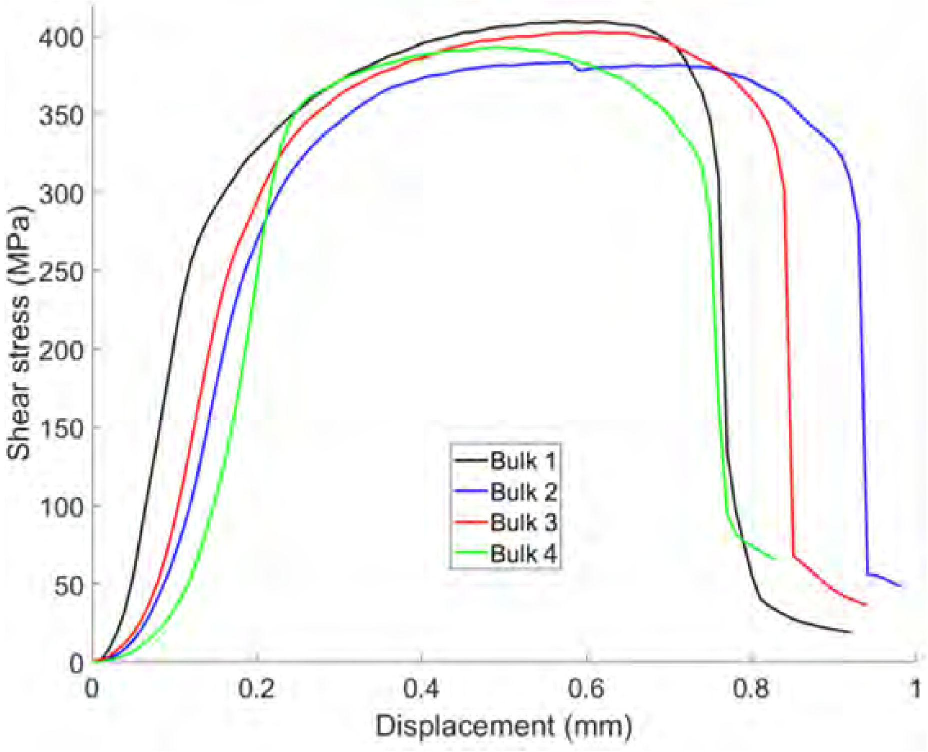

Figure 7.7: Stress vs. strain curves of transverse 1010 steel shear tests.

Table 7.2: Transverse shear strengths of 1010 steel samples

	Shear strength (MPa)
Sample 1	409.30
Sample 2	383.17
Sample 3	402.61
Sample 4	392.66
Average	396.91
Standard deviation	13.57

Interface shear strength of 1010 steel UAM build

Twelve shear samples were prepared to evaluate the UAM bonding strength. The sample locations are shown in Figure 7.8. The white bar indicates the exact location of the shear plane in the step-shaped shear samples. The matrix is defined to investigate the edge effect of 1010 UAM welds.

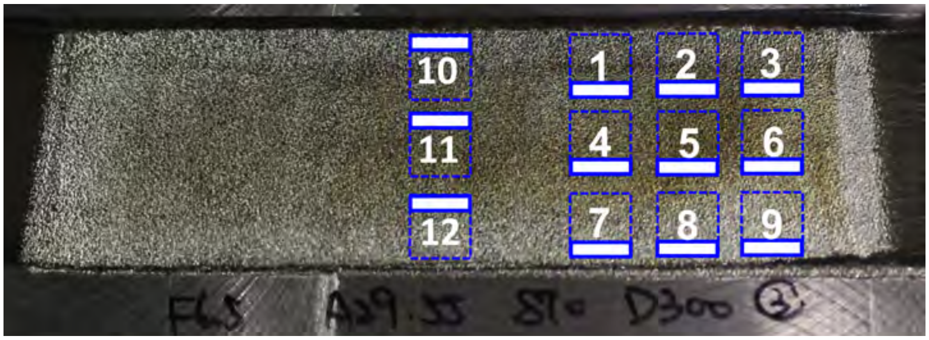

Figure 7.8: Location of interface shear samples on the 1010 steel build.

The stress vs. strain curves of the interface shear tests are plotted in Figure 7.9. Sample 1 was sacrificed while being machined to the stepped shape, therefore was not tested. The black curves are samples at the edge of the welds. The red curves are samples at the center region, and blue curves are those with some distance from the edge but not at the center. Table 7.3 lists the ultimate shear strength of the tested samples. From the table, most of the samples have shear strengths in the range between 380 to 410 MPa. The samples that have lower shear strengths are 7, 8, 9, and 10. Figure 7.10 listed the shear strength of the samples at their relative locations. All the samples at the edges have low shear strength, while there is no significant difference between the samples at the center and intermediate locations.

The criterion of a good UAM bonding is the ratio between interface and bulk shear strength. For this study, the test results are benchmarked against the transverse shear results from Section 7.1.2. Considering all the locations, the average interface shear strength is 346.64 MPa, which is 87.3% of the build shear strength. If we exclude the samples impacted by the edge effect, the 388.24 MPa average shear strength reaches 97.8% of the bulk strength. The high percentage of bulk strength indicates that the UAM parameters are appropriate for 1010 steel welds.

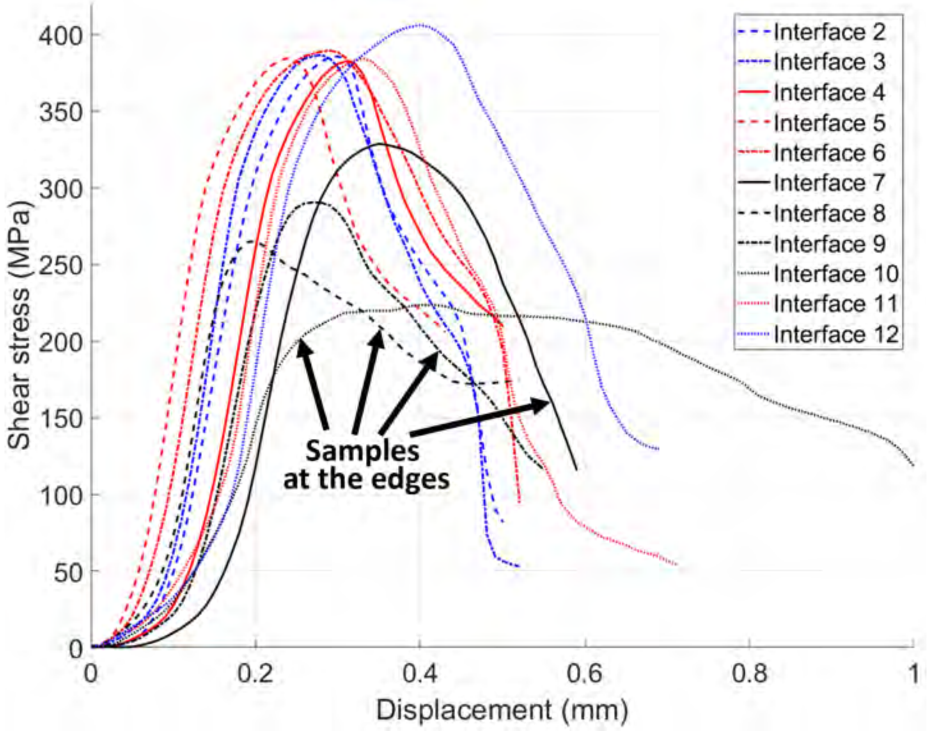

Figure 7.9: Stress vs. strain curves of interface 1010 steel shear tests.

Table 7.3: Interface shear strengths of 1010 steel samples

	Shear strength (MPa)
Sample 2	385.48
Sample 3	386.46
Sample 4	382.43
Sample 5	384.18
Sample 6	389.27
Sample 7	316.53
Sample 8	265.08
Sample 9	290.28
Sample 10	223.45
Sample 11	383.88
Sample 12	406.00
Average of all samples	346.64
SD of all samples	61.99
Average of non-edge samples	388.24
SD of non-edge samples	7.80

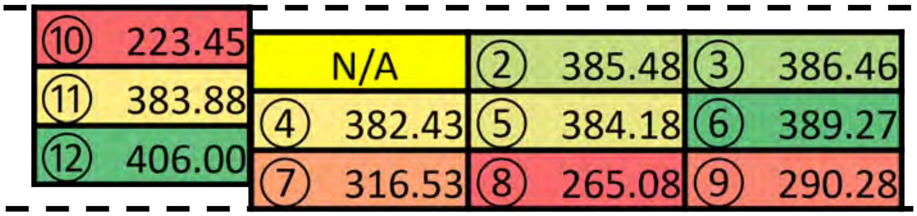
⑩ 223.45
⑪ 383.88
⑫ 406.00
N/A
② 385.48
③ 386.46
④ 382.43
⑤ 384.18
⑥ 389.27
⑦ 316.53
⑧ 265.08
⑨ 290.28

Figure 7.10: Ultimate interface shear strength.

7.2 Kevlar-1010 steel joint

7.2.1 Sample preparation

Following the same procedures as building CFRP-AA joints as described in Section 2.1.2, and using the UAM parameters introduced in Section 7.1, a Kevlar-steel joint has been built by embedding two layers of Kevlar loops in 13 layers of 1010 steel, as shown in the schematic in Figure 7.11. The total joint thickness is 1.78 mm. No foil tearing or cracking is observed. The samples were then cured with West System epoxy and tested in tension.

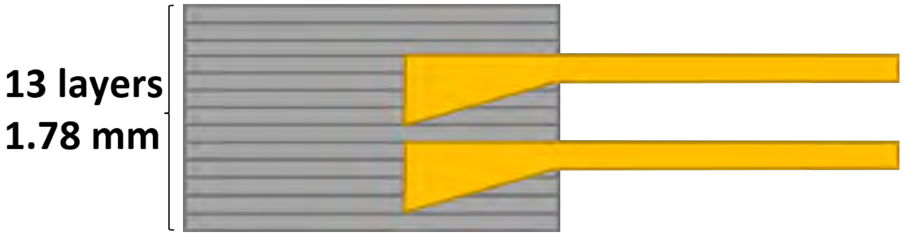

Figure 7.11: Side-view schematic of the KFRP-1010 tensile sample.

7.2.2 Tensile test of KFRP-1010 steel UAM joint

After curing, the KFRP-1010 steel tensile samples were trimmed to 25.4 mm wide using an abrasive wheel. The samples before testing were shown in Figure 7.12 (a). The samples were tested at a rate of 1.27 mm/min in an MTS load frame, and Figure 7.12 (b) shows the samples after testing. As shown in the picture, the samples failed only in the Kevlar, no steel delamination or breaking is observed, as shown in Figure 7.12 (b). This indicates that the UAM bonding is strong enough to avoid any delamination and the load-bearing steel is stronger than the embedded Kevlar.

Figure 7.13 plots the load vs. displacement curves of the samples. The average tensile peak load is 3076 N. The curves are consistent in peak load, with a standard deviation of 114 N. The elongation at break is more scattered because the displacement being plotted is from the crosshead instead of the virtual extensometer from DIC (DIC analysis was not applied to the tests due to large deformation in the fibers). After fiber breaking at the peak, the curves have the same pull-out tail as the 3-CF-layer cases in Figure 2.9.

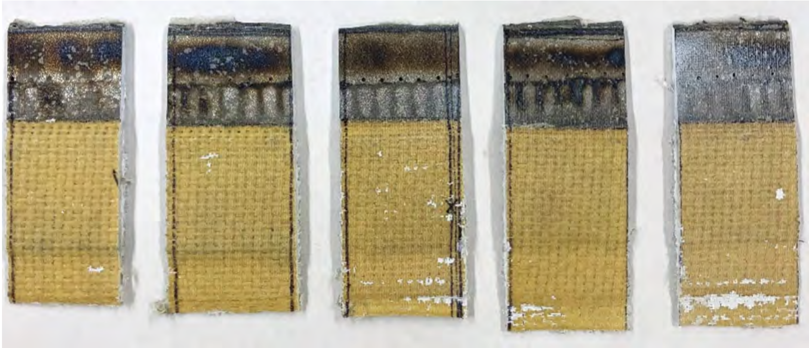

(a)

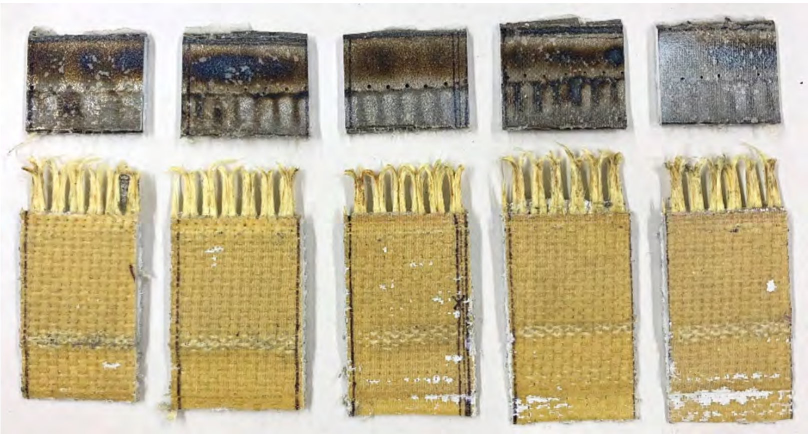

(b)

Figure 7.12: (a) KFRP-1010 samples before tensile testing; (b) KFRP-1010 samples after tensile testing.

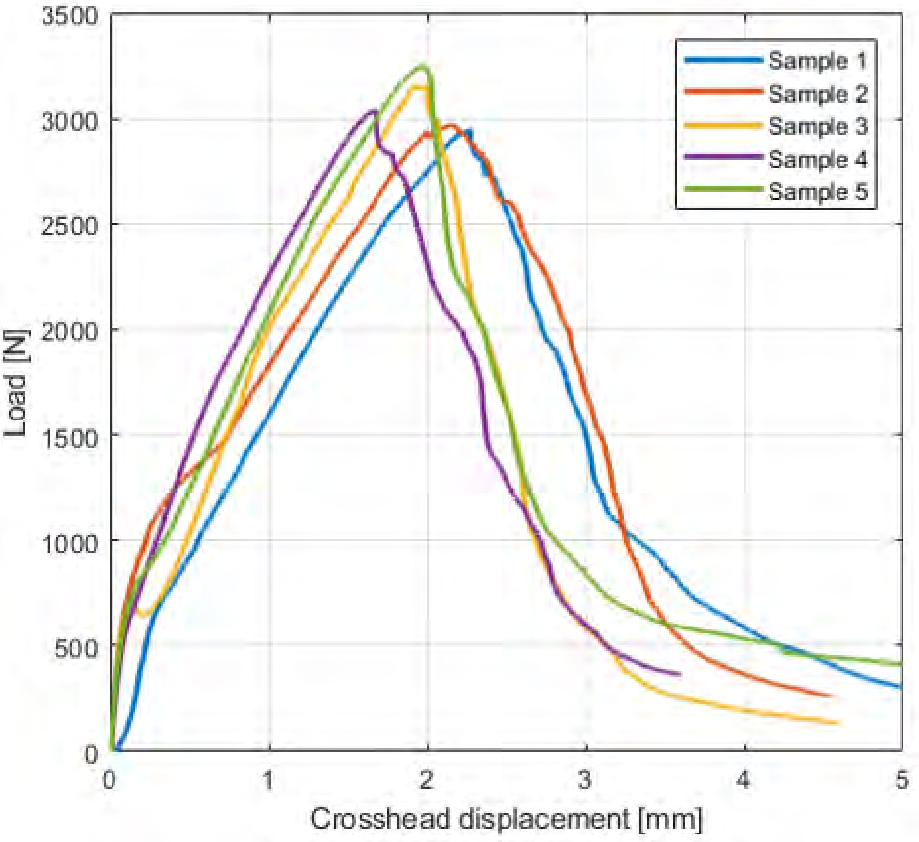

Figure 7.13: Load vs displacement curves of KFRP-1010 tensile tests.

7.3 Effect of RSW on Kevlar-1010 steel joints

JAC 270 is a type of galvannealed steel from Honda that has been widely used in body structure. It has a thin layer of alloyed zinc and steel on the surface. To investigate the compatibility of UAM 1010 steel in the body-in-white, a study of optimal RSW parameters for welds between 1.8 mm thick UAM 1010 and 2.0 mm thick JAC 270 was carried out. A series of parameters were attempted, and a final set of parameters were chosen by RSW technicians based on preliminary evaluations, as listed in Table 7.4. Studies in Section 7.3.1 and 7.3.2 use this set of parameters to prepare RSW samples.

Table 7.4: RSW parameters for UAM 1010 and bulk JAC 270

Cycles	Hold 10 – Weld 10 – Hold 10 (60 Hz)
Current	38 kA
Force	350 kg
Tip	16 mm DR50

7.3.1 Lap shear test of RSW between UAM 1010 and JAC 270

Three 1.8 mm thick UAM 1010 samples were prepared using the parameters listed in Table 7.1. The samples were joined to 2.0 mm thick JAC 270 using RSW, as pictured in Figure 7.14 (a). The load vs. displacement curves of the lap shear tests are plotted in Figure 7.15, and the peak loads are listed in Table 7.5. Figure 7.14 (b) shows the samples after testing. They did not fail in the RSW by a plug or interfacial fracture. The failure occurred in the UAM 1010 base material instead. The reason is that the width of the samples is only twice the RSW nugget diameter. However, the width of the samples is limited by the sonotrode width of the UAM system. Therefore, increasing the sample width will need more investigation in the UAM process, which is out of the scope of the research objective. Since the average peak load of 15.3 kN from these tests is high enough to prove that the RSW parameter can generate high strength bonding between the UAM 1010 and JAC 270, no additional efforts have been made to redo this test. As shown in Figure 7.15, Sample 1 failed by one load drop, corresponding to the fracture at the bottom of the RSW nugget. Samples 2 and 3 exhibit two load drops that correspond to failure in the base material on the left and right-hand sides at the bottom of the nugget. Figure 7.14 (b) also shows out-of-plane deformation in samples 2 and 3, which is due to pulling on one side of the base material after the initial fracture on the other side.

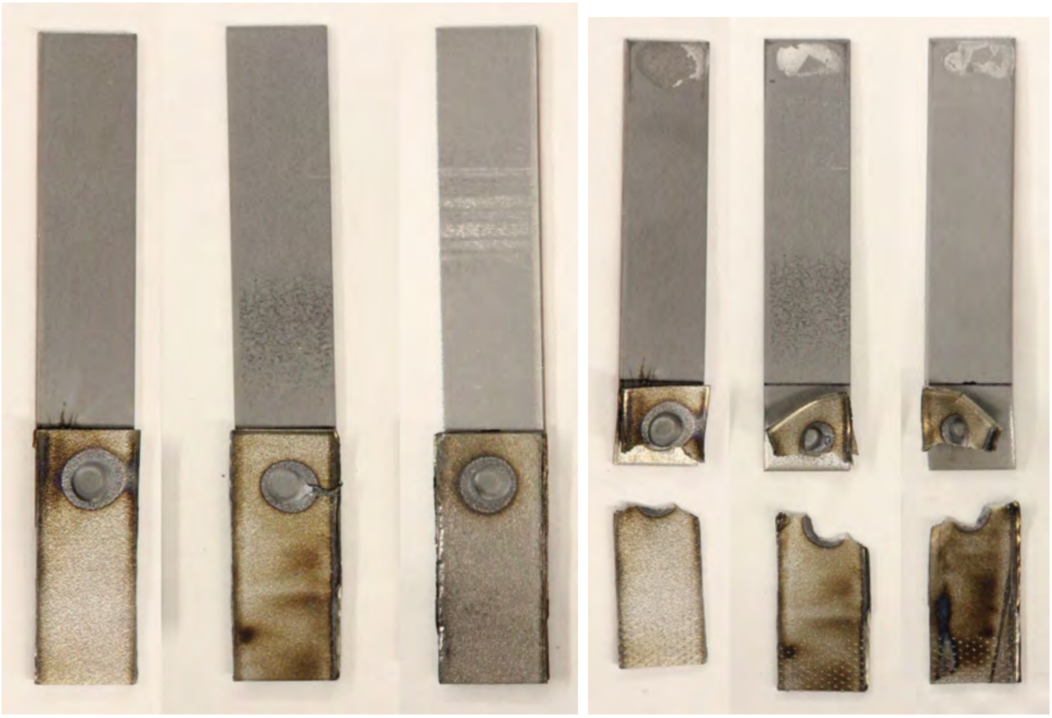

(a) (b)

Figure 7.14: (a) UAM 1010-JAC 270 RSW samples before lap shear testing; (b) UAM 1010-JAC 270 RSW samples after lap shear testing.

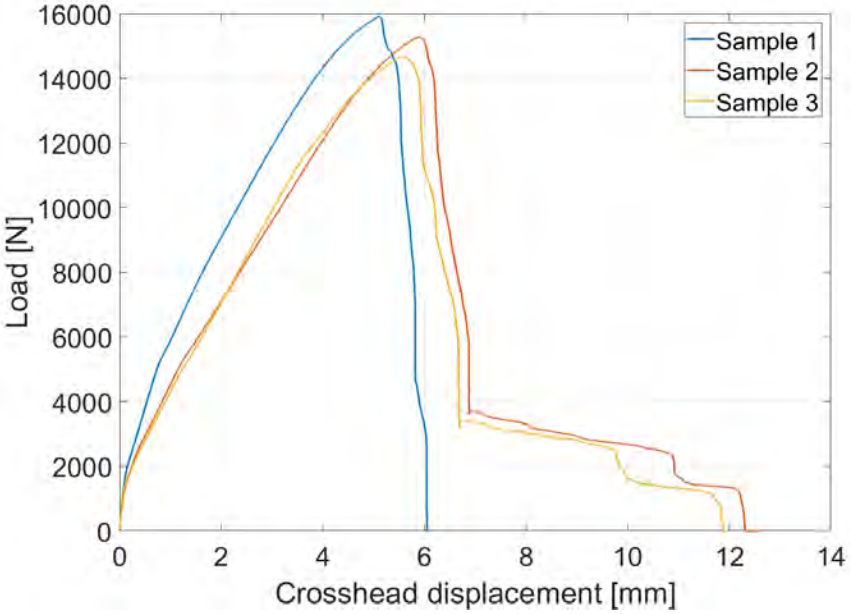

Figure 7.15: Load vs displacement curves of UAM 1010-JAC 270 RSW lap shear tests.

Table 7.5: Lap shear peak load of RSW between UAM 1010 and JAC 270

	Peak load (N)
Sample 1	15902
Sample 2	15278
Sample 3	14678
Average	15286

7.3.2 Heat affected zone of RSW between UAM 1010 and JAC 270

Cross-sectional images were taken in one RSW between UAM 1010 and JAC 270, and microhardness mapping was performed on the same sample to characterize the heat affected zone, as shown in Figure 7.16. The top piece is UAM 1010, and the bottom piece is JAC 270. From the optical image, there is no void on the UAM side. Two small vertical cracks are observed on the JAC 270 side, as shown in the yellow square. This is a typical phenomenon in RSW caused by the zinc coating on the surface of the galvannealed steel. The small voids at the center of the RSW formed during the re-solidification of the mixture of melted steel[46]. The hardness mapping was performed with an indentation force of 150 kgf. The original hardness of UAM 1010 and JAC 270 are both around 160 HV. In the HAZ, the hardness increased to the range from 250 to 250 HV. The mismatch in electrical and thermal conductivity of 1010 and JAC 270 lead to asymmetrical HAZ of the RSW[5].

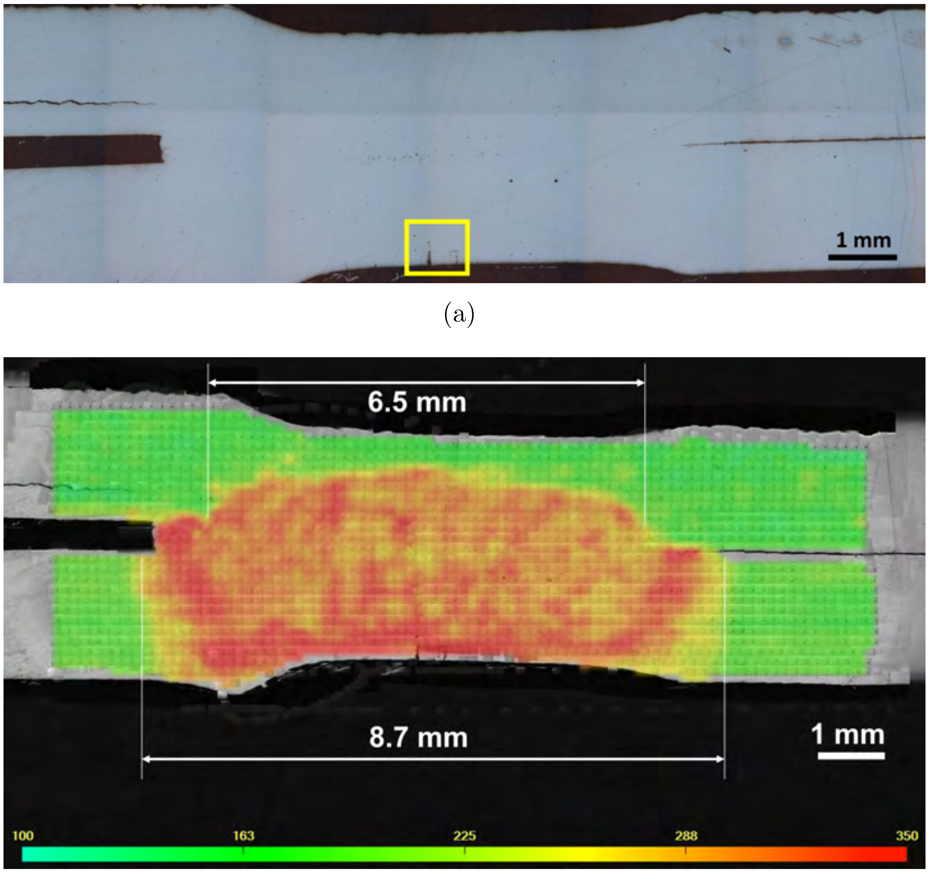

(a)

(b)

Figure 7.16: Cross-section of an RSW between UAM 1010 and JAC 270: (a) optical image; (b) microhardness map.

7.4 Corrosion mitigation investigation of Kevlar-1010 steel joints

To characterize the galvanic corrosion property of the CFRP-KFRP-1010 steel joints via corrosion cyclic testing, a set of KFRP-1010 samples were prepared using the same stack up sequence and weld parameters as Section 7.2.1. The samples were layed up using the configuration with a Kevlar buffer as described in Section 6.3.1. Then RSWs were applied to join the samples to a piece of 2.0 mm thick JAC 270 using the parameters listed in Table 7.4. The post-RSW samples were then E-coated with industry-standard approach, and the final samples are shown in Figure 7.17.

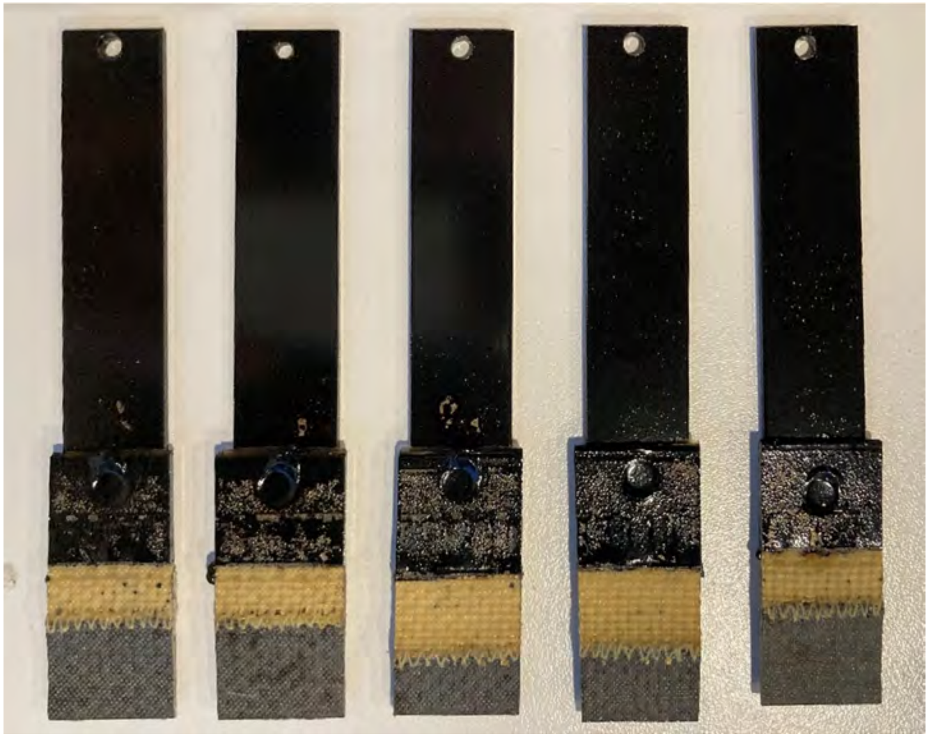

Figure 7.17: KFRP-1010 joint with RSW to JAC 270 and E-coat prior to CCT.

As analyzed in Section 6.3.3, the CFRP-KFRP-AA samples were able to maintain the strength after a 120-day CCT process. Based on the galvanic series shown in Figure 7.18, the difference of potential between low carbon steel and graphite is smaller than the difference between aluminum ally and graphite. We should expect the samples with steel to corrode less than the samples with aluminum.

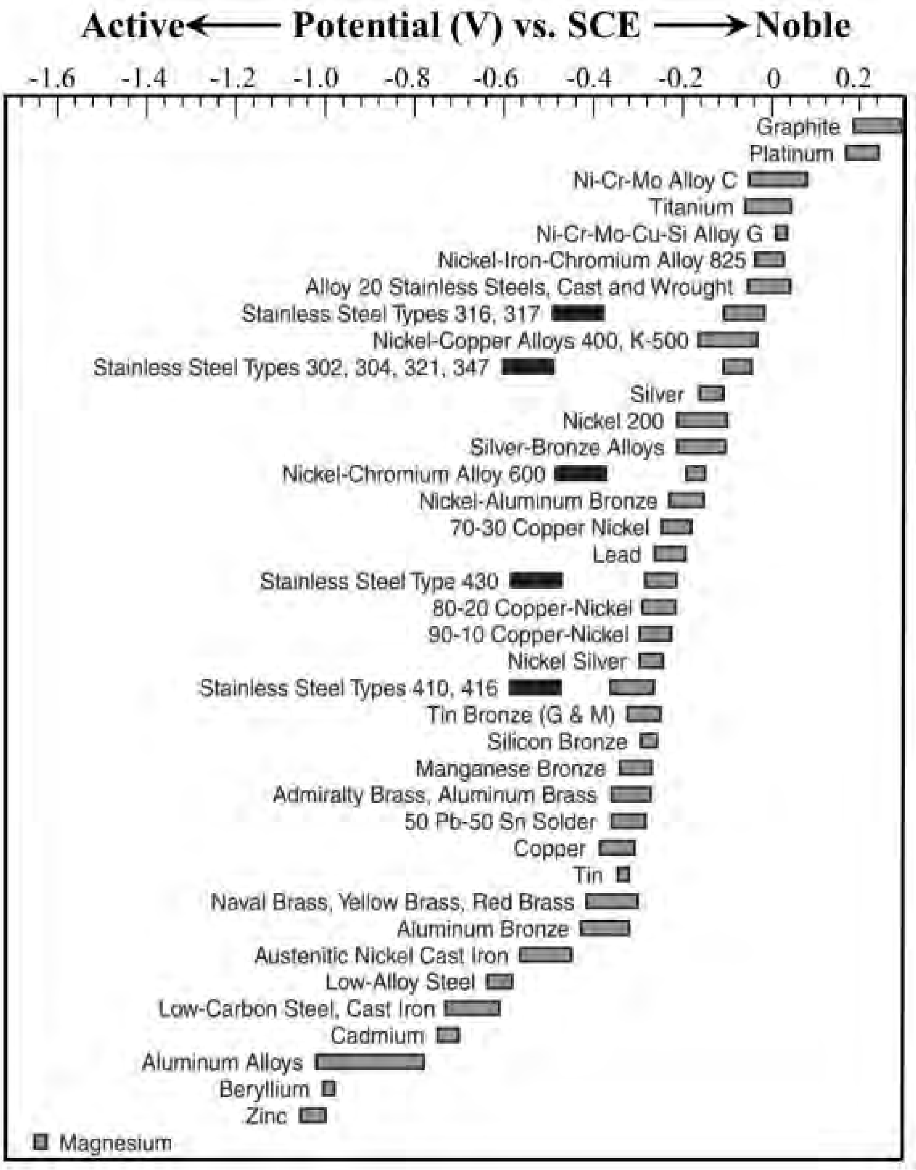

Figure 7.18: Galvanic series in ambient seawater [54].

After 120 days of corrosion cycles with the process per cycle listed in Table 6.2, the samples were pulled out from the corrosion chamber. The samples were severely corroded after the CCT process, which does not agree with the prediction. Three possible reasons are:

- Although the E-coating was performed after RSW, the interface between the transition joint and JAC 270 can easily crack and become an initiator of corrosion due to lack of coating protection.

- The 1010 steel in the transition joint is very susceptible to corrosion by itself. Also, it was not properly pre-treated before E-coating, while in the industry, the steel parts usually receive a zinc or iron phosphate treatment prior to E-coating. The absence of such treatment can compromise the effectiveness of E-coating.

- The FRP may draw moisture into the channel feature inside the 1010 steel, which was not coated. This may induce corrosion in 1010 steel

A possible countermeasure is to use stainless steel, instead of carbon steel, as the matrix of the transition joint. The UAM lab has experience in welding stainless steel 410[16]. Although the previous study shows that an elevated baseplate temperature of 400°F is required to obtain high strength UAM bonding, there are several options that may reduce the required temperature and enable personnel to handle the fibers to be embedded. For example, using the Stellite-coated sonotrode increases the interface temperature during welding, which can generate higher strength bonding compared to regular sonotrode when using the same UAM parameter.

7.5 Summary

A study has been carried out to create CFRP-1010 steel joints using UAM and characterize its mechanical properties, RSW compatibility, and corrosion performance. A UAM manufacturing setup has been developed to generate high-strength bonding between annealed 1010 foils. The work hardening effect from UAM strengthened the annealed 1010. Also, the interface shear strength reaches 87.3% of the bulk shear strength. Kevlar-1010 steel joints were prepared and tested in tensile. The tensile peak load of the 2-Kevlar-layer samples reached 3076 N and failed in the Kevlar fiber. The failure mode and joint strength match the prediction based on the stack sequence and material properties.

The RSW weldability of UAM 1010 to JAC 270 is studied. Lap shear tests were carried out to evaluate the weld quality. Although the samples did not fail in the RSW, the peak load of 15.3 kN indicates that the strength of the RSW is sufficient to be applied to a vehicle body structure. Corrosion evaluation was performed on CFRP-KFRP-1010 steel joints with KFRP buffer as electrical insulation between CFRP and 1010 steel. The result shows that corrosion has occurred to the samples, future work is needed to investigate the countermeasure, such as swapping the matrix material from carbon steel to stainless steel.

Chapter 8: Conclusions and Future Work

8.1 Summary

This study developed a method to create high strength FRP-metal joint using UAM by embedding fiber loops in the metal matrix. A sheet welding method has been applied to consolidate fiber while avoiding foil tearing. This approach creates continuous FRP to metal joints that can serve as weld tabs to enable FRP to be integrated into vehicle structures using conventional metal-metal joining methods.

Carbon fiber has been successfully embedded in AA 6061-H18 without damage to the fibers, which has been verified by optical images. The optical images also show that the vent hole design enabled the epoxy to flow into the channels and ensure load sharing among fibers. The tensile test results of CFRP-AA joints exhibit two possible failure modes: CF tow failure and AA matrix failure. The samples that failed in CF tows have an average peak load of 4677 N and absorb 3.96 J energy due to the pull-out of the embedded fiber after the initial peak. The AA samples that exhibit the AA matrix failure mode failed at 7238 N on average but have 0.9 J energy absorption. The failure mode can be tailored by adjusting the CF:AA bearing area ratio to achieve high energy absorption or high peak load. Cross-tensile tests were also performed on CFRP-AA samples. The samples failed with a peak load of 2318 N and were primarily fractured by CF tow shearing along the edge of the AA matrix.

To investigate the RSW weldability of UAM AA 6061-H18 to bulk AA 6061-T6, tensile and cross-tensile tests have been carried out. Although the average lap shear and cross-tensile peak loads of UAM-bulk RSW are both lower than bulk-bulk RSW, the strength of UAM-bulk RSW is satisfactory for structural welds. This is also verified by the plug fracture failure mode of the samples, which is typical evidence of high strength RSW of AA. The main reason for lower RSW strength in the UAM-bulk samples is the base material strength difference. The tensile strength of bulk 6061-T6 is 290 MPa from the datasheet, while experiments show that the tensile strength of UAM 6061-H18 is 195 MPa. Hardness testing was performed on the UAM-bulk RSW to characterize the heat affected zone. The diameter of HAZ is measured to be 11 mm by line scanning and 12 mm by mapping. Tensile tests were performed on CFRP-AA joint samples with RSW applied at various distances from the CFRP-AA interface. The result shows that the safe distance between the RSW center and CFRP-AA interface is 16.5 mm, which is also verified by optical images.

By applying the CFRP-AA transition joint with RSW, hybrid beam structures have been manufactured to characterize the performance of the joining technique compared to traditional rivet joints for dissimilar materials. The four-point bending results show that the method of RSW through CFRP-AA transition joints is significantly superior in terms of energy absorption and crush force efficiency. The innovative joining technique also enables the structure to maintain integrity after the initial fracture. When tested in dynamic axial crush, the UAM samples have less peak load and crush distance, with higher energy absorption. The crush force efficiency of UAM beams is twice that of the rivet beams. Torsion tests were also performed, exhibiting the advantages of UAM beams in terms of higher peak torque and energy absorption. In contrast to the abrupt simultaneous shearing failure of multiple rivets, the UAM samples failed by gradual shearing of the CFRP-AA interface, which is beneficial in structural integrity.

Galvanic corrosion has been the primary concern in hybrid structures. To characterize the effect of galvanic corrosion on the CFRP-AA joints, CCT tests were performed on the samples for 120 days to simulate a 12-year weathering. The result shows that the aluminum would severely corrode due to galvanic coupling to CFRP even with E-coat. To address this issue, a countermeasure of using Kevlar as a buffer has been proposed. Mechanical tests show that the joint strength is not compromised by switching the embedded fibers from CF to Kevlar fibers. Another 120-day CCT test has been carried out on samples with the countermeasure. The samples maintain 95% of the tensile strength, with no mass loss or appearance degradation.

To investigate the feasibility of the join concept in steel, a study to create KFRP-1010 steel joints has been performed. A UAM process that produces high-strength bonding between annealed 1010 steel foils has been developed. The shear tests show that the interface strength is 87% of the bulk shear strength. With the developed UAM process, KFRP-1010 samples were prepared and tested in tensile. The average tensile peak load is 3076 N, which matches the strength prediction based on the two-Kevlar-embedded stack sequence. A study to evaluate the RSW weldability of UAM 1010 steel and bulk JAC 270 shows that the RSW strength reaches 15 kN. The HAZ of the RSW is measured to be 8.7 mm via hardness mapping. Asymmetry is observed in HAZ due to thermal and electrical conductivity differences between 1010 and JAC

270. A preliminary corrosion study has been carried out on KFRP-1010 joints welded to JAC 270 by RSW and then E-coated. The result shows that this configuration cannot survive a 120-day CCT test. A possible countermeasure is to use stainless steel instead of carbon steel to avoid corrosion of the metal matrix.

8.2 Contributions

1. Developed UAM method to create high strength FRP-metal joints
    - Sheet welding is effective in avoiding foil tear when welding over channels to encapsulate fibers
    - When tested in tension, FRP-metal joints can fail in fiber and achieve high energy absorption from fiber pull-out process after initial fiber fracture, or fail in metal with high peak load
    - The tensile failure mode of FRP-metal joints can be tailored by tuning FRP:metal bearing area ratio
2. Demonstrated the feasibility of using the FRP-metal joints as RSW weld tabs to join FRP with metal structures
    - RSW through UAM 6061-H18 and bulk 6061-T6, and though UAM 1010 and bulk JAC 270 are both characterized by mechanical testing and hardness mapping. Both cases generate high-strength RSW joining.
    - RSW can be applied to FRP-metal joints without damage to the embedded fibers due to heat and avoid compromising the strength when following a safe distance

3. Characterized the benefits of FRP-metal transition joints and RSW in structural tests
    - Four-point bend, axial crush, and torsion tests of beam structures prove that joining method of RSW through UAM transition joint has advantages in energy absorption and force crush efficiency compared to conventional rivets
    - The transition joint improves the structural integrity after the initial fracture
4. Developed analytical and FEA models of the FRP-metal joints in tensile tests
    - The analytical model is able to predict the joint tensile strength and failure mode based on the material properties and joint geometry
    - The efficient FEA model generates simulation that accurately predicts the tensile performance of the FRP-metal joints
5. Investigated the galvanic corrosion mitigation method for FRP-metal joints
    - CCT tests were performed on CFRP-AA joints and proved insufficient protecting with solely E-coat
    - A countermeasure using Kevlar buffer has proved to be effective in preventing galvanic corrosion by CCT tests
    - Zero mass loss and high post-corrosion tensile strength can be achieved after a 12-year equivalent CCT on CFRP-AA joints

6. Developed the UAM process for welding 1010 foil and achieving high shear strength
    - The UAM parameters to weld annealed 1010 foil at room temperature has been determined
    - Shear tests show that the 1010 welds achieve high bonding strength

8.3 Future work

Modeling

The first future work related to modeling is to obtain experimental measurements for the analytical model of the FRP-metal joints. The presented work completed preliminary tests on CFRP. However, there are multiple approaches to characterize the mechanical properties of FRPs, and a study to determine an accurate method would help calibrate the analytical model. Also, to apply the model to joint with KFRP buffer, experiments on KFRP would be necessary.

Another future work is related to the accuracy of FEA models. Although the homogenized shell model can accurately predict the failure of the joints under tensile load, the fiber pull-out process is not included in the current model. An improvement in the model to capture this feature would be critical to simulate the energy absorption of the test.

Lastly, simulations of the structural tests are necessary to validate the accuracy of the joint model in component-level FEA models. Hat sections have been tested in three load cases in this project. To simulate these tests, not only an accurate joint model is needed, but also the material cards of the base materials (CFRP and

AA) need to be calibrated. Mechanical tests on the base materials are necessary to calibrate the material cards.

Manufacturing

The standard UAM manufacturing process creates a 25.4 mm wide metal tab, which is limited by the width of the sonotrode. It is possible to create wider AA tabs by using sheet foils and welding multiple side-by-side passes. However, the seam between two passes is still a weak point. Investigation to achieve a wider UAM weld would be valuable to make the metal width of the FRP-metal joint to be more flexible and easier to accommodate RSW.

The CCT results indicate that more investigation is required to prevent galvanic corrosion in CFRP-KFRP-1010 steel joints. One possible solution is to use stainless steel as the metal matrix material. The UAM lab has previously demonstrated that the stainless steel 410 can be UAM welded with high bonding strength at an elevated temperature using an uncoated sonotrode. With the Stellite-coated sonotrode, it is possible that UAM bonding of stainless steel 410 can be created at lower or room temperature, which enables manufacturing of FRP-stainless steel joints.

Appendix A: Corrosion study data

Table A.1: Tensile peak loads of samples after CCT process (unit:N)

Grp.	Cyc.	Sample 1	Sample 2	Sample 3	Sample 4	Sample 5	Sample 6
1	0	A11	B1	C3	D5	E7	N/A
		3611	3684	3736	3610	3678	
2	25	A4	B6	C8	D10	E12	
		3923	3402	3994	3890	3643	
3	50	A9	B11	C1	D3	E5	
		3846	3516	3674	3746	3822	
4	60	A8	B10	C12	D2	E4	
		3897	3350	3210	3585	3495	
5	70	A2	B4	C6	D8	E10	
		4205	3789	4494	3308	3447	
6	80	A1	B3	C5	D7	E9	
		4260	3533	4045	3633	3258	
7	90	A6	B8	C10	D12	E2	
		4074	3060	3962	3208	3132	
8	100	A12	B2	C4	D6	E8	
		3227	3981	4275	3485	3812	
9	110	A5	B7	C9	D11	E1	
		3680	3434	3736	3980	2895	
10	120	A7	B9	C11	D1	E3	
		3969	3158	3223	3817	3523	
11	0	A3	B5	C7	D9	E11	
		3899	3838	4142	3554	3882	
12	120	A10	B12	C2	D4	E6	
		3739	3086	4193	3702	3720	
13	120	F1	F2	F3	F4	F5	F6
		2879	2992	2377	2727	1111	2411
14	120	F7	F8	F9	F10	F11	F12
		3262	3094	3207	2910	2325	2394

Table A.2: Masses of samples before and after CCT process (unit:g). Samples 1 to 3.

Grp.	Cyc.	Sample 1			Sample 2			Sample 3		
		m_1	m_2	Δm	m_1	m_2	Δm	m_1	m_2	Δm
1	0	A11			B1			C3		
		4.16	4.16	0	4.48	4.48	0	4.79	4.78	0.01
2	25	A4			B6			C8		
		4.55	4.56	-0.01	4.75	4.77	0.02	4.61	4.6	0.01
3	50	A9			B11			C1		
		4.43	4.41	0.02	4.63	4.63	0	4.85	4.83	0.02
4	60	A8			B10			C12		
		4.27	4.27	0	4.60	4.60	0	4.66	4.64	0.02
5	70	A2			B4			C6		
		4.48	4.47	0.01	4.72	4.71	0.01	4.72	4.69	0.03
6	80	A1			B3			C5		
		4.52	4.52	0	4.78	4.75	0.03	4.63	4.63	0
7	90	A6			B8			C10		
		4.46	4.46	0	4.68	4.67	0.01	4.83	4.83	0
8	100	A12			B2			C4		
		4.47	4.44	0.03	4.79	4.79	0	4.78	4.77	0.01
9	110	A5			B7			C9		
		4.50	4.49	0.01	4.62	4.61	0.01	4.71	4.69	0.02
10	120	A7			B9			C11		
		4.46	4.46	0	4.62	4.61	0.01	4.74	4.72	0.02
11	0	A3			B5			C7		
		4.43	4.43	0	4.72	4.72	0	4.80	4.80	0
12	120	A10			B12			C2		
		4.52	4.52	0	4.60	4.60	0	4.83	4.83	0
13	120	F1			F2			F3		
		4.49	4.32	0.17	4.53	4.38	0.15	4.54	4.38	0.16
14	120	F7			F8			F9		
		4.65	4.60	0.05	4.68	4.62	0.06	4.67	4.59	0.08

Table A.3: Masses of samples before and after CCT process (unit:g). Samples 4 to 6.

Grp.	Cyc.	Sample 4			Sample 5			Sample 6		
		m_1	m_2	Δm	m_1	m_2	Δm	m_1	m_2	Δm
1	0	D5			E7			N/A		
		4.86	4.86	0	4.80	4.79	0.01			
2	25	D10			E12					
		4.72	4.69	0.03	4.59	4.59	0			
3	50	D3			E5					
		4.85	4.82	0.03	4.59	4.57	0.02			
4	60	D2			E4					
		4.87	4.87	0	4.62	4.60	0.02			
5	70	D8			E10					
		4.85	4.83	0.02	4.82	4.77	0.05			
6	80	D7			E9					
		4.78	4.77	0.01	4.80	4.76	0.04			
7	90	D12			E2					
		4.71	4.71	0	4.49	4.48	0.01			
8	100	D6			E8					
		4.81	4.79	0.02	4.73	4.73	0			
9	110	D11			E1					
		4.81	4.81	0	4.57	4.55	0.02			
10	120	D1			E3					
		4.91	4.87	0.04	4.51	4.47	0.04			
11	0	D9			E11					
		4.58	4.58	0	4.68	4.68	0			
12	120	D4			E6					
		4.71	4.71	0	4.77	4.77	0			
13	120	F4			F5			F6		
		4.53	4.46	0.07	4.57	4.43	0.14	4.54	4.36	0.18
14	120	F10			F11			F12		
		4.61	4.51	0.10	4.62	4.54	0.08	4.56	4.47	0.09

Appendix B: CFRP mechanical tests

B.1 Longitudinal tensile test

Tensile tests have been performed on CFRP samples in longitudinal direction. The samples are made by 6 layers of 0/90 plain weave 3K CF fabric and 2000/2120 epoxy from Fibreglast. The gauge length is 100 mm and width is 12.7 mm. Tabs are glued to both ends of the sample to avoid fracture in the grips, as shown in Figure B.1 (a). After the testing, all samples failed by a brush-like mode, which is typical in the FRP tensile tests[22]. The stress vs. strain curves are plotted in Figure B.2 and the ultimate tensile stresses are listed in Table B.1. The results are very consistent in in terms of both ultimate tensile stress and strain at fracture. The average peak stress is 1687.8 MPa, which has been applied to the analytical model. However, the strain measurement is not accurate because no strain gauge or DIC system is applied in the tests. Therefore, the measured strain or elastic modulus is not used in the analytical model.

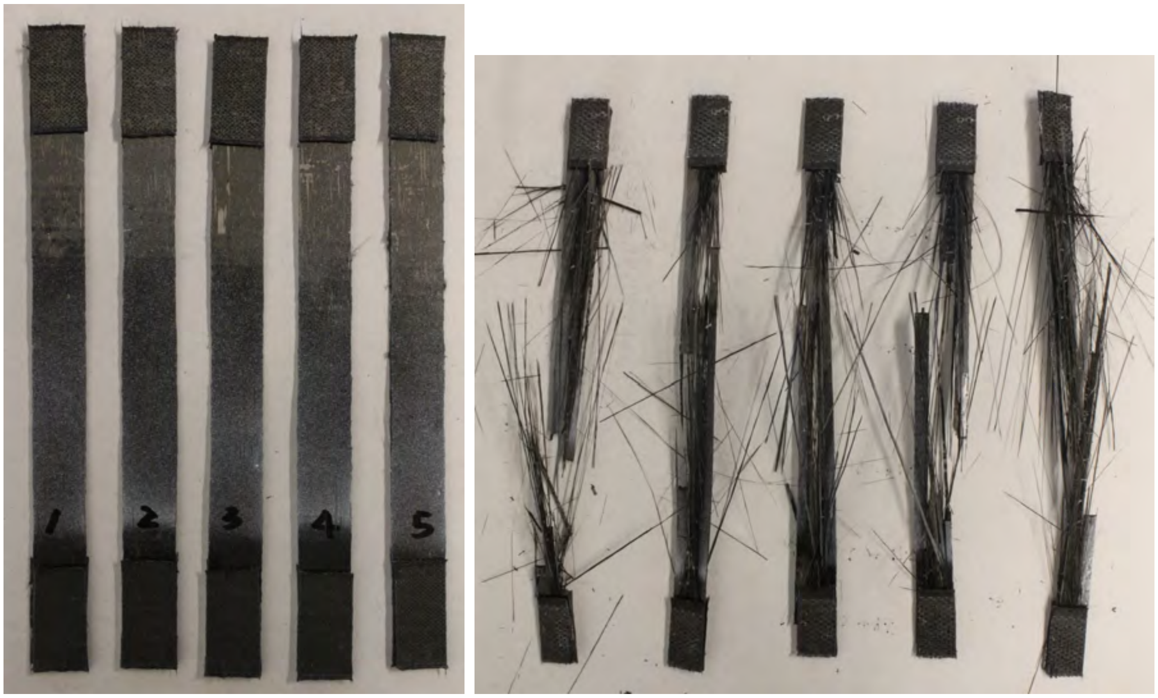

(a) (b)

Figure B.1: CFRP samples before and after tensile testing

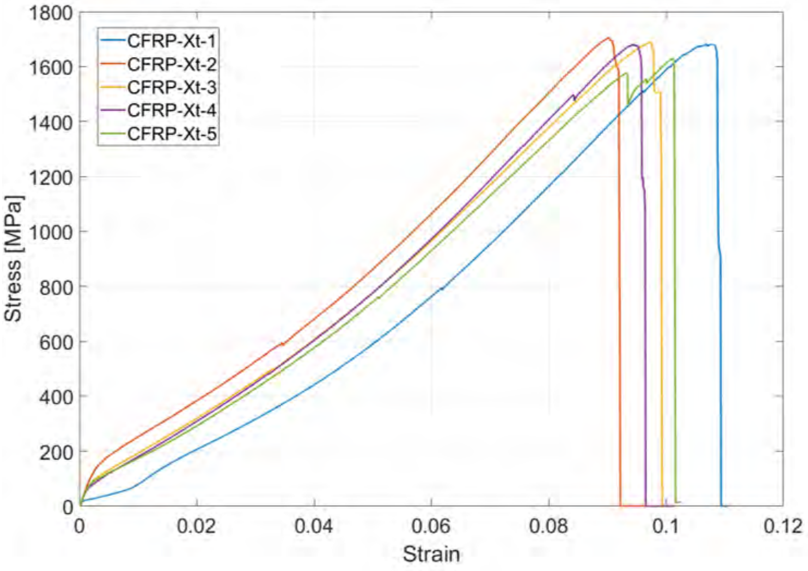

Figure B.2: Stress vs. strain curves of CFRP longitudinal tensile tests

Table B.1: CFRP longitudinal ultimate tensile strength

	Ultimate tensile strength (MPa)
Sample 1	1677
Sample 2	1704
Sample 3	1688
Sample 4	1682
Sample 5	1688
Average	1687.8
SD	82.6

B.2 Longitudinal compressive test

Compressive tests are performed on cylindrical CFRP bars with steel fittings on both ends, as shown in Figure B.3 (a). The gauge length of 12.7 mm and the the diameter of the bar is 4.6 mm. The samples failed along a fracture line through the car, as shown in Figure B.3 (b). From the results listed in Table B.2, the average ultimate compressive strength is 268 MPa

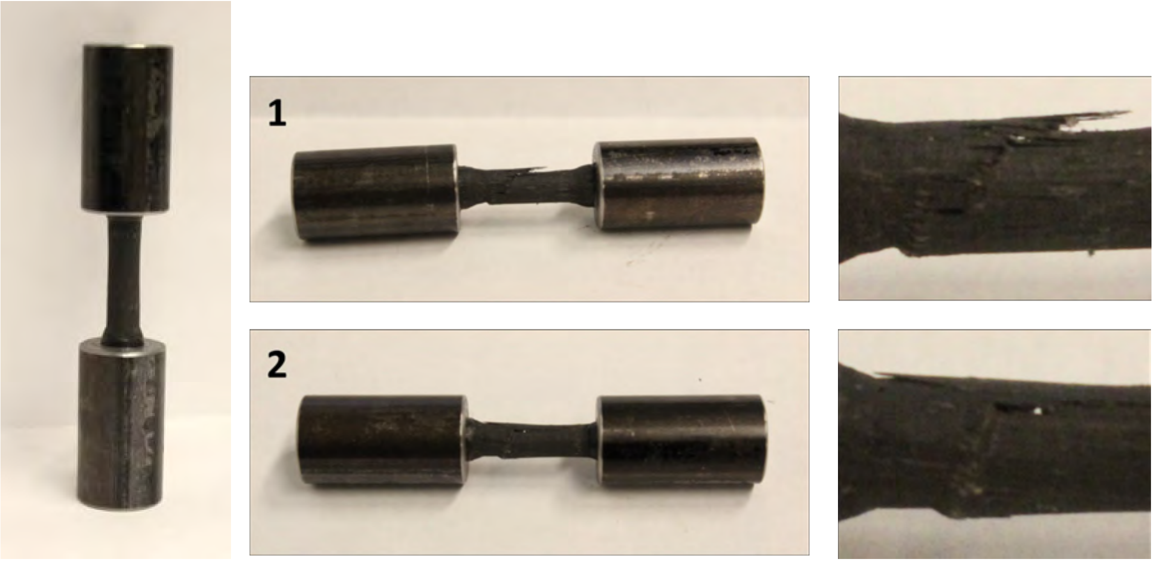

(a) (b)

Figure B.3: CFRP samples before and after compressive testing

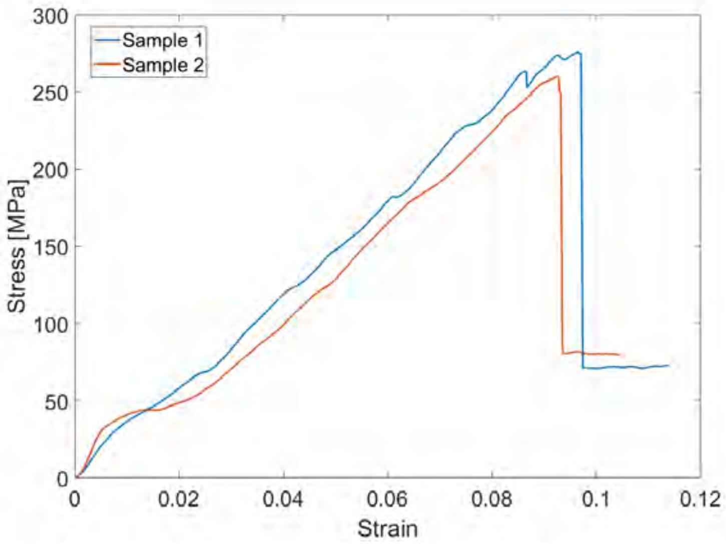

Figure B.4: Stress vs. strain curves of CFRP longitudinal compressive tests

Table B.2: CFRP longitudinal ultimate compressive strength

	Ultimate compressive strength (MPa)
Sample 1	276
Sample 2	260
Average	268

Appendix C: Additional tensile test of CFRP-AA joints

To improve the evenness of the load among the embedded CFRP loops during tensile testing, two techniques are applied to create the CRPP-AA samples. After the UAM process, CF-AA joint is firstly pre-wetted before being cured with epoxy, as illustrated in Figure C.1 (a). The vacuum putty is applied on the surface of the AA. Then an acrylic sheet is covered on top of the vacuum putty. A tube is placed through the acrylic sheet and connected to a vacuum pump on the other end. In this way, the space between the AA and the acrylic sheet is vacuumed. When epoxy is applied at the CF-AA interface underneath the acrylic sheet, the epoxy will flow into the channels and wet the embedded CF tows, then ultimately come through the vent holes.

The second technique is to pre-load the CF-AA joint, as illustrated in Figure C.1 (b). After the additional CF fabrics are being interleaved with the CF-AA joint and the expoy is being applied, the CF-AA joint is being placed up-side-down, and then clamped on the CF side. Using adhesive, a weight is applied on the AA side. After the CF-AA join is positioned with the pre-load, the sample is cured for 24 hours.

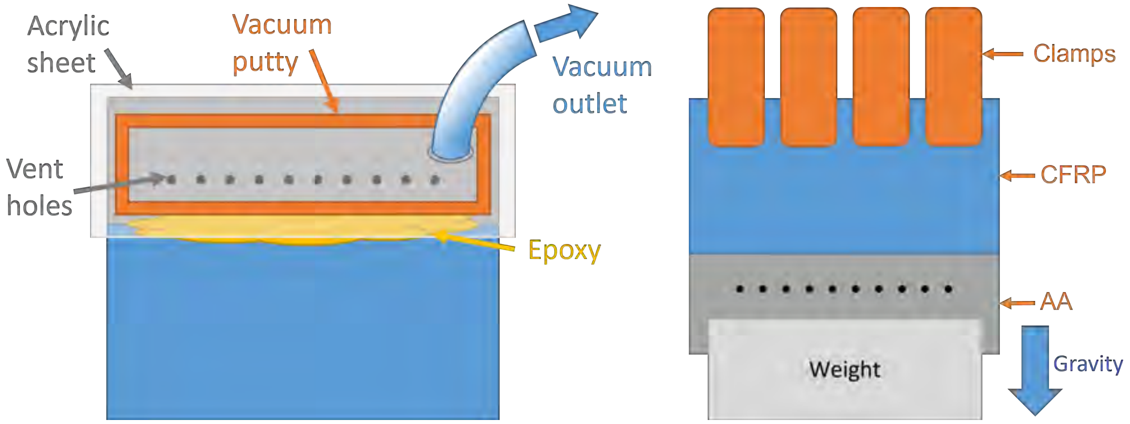
Acrylic sheet
Vacuum putty
Vacuum outlet
Vent holes
Epoxy
Clamps
CFRP
AA
Weight
Gravity

(a) (b)

Figure C.1: Techniques to promote evenly distributed load on the CFRP loops

Tensile tests on 25.4 mm wide samples

With the curing techniques described above, two samples with 3 layers of CF embedded were created. These samples have the same configurations as those in Section 2.3.1. The samples were tested at a strain rate of 1.27 mm/min. Figure C.2 shows the samples after testing. They exhibit failure in CF, which is the same as those in Section 2.3.1. Figure C.3 plots the load vs. displacement curves. Sample 1 and 2 failed at 5124 N and 5516 N, respectively. The average peak load is 5320 N. The displacement data was obtained from the load frame, in stead of the DIC system.

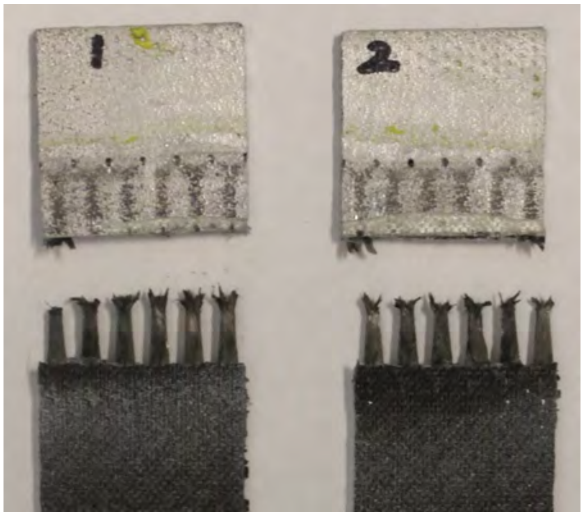

Figure C.2: 25 mm wide tensile sample after testing.

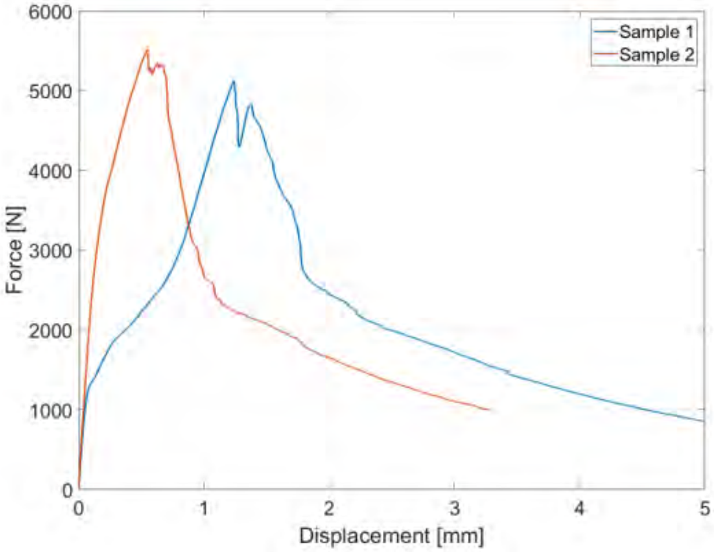

Figure C.3: Load vs. displacement curve of 25 mm wide tensile samples.

Tensile test on a 40 mm wide sample

To evaluate the scalability of the analytical model, a 40 mm wide UAM CF-Al joint with 3 layers of CF embedded was prepared for testing. Each layer has 9 CFRP loops. The 40-mm sample width is determined based on JIS 3136 standard. The sample was tested by an MTS load frame with 40 mm wide hydraulic grips. Images of the sample before and after testing are shown in Figure C.4. All the CF tows failed and no delamination observed. From the load vs. displacement plot shown in Figure C.5, the peak load reached 8707 N. Scaling the peak load by the number of loops per layer, the peak load per inch of this sample is 5804 N.

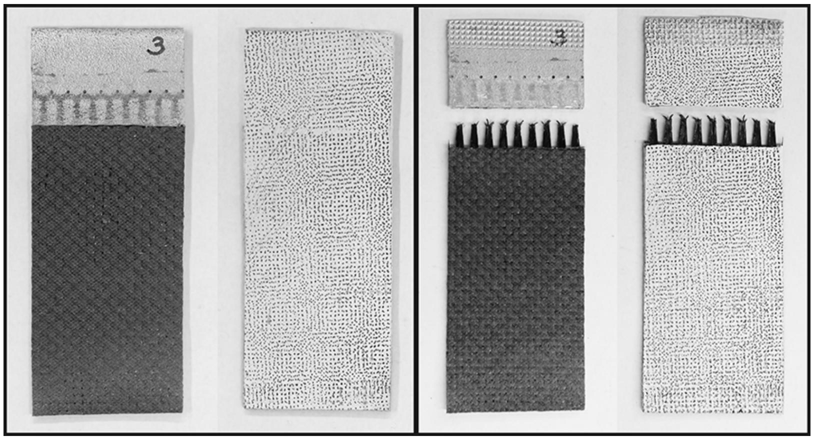

Figure C.4: Front and back of a 40 mm wide tensile sample: (a) before testing; (b) after testing.

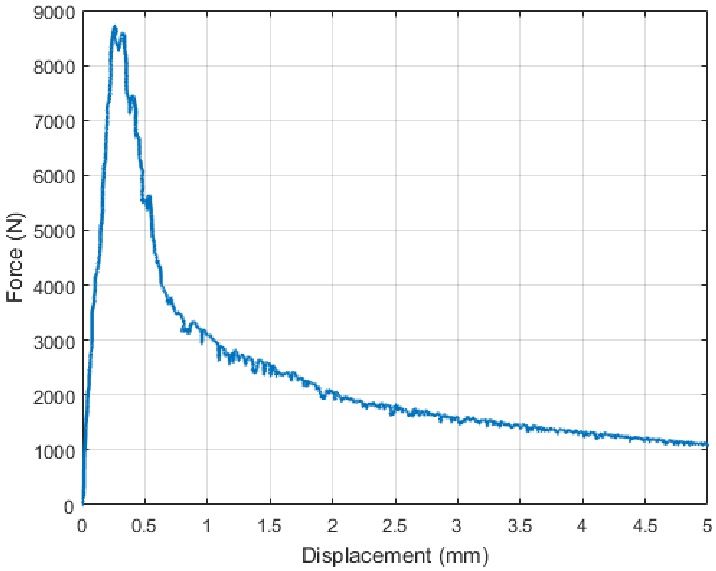

Figure C.5: Load vs. displacement curve of 40 mm wide tensile sample.

Bibliography

[1] JM Arenas, C Alía, JJ Narbón, R Ocaña, and C González. Considerations for the industrial application of structural adhesive joints in the aluminium–composite material bonding. *Composites: Part B*, 44(1):417–423, 2012.

[2] MF Ashby and D Cebon. Materials selection in mechanical design. *Le Journal de Physique IV*, 3(C7):C7–1, 1993.

[3] F Balle, G Wagner, and D Eifler. Ultrasonic spot welding of aluminum sheet/carbon fiber reinforced polymer – joints. *Materialwissenschaft und Werkstofftechnik*, 38(11):934–938, 2007.

[4] TA Barnes and IR Pashby. Joining techniques for aluminium spaceframes used in automobiles Part II — adhesive bonding and mechanical fasteners. *Journal of Materials Processing Technology*, 99:72–79, 2000.

[5] N Charde. Characterization of spot weld growth on dissimilar joints with different thicknesses. *Journal of Mechanical Engineering and Sciences*, 2:172–180, 2012.

[6] A Cherniaev, J Montesano, and C Butcher. Modeling the axial crush response of cfrp tubes using MAT054, MAT058 and MAT262 in LS-DYNA®. In *Proceedings of the 15th International LS-DYNA® Users Conference, Detroit, MI, USA*, pages 10–12, 2018.

[7] N Chowdhury, WK Chiu, J Wang, and P Chang. Static and fatigue testing thin riveted, bonded and hybrid carbon fiber double lap joints used in aircraft structures. *Composite Structures*, 121:315–323, 2015.

[8] H Conen. Deformation und versagen von gfk-strangschlaufen. *Kunststoffe*, 56(9):629–631, 1966.

[9] Z Deng, MB Gingerich, T Han, and MJ Dapino. Yttria-stabilized zirconia-aluminum matrix composites via ultrasonic additive manufacturing. *Composites Part B: Engineering*, 151:215–221, 2018.

[10] SM Goushegir, JF dos Santos, and ST Amancio-Filho. Influence of aluminum surface pre-treatments on the bonding mechanisms and mechanical performance of metal-composite single-lap joints. *Welding in the World*, 61(6):1099–1115, 2017.

[11] H Guo, MB Gingerich, LM Headings, R Hahnlen, and MJ Dapino. Joining of carbon fiber and aluminum using ultrasonic additive manufacturing (UAM). *Composite Structures*, 208:180–188, 2019.

[12] R Hahnlen and MJ Dapino. Stress-induced tuning of ultrasonic additive manufacturing Al-NiTi composites. In *Behavior and Mechanics of Multifunctional Materials and Composites 2012*, volume 8342, San Diego, apr 2012. SPIE.

[13] R Hahnlen and MJ Dapino. NiTi–Al interface strength in ultrasonic additive manufacturing composites. *Composites: Part B*, 2013.

[14] R Hahnlen, G Fox, and MJ Dapino. Ultrasonic soldering of shape memory NiTi to aluminum 2024. *Welding Journal*, 91(1):1s–7s, 2012.

[15] H Hamada, N Oya, K Yamashita, and Z-I Maekawa. Tensile strength and its scatter of unidirectional carbon fibre reinforced composites. *Journal of reinforced plastics and composites*, 16(2):119–130, 1997.

[16] T Han, CH Kuo, N Sridharan, LM Headings, SS Babu, and MJ Dapino. Effect of preheat temperature and post-process treatment on the microstructure and mechanical properties of stainless steel 410 made via ultrasonic additive manufacturing. *Materials Science and Engineering: A*, 769:138457, 2020.

[17] T Havar. Beitrag zur gestaltung und auslegung von 3d-verstärkten faserverbundschlaufen. 2007.

[18] A Hehr and MJ Dapino. Interfacial shear strength estimates of NiTi–al matrix composites fabricated via ultrasonic additive manufacturing. *Composites Part B: Engineering*, 77:199–208, aug 2015.

[19] A Hehr, PJ Wolcott, and MJ Dapino. Effect of weld power and build compliance on ultrasonic consolidation. *Rapid Prototyping Journal*, 2016.

[20] VHB Hernandez, SK Panda, Y Okita, and NY Zhou. A study on heat affected zone softening in resistance spot welded dual phase steel by nanoindentation. *Journal of Materials Science*, 45(6):1638–1647, dec 2009.

[21] WJ Joost. Reducing vehicle weight and improving u.s. energy efficiency using integrated computational materials engineering. *JOM*, 64(9):1032–1038, aug 2012.

[22] QS Khan, MN Sheikh, and MNS Hadi. Tension and compression testing of fibre reinforced polymer (frp) bars. 2015.

[23] CY Kong, RC Soar, and PM Dickens. Optimum process parameters for ultrasonic consolidation of 3003 aluminium. *Journal of Materials Processing Technology*, 146:181–187, 2003.

[24] F Lambiase and DC Ko. Two-steps clinching of aluminum and carbon fiber reinforced polymer sheets. *Composite Structures*, 164:180–188, 2017.

[25] SM Lee. *Handbook of composite reinforcements*. John Wiley & Sons, 1992.

[26] S Li, E Sitnikova, Y Liang, and AS Kaddour. The tsai-wu failure criterion rationalised in the context of UD composites. *Composites Part A: Applied Science and Manufacturing*, 102:207–217, 2017.

[27] F Lionetto, F Balle, and A Maffezzolia. Hybrid ultrasonic spot welding of aluminum to carbon fiber reinforced epoxy composites. *Journal of Materials Processing Tech.*, 247:289–295, 2017.

[28] Q Liu, Z Ou, Z Mo, Q Li, and D Qu. Experimental investigation into dynamic axial impact responses of double hat shaped CFRP tubes. *Composites Part B: Engineering*, 79:494–504, sep 2015.

[29] Q Liu, H Xing, Y Ju, Z Ou, and Q Li. Quasi-static axial crushing and transverse bending of double hat shaped CFRP tubes. *Composite Structures*, 117:1–11, nov 2014.

[30] M Mandel and L Krüger. Long-term corrosion behaviour of EN AW-6060-T6 in an aluminium/carbon-fibre reinforced polymer self-piercing rivet joint: Langzeitkorrosionsverhalten von en aw-6060-t6 in einer aluminium/kohlenstofffaserverstärkten kunststoff halbhohlstanzniet-verbindung. *Materialwissenschaft und Werkstofftechnik*, 45(12):1123–1129, 2014.

[31] N Manente André, JF dos Santos, and ST Amancio-Filho. Evaluation of joint formation and mechanical performance of the AA7075-T6/CFRP spot joints produced by frictional heat. *Materials*, 12(6):891, 2019.

[32] G Marannano and B Zuccarello. Numerical experimental analysis of hybrid double lap aluminum-CFRP joints. *Composites: Part B*, 71:28–39, 2014.

[33] P Mitschang, R Velthuis, and M Didi. Induction spot welding of metal/CFRPC hybrid joints. *Advanced Engineering Materials*, 15(9):804–813, 2012.

[34] K Nagatsuka, S Yoshida, A Tsuchiya, and K Nakata. Direct joining of carbon-fiber–reinforced plastic to an aluminum alloy using friction lap joining. *Composites: Part B*, 73:82–88, 2014.

[35] HA Nied. The finite and element modeling and of the and cl and o and resistance spot and welding process. 1983.

[36] TEA Ribeiro, RDSG Campilho, LFM Da Silva, and L Goglio. Damage analysis of composite-aluminium adhesively-bonded single-lap joints. *Composite Structures*, 136:25–33, 2016.

[37] M Salamati, M Soltanpour, A Zajkani, and A Fazli. Improvement in joint strength and material joinability in clinched joints by electromagnetically assisted clinching. *Journal of Manufacturing Processes*, 41:252–266, 2019.

[38] K Sato, T Inazumi, A Yoshitake, and SD Liu. Effect of material properties of advanced high strength steels on bending crash performance of hat-shaped structure. *International Journal of Impact Engineering*, 54:1–10, apr 2013.

[39] M Scheidt. *Lightweight aluminum structures with embedded reinforcement fibers via ultrasonic additive manufacturing*. PhD thesis, The Ohio State University, 2016.

[40] JJ Schomer, AJ Hehr, and MJ Dapino. Characterization of embedded fiber optic strain sensors into metallic structures via ultrasonic additive manufacturing. In *Sensors and Smart Structures Technologies for Civil, Mechanical, and Aerospace Systems 2016*, volume 9803, page 980320. International Society for Optics and Photonics, 2016.

[41] JJ Schomer, AJ Hehr, and MJ Dapino. Characterization of embedded fiber optic strain sensors into metallic structures via ultrasonic additive manufacturing. In *Sensors and Smart Structures Technologies for Civil, Mechanical, and Aerospace Systems*, volume 9803, Las Vegas, apr 2017. SPIE.

[42] SB Shea. 54.5 MPG and Beyond: Materials Lighten the Load for Fuel Economy. https://www.energy.gov/articles/545-mpg-and-beyond-materials-lighten-load-fuel-economy, 2012.

[43] ESM Sherif, AA Almajid, FH Latif, and H Junaedi. Effects of graphite on the corrosion behavior of aluminum-graphite composite in sodium chloride solutions. *Int. J. Electrochem. Sci*, 6:1085–1099, 2011.

[44] Niyanth Sridharan, Paul Wolcott, Marcelo Dapino, and Sudarsanam Suresh Babu. Microstructure and mechanical property characterisation of aluminium–steel joints fabricated using ultrasonic additive manufacturing. *Science and Technology of Welding and Joining*, 22(5):373–380, 2017.

[45] F Staab and F Balle. Ultrasonic torsion welding of ageing-resistant Al/CFRP joints: Properties, microstructure and joint formation. *Ultrasonics*, 93:139–144, 2019.

[46] W Tong, H Tao, N Zhang, X Jiang, MP Marya, LG Hector, and XQ Gayden. Deformation and fracture of miniature tensile bars with resistance-spot-weld microstructures. *Metallurgical and Materials Transactions A*, 36(10):2651–2669, 2005.

[47] SW Tsai and EM Wu. A general theory of strength for anisotropic materials. *Journal of composite materials*, 5(1):58–80, 1971.

[48] J Wenning. Fabrisonic LLC, personal communication. May May 18 2017.

[49] MD White and N Jones. Experimental quasi-static axial crushing of top-hat and double-hat thin-walled sections. *International Journal of Mechanical Sciences*, 41(2):179–208, 1999.

[50] MD White and N Jones. Experimental study into the energy absorbing characteristics of top-hat and double-hat sections subjected to dynamic axial crushing. *Proceedings of the Institution of Mechanical Engineers, Part D: Journal of Automobile Engineering*, 213(3):259–278, 1999.

[51] PJ Wolcott and MJ Dapino. Ultrasonic additive manufacturing. In *Additive Manufacturing Handbook*, pages 275–298. CRC Press, 2017.

[52] PJ Wolcott, A Hehr, and MJ Dapino. Optimized welding parameters for Al 6061 ultrasonic additive manufactured structures. *Journal of Materials Research*, 29(17):2055–2065, 2014.

[53] PJ Wolcott, C Pawlowski, LM Headings, and MJ Dapino. Seam welding of aluminum sheet using ultrasonic additive manufacturing system. *Journal of Manufacturing Science and Engineering*, 139(1):011010, 2016.

[54] S Yan, GL Song, Z Li, H Wang, D Zheng, F Cao, M Horynova, MS Dargusch, and L Zhou. A state-of-the-art review on passivation and biofouling of ti and its alloys in marine environments. *Journal of materials science & technology*, 34(3):421–435, 2018.

[55] A Zajkani and M Salamati. Numerical and experimental investigation of joining aluminium and carbon fiber reinforced composites by electromagnetic forming process. In *7th International Conference on High Speed Forming*, pages 59–68, Dortmund, 2016.

[56] Y Zhai, D Li, X Li, and L Wang. An experimental study on the effect of joining interface condition on bearing response of single-lap, countersunk composite-aluminum bolted joints. *Composite Structures*, 134:190–198, 2015.

[57] L Zhao, Y Li, J Zhang, L Zhou, and N Hu. A novel material degradation model for unidirectional CFRP composites. *Composites Part B: Engineering*, 135:84–94, 2018.